Birk Emil Karlsen-Bæck

Modelling Control Loops for SPS-LHC Beam Transfer Studies

Master's thesis in Applied Physics and Mathematics
Supervisor: Assoc. Prof. Jon Andreas Støvneng
Co-supervisor: Dr. Helga Timko and Dr. Theodoros Argyropoulos
June 2022

Master's thesis

NTNU
Norwegian University of Science and Technology
Faculty of Natural Sciences
Department of Physics

NTNU
Norwegian University of
Science and Technology

Birk Emil Karlsen-Bæck

Modelling Control Loops for SPS-LHC Beam Transfer Studies

Master's thesis in Applied Physics and Mathematics
Supervisor: Assoc. Prof. Jon Andreas Støvneng
Co-supervisor: Dr. Helga Timko and Dr. Theodoros Argyropoulos
June 2022

Norwegian University of Science and Technology
Faculty of Natural Sciences
Department of Physics

Abstract

In the HL-LHC era, the injection of SPS beams might lead to beam losses and RF power limitations in the LHC. An accurate simulation model of both the SPS and LHC control loops in the longitudinal beam dynamics simulator BLonD is indispensable for estimating these beam losses and power limitations. This thesis presents simulation models and benchmarks for the SPS and LHC cavity controllers that control the RF voltage in amplitude and phase in the SPS and LHC accelerating cavities, in high beam-loading conditions. High-intensity, multi-bunch beam distributions can be accurately modelled in the SPS using the SPS cavity controller model, which will be necessary for future beam transfer studies. The SPS model was found to show good agreement with beam measurement data and measurements of the LHC cavity loop transfer functions were accurately reproduced by the LHC cavity loop model.

Sammendrag

For HL-LHC æraen kan overføring av partikkelstråler fra SPS føre til tap av partikler og begrensninger i elektrisk effekt i radiofrekvens systemene til LHC. Presise numeriske modeller av kontrollsystemene i både SPS og LHC i simulatoren BLonD er essensielle for å gi estimater for både tap av partikler og begrensinger i elektrisk effekt. Denne masteroppgaven presenterer modeller av både SPS og LHC "cavity controllers", viser hvordan disse ble validert og sammenliknet med målinger. Disse kontrollsystemene regulerer spenningen i de akselererende strukturene i akseleratorene, både i amplitude og i fase under forhold med høy effekt grunnet partikkelstrålen. Ved bruk av SPS "cavity controller" modellen kan man skape realistiske høyintensitets stråler, som vil bli viktig for fremtidige studier av stråleoverføring mellom SPS og LHC. Det ble funnet at SPS modellen er i god enighet med eksperimentell data av partikkelstråler. Videre ble det vist at LHC "cavity loop" modellen kunne gjenskape målte overføringsfunksjoner til tilfredsstillende nøyaktighet.

Preface

This master thesis was written at the European Organization for Nuclear Research (CERN) and is the final part of a Master of Science program in Applied Mathematics and Physics at the Norwegian University of Science and Technology (NTNU). The work was carried out during the spring of 2022 in the Beams & RF Studies (BR) section under the supervision of Dr. Helga Timko and Dr. Theodoros Argyropoulos at CERN and Assoc. Prof. Jon Andreas Støvneng at the Physics Department at NTNU. Sections 2.1-2.2, 2.4, 3.1-3.2.1 have commonalities with the specialization project [1] that was carried out during the fall of 2021. Sections 3.4-3.6 are continuations and improvement of the analysis done in [1], but with a refined version of the SPS cavity controller.

I would like to express my sincerest gratitude to Dr. Helga Timko for her wise guidance, inspiring insight and for always providing valuable input. It has truly been an joy to work closely with such a brilliant physicist and I have gone out of all our meetings feeling smarter and more knowledgeable than when I went in. I am truly grateful for all her feedback, effort and facilitation. I want to extend a big thank you to Assoc. Prof. Jon Andreas Støvneng for the facilitation that allowed me to write my master thesis at CERN.

I would also like to thank Dr. Theodoros Argyropoulos for his great guidance and wise words. In addition to Dr. Timko, he has been an excellent guide into the field of accelerator physics. I want to thank both him and Dominika Agnieszka Dlugosz for facilitating the acquisitions for some of the data that was used in this thesis. I am also very grateful for all the valuable feedback and input I have gotten from all the experts in both the Beams & RF Studies section and the Feedbacks and Beam Control section. A big thank you to Ludovico Bessi, Paraskevi Papadopoulou, Evin Thomas Vinten, Dominika Agnieszka Dlugosz and Cecilia Martínez Martin for morning coffees and for raising my spirit during rough days.

I want to thank my mom Prof. Unn-Doris Karlsen Bæck for giving me excellent career and life advice and for being the best mom I could ever ask for. I want to thank my sister Lykke Linnea Karlsen-Bæck for lovely conversations and support. Thank you to Jørgen and Linus Hjerde Bæck for being my brothers and listening to my speeches about physics. I Dr. Torgeir Hjerde for his advice and food. Lastly, I want to thank my dad Dr. Geir Runar Karlsen for always believing in me, for sparking an interest in physics and mathematics that turned into a deep passion and for being the best dad a son could ever ask for.

Prévessin, 20 June 2022   Birk Emil Karlsen-Bæck

Contents

List of Figures

List of Tables

1 Introduction

During the 1960's, Peter Higgs [2] and two other groups of scientists: Robert Brout and François Englert [3], as well as Gerald Guralnik, Carl Hagen and Tom Kibble [4], independently postulated the existence of a new particle. The other elementary particles in the Standard Model would obtain their mass through their interaction with this boson, now known as the Higgs boson. In addition, the existence of this particle would introduce electroweak symmetry breaking and gravitational charge into the Standard Model. Taking into account interactions both within and beyond the Standard Model, the theory predicted a relatively high mass for the boson, with the exact mass determined by physics beyond the Standard Model. Thus in most models, the Higgs boson would require the energy of several hundreds of GeVs to produce. The accelerators at the time could not produce center of mass energies high enough to probe this energy range, and so studies for two higher-energy colliders started during the 1980's. These were the Superconducting Super Collider (SSC) in the US and the Large Hadron Collider (LHC) at the European Organization for Nuclear Research (CERN) in Switzerland. The SSC project was eventually canceled during the 1990's, while the construction of the LHC at CERN finished in 2008. Thus the LHC became, and still is, the largest accelerator in the world. In 2012, two of the LHC detectors [5, 6] independently claimed the discovery of the Higgs boson.

The LHC is located around the French-Swiss boarder near Geneva and is a part of the CERN accelerator complex, see Fig. 1.1 [7]. CERN hosts a number of different accelerators which operate at different energy ranges and deliver charged particle beams of different species, to their own physics experiments or to another machine. The accelerator complex consists of two kinds of accelerators: linear and circular machines. As indicated by their name, linear accelerators (LINACs) have a straight beam pipe and hence, a beam that moves in a straight line. Since the beam only passes through the accelerator once, the machine has a large number of accelerating structures to maximize the energy of the beam. In circular machines on the other hand, the beam is bent around the machine. This enables the machine to use the same accelerating structures many times. As described by the Lorentz equation in classical electrodynamics, only electric fields can do work on charged particles while the magnetic fields can bend their trajectory. This is why circular machines use magnetic fields to bend the
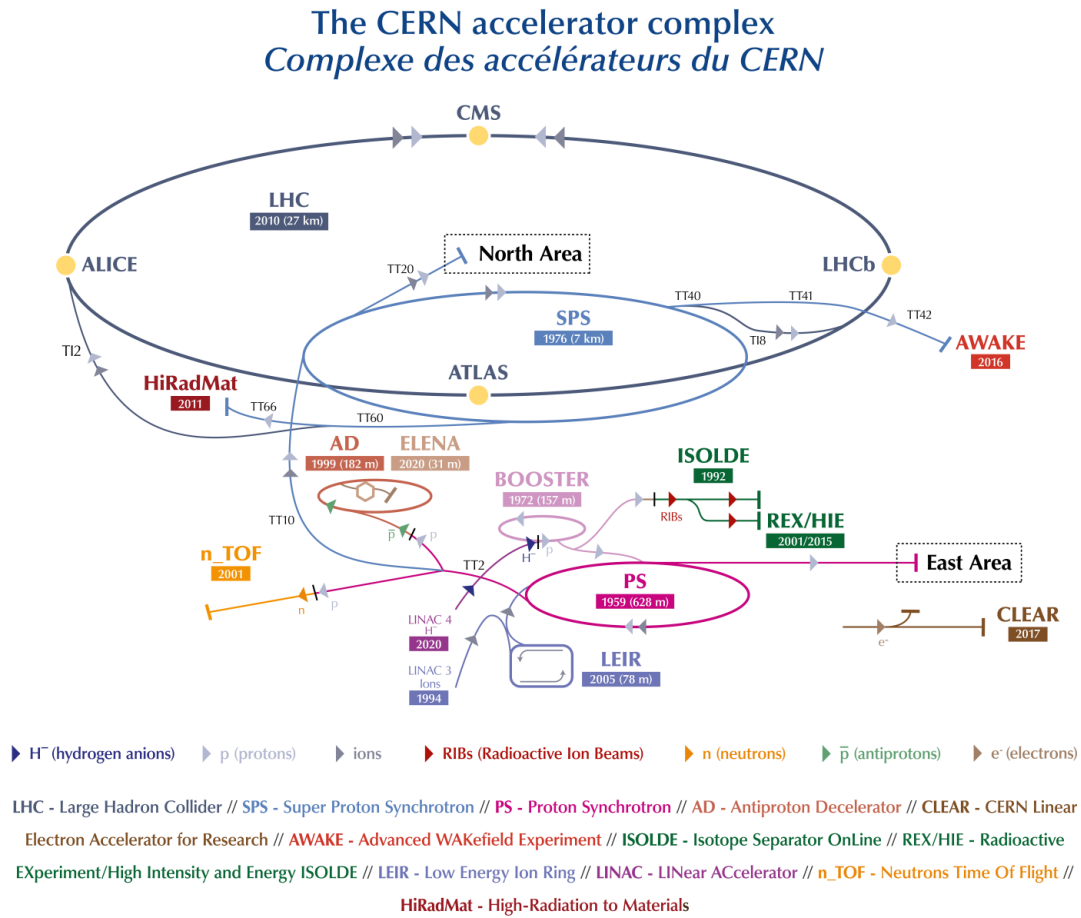
Figure 1.1: Schematic overview of the particle accelerators in the CERN accelerator complex.

path of the beam while both linear and circular machines use electric fields for acceleration.

At CERN, all operational circular machines are so-called synchrotrons and this thesis focuses on longitudinal beam dynamics in synchrotrons. Synchrotrons use Radio-Frequency (RF) cavities to accelerate the beam. These are cavities that resonate with electromagnetic waves at frequencies that are determined by their designed geometry and are usually in the radio spectrum. In circular machines the frequency of the RF cavities (the RF frequency) is kept at a multiple of the revolution frequency of the beam. Additionally, the orbit radius of a charged particle is adjusted by the magnetic field strength to always keep the particles close to the design orbit, independent of their energy. The defining feature of a synchrotron is that they keep the orbit radius of the beam fixed by synchronizing the RF frequency to the magnetic field strength supplied by the magnetic lattice. In the CERN accelerator complex, most beams, like the proton beams for the LHC experiments, are transferred from lower-energy machines to incrementally higher-energy machines, as indicated by the arrows in Fig. 1.1 [7]. This is because the beam needs a certain amount of initial energy to start circulating in a synchrotron,

which is due to the fixed radius of the beam pipe. It also means that the beam that the Super Proton Synchrotron (SPS) eventually injects into the LHC starts in LINAC4 and is passed from one machine to the next. Antiproton beams, on the other hand, are sent through a small chain of decelerators to cool down the beam.

As the charged particles of the beam circulate around a synchrotron, they interact electromagnetically with the machine components along the beam line and with each other; we call this collective effects. Each machine component has a characteristic electrical impedance that the beam is exposed to when traveling through the machine. The beam-impedance interaction results in beam-induced voltages, which perturb the already existing voltage generated in the RF cavities. Collective effects, if not controlled, can lead to undesired beam instabilities and, as a consequence, loss of particles. In the field of beam dynamics, in general, the aim is therefore to keep the beam stable and bunched.

The biggest contributor to the total impedance of an accelerator is often the RF cavity impedance at its fundamental frequency. The beam-induced voltage present in the cavity changes the RF power needed to maintain a given RF voltage, and we therefore say that the cavity is beam loaded. To reduce this beam-loading effect, the LHC and SPS machines employ so-called cavity controllers or local feedbacks around the cavity that make use of control loops. The purpose of these circuits are two-fold. Firstly, they regulate the amplitude and phase of the voltage in the RF cavity and secondly, they reduce the impedance of the fundamental cavity frequency seen by the beam.

For the proton beams in the LHC and its injectors, the "nominal" beam intensity till 2018 was 1.15×10^{11} protons per bunch (p/b). The High-Luminosity LHC (HL-LHC) project [8] is planning to double this to 2.3×10^{11} p/b at LHC injection after 2028. The HL-LHC upgrade aims at exploiting the full potential of the LHC to achieve increased luminosity for the experiments and therefore more collisions and more data. To deliver such beams to the LHC, the LHC Injector Upgrade (LIU) project [9], has successfully upgraded the LHC injector chain during Long Shutdown 2 (LS2). However, the LHC will not actually be able to accept HL-LHC beam intensities before Long Shutdown 3 (LS3), so during Run 3 (2022-2025), the beam intensity is planned to be increased gradually from 1.15×10^{11} p/b to 1.8×10^{11} p/b. For the main RF system in the LHC, power limitations and possibly beam losses are expected to occur at injection for HL-LHC injection [10].

The increase of intensity during Run 3 will be used to benchmark and refine the models of the LHC RF system. The final aim is to give accurate predictions for the HL-LHC era and find alternative solutions to overcome the power limitations. The main investigation tool for these studies are simulations, which is the only way to account for all the complexities of the physics of the beam. This thesis will make use of the Beam Longitudinal Dynamics (BLonD) simulator [11]. As the name suggests, this simulator models the dynamics of the beam in the two dimensional longitudinal phase-space in synchrotrons.

To accurately simulate the power transients and particle loss at transfer to the LHC, realistic models of the control loops are needed. These control loops are needed both to generate realistic beams in the SPS and accurately reproduce the dynamics in the LHC during and after the beam injection. This thesis will present the implementation and the benchmarking of the

cavity controllers for both the SPS and the LHC in BLonD.

Chapter 2 will introduce the basic terminology relevant to the two accelerators that the rest of the thesis will focus on, namely the LHC and SPS. In addition, it will briefly walk through the basics of longitudinal beam dynamics in a synchrotron and how this is implemented in BLonD. The chapter will then go on to explain the ultimate goal of the LHC injection studies, how this thesis contributes to these studies, and will end on a brief introduction into control loops. Chapter 3 will introduce the SPS RF cavities and their cavity controller. It will then describe how this was integrated in BLonD and some basic tests of the implementation. The chapter will finish by showing results from benchmarks of the BLonD SPS cavity controller model, both against theory and measurements. Chapter 4 will discuss the LHC cavity controller and show results from a comparison of transfer functions between the BLonD model and the real system. Finally, Chapter 5 will discuss the future work left and a conclusion will be given in Chapter 6 based on the results that were found throughout the thesis.

2 Background

This chapter will give a brief background to the work that was done. It will introduce the accelerators to which the work was related to and go through the basic equations governing the beam dynamics in the longitudinal plane and how these are implemented in the BLonD simulator. Lastly, the chapter introduces the cavity control systems in the accelerators at hand, why they are important to model correctly, and describes the control theory concepts relevant to the thesis.

2.1 The CERN Accelerator Complex

Figure 1.1 gives an overview of the entire accelerator complex at CERN. As mentioned in the introduction chapter, proton beams for the LHC are first accelerated in LINAC4, followed by a series of synchrotrons. This thesis will focus on the longitudinal dynamics at proton beam transfer between the SPS and LHC.

A synchrotron accelerator is characterized by having a fixed circumference, meaning that the magnetic field keeping the particles in orbit around the ring has to increase in magnitude as the energy of the particles increases. The energy is given to the particle beam through electric fields resonating in Radio-Frequency (RF) cavities. The frequency of the oscillating electric field ω_{rf} is usually an integer multiple of revolution frequency ω_{rev} of the particles:

$$\omega_{\text{rf}} = h\omega_{\text{rev}}, \tag{2.1}$$

where h is know as the harmonic number. This equation describes the synchronization of the accelerating RF field and the magnetic lattice and hence the name "synchrotron".

The magnetic cycle of an accelerator is normally split into 3 parts. The first part of the cycle is know as flat bottom and the particles are injected during this initial stage with the lowest energy of the cycle. Once the synchrotron is sufficiently filled with beam, the magnetic field and RF frequency ramp starts and the particles are accelerated. Flattop is reached when the particles have obtained their maximum energy. Some time after flattop is reached the beam can be either extracted to (or, in the case of the LHC, collided in) an experiment, extracted to a beam dump, or to another accelerator. In the LHC, two beams circulate in two beam lines in opposite direction and can be collided at four interaction points along the ring. The

aforementioned three parts of the cycle can be seen in the momentum program of an SPS cycle depicted in Fig. 2.1.
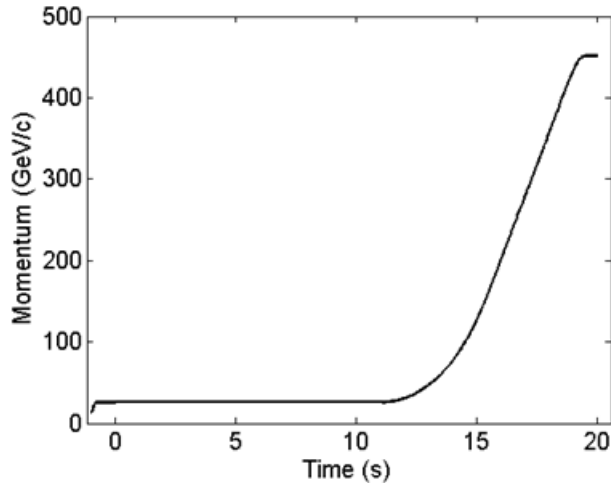
Figure 2.1: An example of a magnetic cycle in the SPS.

2.1.1 The Super Proton Synchrotron

The SPS is the second largest synchrotron at CERN. It was first operated in 1976 and provided beam to the UA1 [12] and UA2 [13] experiments which led to the discovery of the W and Z bosons. Today it serves as the injector for the LHC as well as delivering beam to fixed-target experiments and to the AWAKE wakefield acceleration experiment. The most important machine parameters of the SPS can be found in Table 2.1 [9]. In this machine, the beam is accelerated through the use of normal-conducting, travelling wave cavities (TWCs) [14]. In these RF cavities, an electromagnetic (EM) wave is injected and travels along (in the opposite direction to) the beam and is extracted at the other end of the cavity. The EM wave is generated by upgraded tetrode and new solid-state amplifiers on the surface [15] and coupled into the cavities in the tunnel through fundamental power couplers.

As was mentioned in Chapter 1, the LIU upgrade [9] was completed during LS2 on all the LHC injectors. A major part of this upgrade was to completely renovate the RF system in the SPS, preparing it for higher intensity beams. For instance, the TWCs were shortened and re-grouped. Before the ugrade, the 200 MHz system consisted of two 5-section and two 4-sections cavities, and were supplied by two tetrode amplifier chains. To reduce beam-loading, the cavities were restructured into four 3-section and two 4-section cavities, using also two spare sections for this regrouping. Additionally, the new solid-state power system was built and commissioned to power the 3-section cavities. Before the LIU upgrade, the SPS 200 MHz RF system could supply a maximum total voltage of 7 MV with nominal beam intensities. After the upgrade, the maximum was increased to 10 MV for HL-LHC beam intensities. This increase in total voltage was needed for beam stability in the longitudinal plane, as the beam circulating in the SPS is subject to many different types of instabilities at different stages during

the cycle [16, 17, 18, 19]. For the HL-LHC era, the SPS bunch intensity target is 2.6×10^{11} p/b at injection and 2.3×10^{11} p/b at extraction, with a target bunch length of 1.65 ns $\pm$ 10 % across the batch at extraction.

Table 2.1: SPS and LHC parameters during Run 3.

Parameter	Symbol	SPS	LHC
Circumference	C	6.9 km	26.7 km
Transition gamma	γ_t	18.0	53.8
Max. RF voltage	V	10 MV	16 MV
Harmonic number	h	4620	35640
Momentum (flat bottom)	p	26 GeV/c	450 GeV/c
Revolution frequency (flat bottom)	f_{rev}	43347 Hz	11245 Hz
Synchronous momentum (flattop)	p_s	450 GeV/c	6.8 TeV/c
Revolution frequency (flattop)	f_{rev}	43347 Hz	11245 Hz

2.1.2   The Large Hadron Collider

The LHC was first put into operation in 2008. As mentioned previously, it has two separate beam lines with particles running in opposite direction. These particles can be collided in four interaction regions, were the four principal LHC experiments ATLAS, CMS, ALICE and LHCb are hosted. The LHC can accelerate both protons and heavier ions depending on the cycle. The particles are kept in orbit through the use of thousands of superconducting magnets placed in a lattice along the ring.

The LHC uses superconducting, standing-wave cavities [20] to accelerate the beam. The electromagnetic waves are generated by klystrons and coupled into the RF cavities through wave guides. Each of the klystrons power one cavity and can supply a maximum of 300 kW [21]. The LHC RF cavities themselves can provide operationally an accelerating field 2 MV/cavity maximum, and there are eight cavities per beam installed. When operating with high-intensity batched beam in the so-called half-detuning scheme [22], most of the RF power supplied to the cavities is used for beam-loading compensation.

The most important machine parameters, mainly based on the LHC design [23], can be found in Table 2.1. During Run 2 (2015-2018), the flat top energy was 6.5 TeV for protons. During Run 3, the LHC flat top energy is 6.8 TeV.

2.2   Introduction to Longitudinal Beam Dynamics

To introduce longitudinal beam dynamics we will start by modelling a single RF cavity interacting with the charged particles in the beam. The electric field in an RF cavity experienced by a charged particle passing through it can be written in the form [24]

$$\varepsilon(t) = \varepsilon_0 \sin\left(\omega_{\text{rf}} t + \phi_s\right) \tag{2.2}$$

where ε_0 is the amplitude of the electric field, ω_{rf} is the RF angular frequency, t is the arrival time of the particle and ϕ_s is the RF phase experienced by the synchronous particle when travelling through the cavity. The synchronous particle is the particle that arrives at $t = 0$ at a given turn. Note that the synchronous particle can change from turn to turn. The angular revolution frequency, ω_{rev}, is related to the RF angular frequency through Eq. (2.1). In turn, the angular revolution frequency is given as

$$\omega_{\mathrm{rev}} = \frac{\beta_s c}{R_s} \tag{2.3}$$

where β_s is the relativistic beta of the synchronous particle, c is the speed of light and R_s is the mean radius of the synchronous particle orbit around the synchrotron. If the accelerating gap length of the cavity is assumed to be g, then the particle is accelerated by the electric field during the time span $t \in nT_{\mathrm{rev}} + \left(-g/2\beta_s c, g/2\beta_s c\right)$, where n is an integer. With this in mind, it is possible to derive the energy kick for a single passing of the RF cavity to be

$$\Delta E = q\varepsilon_0 g T \sin\phi_s \;, \;\; T = \frac{\sin\left(hg/2R_s\right)}{hg/2R_s} \tag{2.4}$$

where q is the particle charge and T is known as the transit time factor arising from the fact the particles have a finite time-of-flight through the cavity. It is also convenient to define the effective voltage over the cavity to be $V = \varepsilon_0 g T$. From Eq. (2.4), one sees that the rate of acceleration is given as

$$\dot{E}_s = \frac{\omega_{\mathrm{rev}}}{2\pi} q V \sin\phi_s \;, \tag{2.5}$$

where E_s is the total energy of the synchronous particle. $\dot{E}_s$ is the change in energy ΔE over the course of a turn of length $T_{\mathrm{rev}} = 2\pi/\omega_{\mathrm{rev}}$ in time, assuming there is no other sources of loss or gain of energy.

Until now we have only handled the synchronous particle, which have the design orbit and energy of the machine. Let us now consider a particle with some small deviation in energy from the synchronous particle. This particle is characterized by

$$\begin{cases} \omega = & \omega_{\mathrm{rev}} + \Delta\omega \\ \phi = & \phi_s + \Delta\phi \\ p = & p_s + \Delta p \\ E = & E_s + \Delta E \\ t = & t_s + \Delta t, \end{cases} \tag{2.6}$$

where ω, p, E and t is the revolution frequency, momentum, total energy and arrival time of the particle, respectively. Note that by definition $t_s = 0$ and $t = \Delta t$. As shown in [24], from this the time evolution of the energy difference $\Delta E/\omega_{\mathrm{rev}}$ can be derived to be

$$\frac{d}{dt}\left(\frac{\Delta E}{\omega_{\mathrm{rev}}}\right) = \frac{1}{2\pi} q V \left(\sin\phi - \sin\phi_s\right) \;, \tag{2.7}$$

which is our first equation of motion for the particles in the longitudinal plane, often referred

to as *kick* equation. According to the same derivation [24], the second equation of motion, also called the drift equation, describing time evolution of the phase is found to be

$$\frac{d\phi}{dt} = \frac{h\omega_{\text{rev}}^2\eta}{\beta_s^2 E_s}\left(\frac{\Delta E}{\omega_{\text{rev}}}\right) \tag{2.8}$$

where η is know as the phase slip factor, or 'slippage factor'. The slippage factor is a function of the relative momentum offset $\delta \equiv \Delta p / p = \Delta E / (\beta_s^2 E_s)$. This property of the synchrotron describes how off-momentum particles will slip in frequency as they go around the accelerator. The slippage factor can be expanded as a series in δ;

$$\frac{\Delta\omega}{\omega_{\text{rev}}} = \frac{\omega - \omega_{\text{rev}}}{\omega_{\text{rev}}} \equiv \eta(\delta)\delta = -\left(\eta_0 + \eta_1\delta + \eta_2\delta^2 + O\left((\delta^3)\right)\right)\delta. \tag{2.9}$$

If the relative momentum offset is sufficiently small then only η_0 is kept. The zeroth-order phase slip factor can also be written as $\eta_0 = \alpha_0 - \frac{1}{\gamma_s^2}$, where α_0 is known as the zeroth order momentum compaction factor and γ_s is the relativistic γ-factor of the synchronous particle. Both η and α are determined by the magnetic lattice of the accelerator. It is also worth remarking that the momentum compaction factor can be rewritten to $\alpha_0 = 1/\gamma_t^2$, where γ_t is the relativistic gamma at transition energy. Below this transition energy, more energetic particles will arrive at the cavity sooner than the synchronous particle. However, as the particles gain energy, they will gain less velocity for every unit of energy. Above transition energy, the gain in velocity will be so small that it cannot make up for the longer orbit the more energetic particles have. Hence, the particles with slightly higher energy will arrive later to the cavity above transition.

Eqs. (2.7) and (2.8) constitute the equations of motion in longitudinal beam dynamics and they can be joined into a Hamiltonian of

$$H = \frac{1}{2}\frac{h\eta\omega_{\text{rev}}^2}{\beta_s^2 E_s}\left(\frac{\Delta E}{\omega_{\text{rev}}}\right)^2 + \frac{qV}{2\pi}\left[\cos\phi - \cos\phi_s + \left(\phi - \phi_s\right)\sin\phi_s\right], \tag{2.10}$$

with $\Delta E / \omega_s$ and ϕ as the conjugate variables. The first term in Eq. (2.10) is the kinetic energy of the system and the second is the potential energy from a single RF system. The second term defines the potential well that the particles see when passing through the RF cavities. Exposed to these potential wells, the beam particles group into so-called bunches, as depicted in Fig. 2.2. The collection of multiple bunches that are transferred from one accelerator to another at the same time is known as a batch. It is also worth noting that a single RF system refers to the situation derived above where all the RF cavities have the same RF frequency. This might not be the case in all accelerators; for instance, in the Super Proton Synchrotron, a higher harmonic is used in addition to the main one in order to stabilize the bunches.

From Eq. (2.10) it is possible to to show that the motion of some particles will describe bound trajectories in phase-space. The lines that separate the bound and unbound trajectories in phase-space is known as the separatrix, and in the context of longitudinal beam dynamics these boarders are referred to as RF buckets, see Fig. 2.3. The synchronous point of these RF
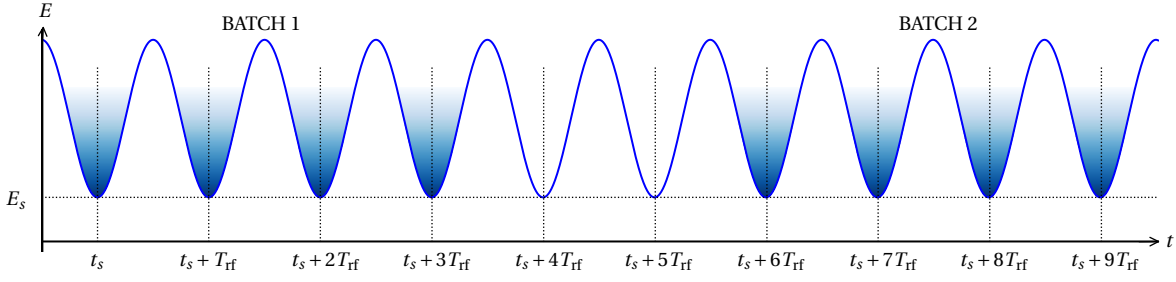
Figure 2.2: Illustration of the potential wells that the charged particles in the accelerator experience when passing through the RF cavities. The blue color indicates that the region is filled with a bunch. Groups of adjacent bunches are often referred to as batches.

buckets correspond to the minima of the aforementioned potential wells and all particles in the beam are bunched into these buckets, since all other orbits would be unstable.

The distribution of particles in phase space can vary depending on the mode of operation of an accelerator. A common distribution type is the binomial bunch distribution [25]

$$F(J) = F_0 \left(1 - \frac{J}{J_0} \right)^\mu . \tag{2.11}$$

where μ is the binomial exponent, F_0 is some normalization factor of the distribution and J_0 is the value of the action J along the trajectory that encloses all particles. This corresponds to a longitudinal line density of

$$\lambda(t) = \lambda_0 \left(1 - \left(\frac{t}{\tau_{\text{full}}/2} \right) \right)^{\mu + \frac{1}{2}} , \tag{2.12}$$

where τ_{full} is the full bunch length of the distribution, i.e. the bunch length enclosing all particles in the bunch. λ_0 is some normalization factor and is found by normalizing $\lambda(t)$ to one. Another particle distribution that will be used in this thesis is the bigaussian distribution given as

$$F(J) = F_0 e^{-2J/J_0} , \tag{2.13}$$

where J_0 is the value of the action J along the trajectory that encloses 4σ ($\approx 95\,\%$) of the particles. This distribution is gaussian in both energy and time, meaning that the corresponding line density is

$$\lambda(t) = \lambda_0 e^{-t^2/2\sigma^2} , \tag{2.14}$$

where σ is the standard deviation for a gaussian distribution. The bunch length τ_b is defined as

$$\tau_b = \frac{2}{\sqrt{2\ln 2}} \tau_{\text{FWHM}} , \tag{2.15}$$

where τ_{FWHM} is the bunch length measured using full width at half maximum.
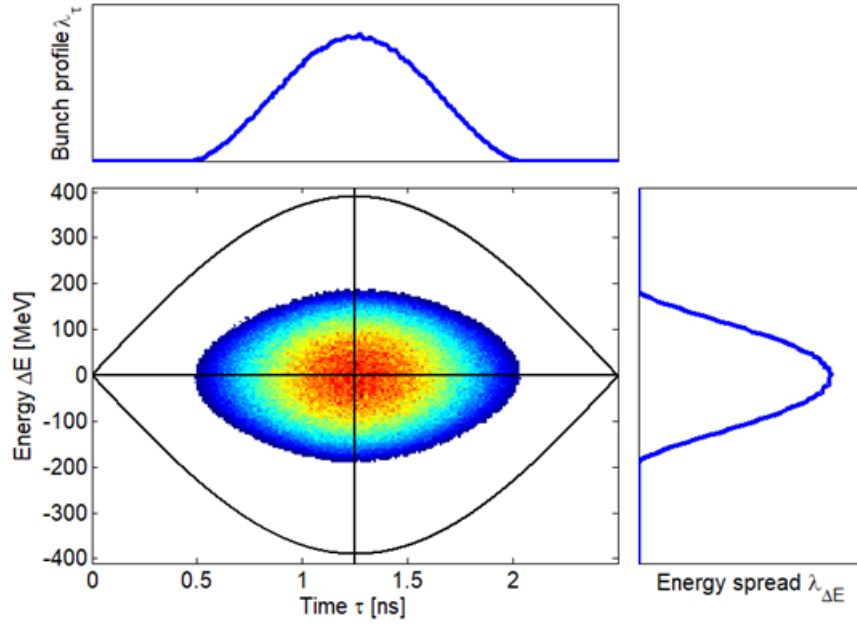
Figure 2.3: An example of a bunch in a RF bucket in phase-space.

Using the conjugate variables $\left(\frac{\Delta E}{\omega_{\text{rev}}}, \phi\right)$, the longitudinal emittance ε_b is given as

$$\varepsilon_b = \oint_{\mathscr{C}} \frac{\Delta E}{\omega_{\text{rev}}}(\phi) d\phi. \tag{2.16}$$

The contour $\mathscr{C}$ is along a constant value of the Hamiltonian and crossing the point ($\frac{\Delta E}{\omega_0} = 0, \phi = \phi_b$) in phase-space. ϕ_b is half of the bunch length τ_b in degrees, i.e. $2\phi_b = \omega_{\text{rf}} \tau_b$.

Until this point we have only handled the interaction between single particles and the RF system. However in the real machine the particles will interact electromagnetically with each other and with machine elements; these interactions are called collective effects.

In this context, the machine can be characterized by its electrical impedance. When the charged particles travel through various machine parts along their path, they will induce electromagnetic fields caused by interaction with the impedance of these parts. Each ultra-relativistic particle will experience half of their own induced voltage. In addition, the trailing particles, will also experience the induced voltage of all the particles in front. The total impedance can be described by the function $Z(\omega)$ [26, 27], which is frequency-dependent, or by its Fourier image, the wake function $W(t)$. The beam-induced voltage from a beam with a longitudinal line density of $\lambda(t)$ can be computed both through the use of the wake function

$$V_{\text{ind,beam}}(t) = q \int_{-\infty}^{\infty} d\tau \, \lambda(\tau) W(t - \tau) \tag{2.17}$$

11

or through the impedance

$$V_{\text{ind,beam}}(t) = q \int_{-\infty}^{\infty} d\omega \Lambda(\omega) Z(\omega) e^{i\omega t} , \tag{2.18}$$

where $\Lambda(\omega)$ is the spectrum or Fourier transform of the beam profile $\lambda(t)$.

2.2.1 Implementation in BLonD

For practical reasons, the BLonD (Beam Longitudinal Dynamics) simulator uses the energy-offset $\Delta E_{(n)}$ and time-offset $\Delta t_{(n)}$ coordinates, where the index n denotes turn n around the accelerator. This pair of conjugate variables describes the difference in energy and time of arrival of a given particle relative to the synchronous (design) energy $E_{s,(n)}$ and reference time $t_{s,(n)}$ at turn n. Notice that the phase-space coordinates are calculated on a turn by turn basis. The reference time is defined as

$$t_{s,(0)} \equiv 0 \ \text{ and } \ t_{s,(n)} \equiv \sum_{k=0}^{n} T_{\text{rev},(k)} \ \text{ for } \ n \geq 1 , \tag{2.19}$$

where the revolution period of the design particle for turn n is given as $T_{\text{rev},(n)} = 2\pi/\omega_{\text{rev},(n)}$. Additionally, the revolution period of the design particle can be expressed as

$$T_{\text{rev},(n)} = \frac{2\pi R_s}{\beta_{s,(n)} c} \tag{2.20}$$

through the average design orbit radius R_s around the synchrotron and the relativistic beta $\beta_{s,(n)}$ of the design particle at turn n.

In reality, a single particle bunch could contain billions or trillions of particles. It would therefore take a lot of computational power to simulate the real amount of particles. For this reason BLonD tracks macro-particles, where each macro-particle is equivalent to a given number of physical particles.

The energy of the particles for turn $n + 1$ is given as

$$\begin{aligned} \Delta E_{(n+1)} &= \Delta E_{(n)} + q \sum_{k=0}^{n_{\text{rf}}} V_{k,(n)} \sin\left(\omega_{\text{rf},k,(n)} \Delta t_{(n)} + \varphi_{\text{rf},k,(n)}\right) \\ &- \left(E_{s,(n+1)} - E_{s,(n)}\right) + E_{\text{other},(n)}, \end{aligned} \tag{2.21}$$

and is the equivalent of Eq. (2.7) in the BLonD notation. The first term is the particle energy in turn n, the second term is the sum of voltage kicks from different harmonic RF systems and the third term is the change in synchronous energy. Finally, the last term comes from all other possible contributions to the particle energy (depending on the simulation), e.g. synchrotron radiation and/or induced voltages from other particles. The arrival time of a given particle,

$\Delta t_{(n+1)}$, relative to the reference time at turn $n+1$ is found through the *drift* equation

$$\Delta t_{(n+1)} = \Delta t_{(n)} + T_{\text{rev},(n+1)} \left[\left(1 + \alpha_{0,(n+1)} \delta_{(n+1)} + \alpha_{1,(n+1)} \delta_{(n+1)}^2 \right. \right.$$
$$\left. \left. + \alpha_{2,(n+1)} \delta_{(n+1)}^3 \right) \frac{1 + \frac{\Delta E_{n+1}}{E_{d,(n+1)}}}{1 + \delta_{(n+1)}} - 1 \right] . \tag{2.22}$$

Notice that the momentum compaction factor α is expanded in orders of relative momentum offset $\delta_{(n+1)}$ and used instead of the slippage factor η. To third order, they are related to each other through the following set of equations

$$\eta_0 = \alpha_0 - \frac{1}{\gamma_s^2} \tag{2.23}$$

$$\eta_1 = \frac{3\beta_s^2}{2\gamma_s^2} + \alpha_1 - \alpha_0 \eta_0 \tag{2.24}$$

$$\eta_2 = -\frac{\beta_s^2 (5\beta_s^2 - 1)}{2\gamma_s^2} + \alpha_2 - 2\alpha_0 \alpha_1 + \frac{\alpha_1}{\gamma_s^2} + \alpha_0^2 \eta_0 - \frac{3\beta_s^2 \alpha_0}{2\gamma_s^2} . \tag{2.25}$$

Finally, the induced voltage generated by the beam that interacts with the machine impedance is computed using the Discrete Fourier Transform (DFT) and Inverse Discrete Fourier Transform (IDFT) [28]. Using these discrete transformations, the induced voltage can be computed as

$$V_{\text{ind}}[n] = -q \, \text{IDFT} \left(Z[k] \Lambda[k] \right) \tag{2.26}$$

or

$$V_{\text{ind}}[n] = -q \, \text{IDFT} \{ \text{DFT} \left(W[n] \right) \text{DFT} \left(\lambda[n] \right) \} \tag{2.27}$$

given that the beam profile is adequately zero-padded to resolve the machine impedance. Which method to use depends on the nature of the simulation, due to the fact that different methods have different numerical limitations in terms of runtime and accuracy.

2.3 Power Limitations at HL-LHC Injection

The LHC RF system has two operational beam-loading compensation schemes. In the half-detuning scheme [22], the RF voltage is kept constant in both amplitude and phase, and as mentioned, in this scheme, a significant part of the RF power is used for beam-loading compensation. On the other hand, during the ramp and flattop the RF cavities are operated in the a full-detuning scheme [29, 30], which is also the baseline for HL-LHC intensities. In the full-detuning scheme, the RF voltage amplitude is constant while the phase is allowed to slip. This allows for the RF bucket to position itself where the bunches with beam loading would naturally sit, and significantly reduced the RF power consumption. Unfortunately, at injection the half-detuning scheme is still the most power-efficient option, since the bunches from the SPS arrive equispaced. This is why the LHC RF system is limited at injection for HL-LHC intensities.

Another way of reducing the power consumption at injection is to reduce the RF voltage.

However, as we have seen, the SPS itself has to increase the flat top bunch length as much as possible for beam stability, and so the bunch length of the SPS beam injected is already at the limit of what the twice as short LHC RF bucket can capture. To limit capture losses, the LHC injection voltage has to be much larger than matched. For 2018 beam parameters with an SPS bunchlength of 1.5 ns and flattop RF voltage of 7 MV, the matched LHC voltage would be 1.9 MV (see App. C), while the minimum voltage acceptable for beam losses was found to be 4 MV [31]. The LHC design report [23] even foresaw a capture voltage of 8 MV for nominal beams.

To come up with solutions to the RF power limitations and to optimize operational schemes for the HL-LHC era, an accurate and detailed simulation model is needed, which is capable of reproducing present beam observations and can be scaled to increased intensities. Such simulations require describing the beam transfer from the SPS to the LHC and the LHC flat-bottom evolution.

At SPS flat top, realistic beam distributions have to be generated. Particularly the halo of the bunches need to be well described as they are a source of particle losses. This is achieved by collective effects and the cavity control loops of the SPS, consisting a one-turn delay feedback (OTFB) and a feed-forward (FF). The OTFB regulates the antenna voltage in the SPS TWCs to the set point voltage and reduces the effective impedance of the cavity as seen by the beam. The FF is used to attenuate the real part of the TWC impedance towards the beam and is used in combination with the OTFB to boost its performance. At the same time, the cavity loops redistribute the bunch-by-bunch position of the beam. This strongly influences the beam losses at injection, which is of central interest to do HL-LHC injection studies.

To accurately describe the RF power consumption at LHC flat bottom, the beam dynamics in the presence of cavity controllers and beam losses at capture and along the flat bottom need to be modelled. The LHC cavity controller consists of two main components, an RF feedback (RFFB) and a one-turn delay feedback (OTFB).

2.4   Introduction to Control Loops

The control systems that will be handled in this thesis will be restricted to closed control systems. Closed control systems regulate some external parameter by using measurements of the parameter itself. The measurement is sent through the system that reacts with some designed response, and regulates the parameter. The system response can be characterized by the transfer function $h(t)$ in time-domain, also referred to as the response function. Consider the simple example in Fig. 2.4. The output signal $y(t)$ of the system is given by

$$y(t) = \int_{-\infty}^{\infty} h(\tau)x(t-\tau)d\tau \equiv h(t) * x(t), \tag{2.28}$$

where $x(t)$ is the input signal. The operator $*$ denotes the convolution.

For the analysis of control systems, it is often convenient to use of Laplace transforms [32]. The Laplace transform of a function $x(t)$ is defined as

$$X(s) = \mathscr{L}\{x(t)\} = \int_{0}^{\infty} x(t)e^{-st}dt. \tag{2.29}$$
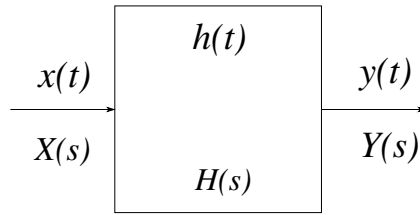
Figure 2.4: Block diagram of a signal $x(t)$ sent to some system $h(t)$ resulting in a response $y(t)$.

In Laplace domain, Eq. (2.28) simplifies the relation between the input and output signal to

$$Y(s) = H(s) \cdot X(s), \tag{2.30}$$

where $Y(s)$, $H(s)$, and $X(s)$ are the Laplace-domain images of the output signal, the transfer function, and the input signal, respectively. The simplification from a convolution in time-domain to a multiplication in Laplace-domain becomes especially useful for systems as in Fig. 2.5. This is a negative feedback system, in which the output signal $Y(s)$ is amplified by some gain G and subtracted from a reference signal $R(s)$ to produce an error signal $E(s)$, which is then sent through a system $H(s)$. Using the multiplicative property of the signals and the response function, it is possible to show that the output signal in Laplace-domain is

$$Y(s) = \frac{H(s)}{1 + GH(s)} R(s), \tag{2.31}$$

where G is referred to as the loop gain.
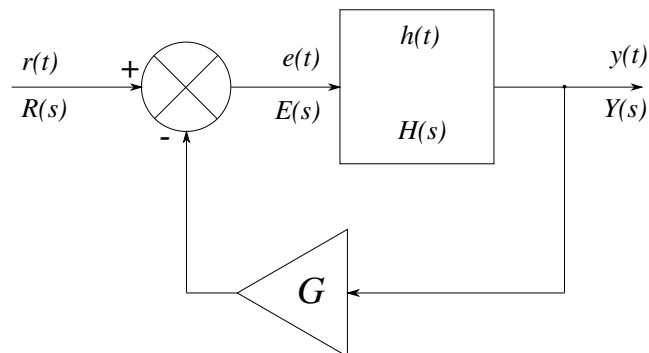
Figure 2.5: Block diagram of a negative feedback loop.

2.4.1 The Base-band Network Analyzer

One frequently used device to measure the transfer function of a complex control system is the base-band network analyzer (BBNA). This measurement device works by sending white

noise into some system and reading out the result signal at some other point in the system. The network analyzer is said to be on the base-band because the system frequency response is measured around the carrier frequency. In this thesis, the carrier frequency will always refer to the RF frequency. This measurement method can conveniently also be modeled in simulations, to compare measured and simulated transfer functions.

The frequency range that can be probed with a BBNA is $(-\frac{1}{2}f_{\max}, +\frac{1}{2}f_{\max})$, where $f_{\max}$ is given by the sampling time T_s at which the white noise is injected,

$$\Delta T_s = \frac{1}{2f_{\max}} \, . \tag{2.32}$$

Furthermore, since the the network analysis is done at base band, the frequency range will be centered around the base-band frequency. Although the frequency range of the measurement is limited by the sampling time, the resolution of the measurement can be improved by increasing the length of the injected white noise.

3 SPS Cavity Control

This chapter describes the SPS OTFB, its model implemented in BLonD, and the tests that were performed to validate and benchmark the model.

3.1 The SPS Travelling Wave Cavity

The SPS TWCs have a different impedance towards the amplifiers (or generators) than towards the beam. The total antenna voltage in the cavity will therefore consist of the sum of generator- (V_{gen}) and beam-induced (V_{beam}) voltages,

$$V_{\text{ant}} = V_{\text{gen}} + V_{\text{beam}}. \tag{3.1}$$

The generator-induced voltage can be written as [14]

$$V_{\text{gen}} = Ele^{i\phi} \frac{\sin\left(\frac{\tau(\omega-\omega_r)}{2}\right)}{\frac{\tau(\omega-\omega_r)}{2}} + \text{H.C.}, \tag{3.2}$$

where E is the peak electric field created by the generator, l is the accelerating length of the cavity, ϕ is the RF phase and ω_r is the resonant frequency of the cavity. Note that the TWCs cannot be actively tuned and have a fixed resonant frequency. In addition, 'H.C.' stands for the Hermitian conjugate and cavity filling time is given as

$$\tau = \frac{l}{v_g}\left(1 + \frac{v_g}{c}\right) \tag{3.3}$$

with v_g being the group velocity of the travelling electromagnetic wave and c being the speed of light. The beam, having a net electric charge, will interact with the cavity and also introduce an electrical field [14]:

$$E_{\text{beam}}(z) = -I_b \frac{\rho}{4} e^{-i\frac{\omega}{v}\left(z-\frac{l}{2}\right)} \frac{1 - e^{-i\tau(\omega-\omega_r)\frac{z}{l}}}{i\frac{\tau(\omega-\omega_r)}{l}} + \text{H.C.}. \tag{3.4}$$

Here, I_b is the RF beam current and ρ is the series impedance of the cavity per unit area. This electrical field has an associated voltage V_{beam}, which is summed with the expression in Eq. (3.2), to obtain the total RF voltage in the cavity

$$V_{\text{ant}} = V_{\text{gen}} + V_{\text{beam}}$$

$$= Ele^{i\phi} \frac{\sin\frac{\tau(\omega-\omega_r)}{2}}{\frac{\tau(\omega-\omega_r)}{2}} - I_b \frac{\rho l^2}{8} \left[\left(\frac{\sin\frac{\tau(\omega-\omega_r)}{2}}{\frac{\tau(\omega-\omega_r)}{2}} \right)^2 - i2 \frac{\tau(\omega-\omega_r) - \sin\tau(\omega-\omega_r)}{(\tau(\omega-\omega_r))^2} \right] + \text{H.C..} \quad (3.5)$$

From the above expression, the impedance of the cavity towards the generator is given by

$$Z_{\text{gen}}(\omega) = l\sqrt{\frac{\rho Z_0}{2}} \left[\frac{\sin\left(\frac{\tau(\omega-\omega_r)}{2}\right)}{\frac{\tau(\omega-\omega_r)}{2}} + \frac{\sin\left(\frac{\tau(\omega+\omega_r)}{2}\right)}{\frac{\tau(\omega+\omega_r)}{2}} \right], \quad (3.6)$$

where $Z_0 = 50\,\Omega$ is the matched impedance. In addition, the impedance of the cavity towards the beam is given by

$$Z_{\text{beam}}(\omega) = \frac{\rho l^2}{8} \left[\left(\frac{\sin\left(\frac{\tau(\omega-\omega_r)}{2}\right)}{\frac{\tau(\omega-\omega_r)}{2}} \right)^2 - 2i \frac{\tau(\omega-\omega_r) - \sin(\tau(\omega-\omega_r))}{(\tau(\omega-\omega_r))^2} \right.$$

$$\left. + \left(\frac{\sin\left(\frac{\tau(\omega+\omega_r)}{2}\right)}{\frac{\tau(\omega+\omega_r)}{2}} \right)^2 + 2i \frac{\tau(\omega+\omega_r) - \sin(\tau(\omega+\omega_r))}{(\tau(\omega+\omega_r))^2} \right] \quad (3.7)$$

from Eq. (3.5). The resulting impedance from all the TWCs in the SPS seen by the beam is found in Fig. 3.1. Each TWC consists of multiple sections, and in each section there are 11 accelerating cells, while the first and last cell of each cavity only give half of the accelerating field. Table 3.1 shows the central parameters of the three- and four-section SPS TWCs. Note that the resonant frequencies in the table are taken from the most recent measurement done on the TWCs, which was done in 2021 [33]. This aspect of the TWCs will be discussed later.

Table 3.1: Table of values for the three- and four-section SPS TWCs. All parameters are from the original design of the TWCs expect for the resonant frequencies, which are taken from the most recent measurements done in 2021.

variable	3-section	4-section
n_{cavities}	4	2
l	32×0.374 m	43×0.374 m
v_g/c	0.0946	0.0946
τ	462 ns	621 ns
ρ	27.1 kΩ/m^2	27.1 kΩ/m^2
f_r	200.038 MHz	199.995 MHz
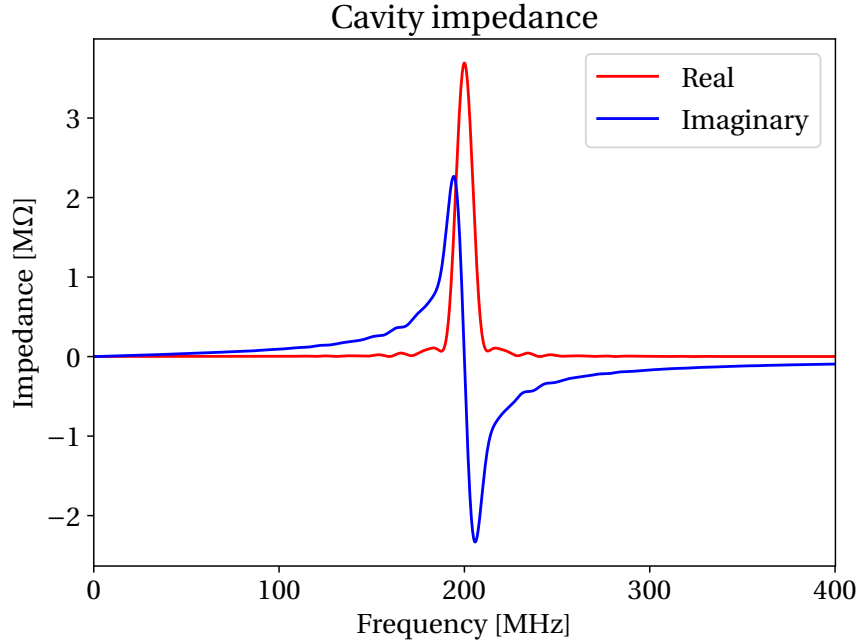
Figure 3.1: A plot of the real and imaginary part of the impedance of the SPS 200 MHZ travelling wave cavity.

3.2   The SPS One-Turn Delay Feedback and Feed-Forward Models

In this section, we will introduce the main parts of the SPS cavity controller model and how they are implemented numerically in BLonD package `cavity_control`. This implementation uses the design in [34].

3.2.1   Low Power-Level Radio Frequency System

In the simulation model, the SPS OTFB is divided into three units, namely, the generator-, LLRF- and beam-parts, see Fig. 3.2. It utilizes complex, time-domain signals that span one turn with h samples per turn and is thus intrinsically sampled at the RF frequency.

LLRF Unit

The LLRF unit in Fig. 3.2 is where the error signal dV_{gen} of this negative feedback is calculated as the difference between the measured antenna voltage and the set point voltage

$$dV_{\mathrm{gen}} = V_{\mathrm{set}} - V_{\mathrm{ant}}, \tag{3.8}$$

This signal is then amplified by the LLRF gain, G_{llrf} and sent through a comb filter. The purpose of this filter is to reduce the effective impedance at the multiples of the revolution frequency. This is done by doing a weighted sum of the current turn signal with the output signal from the comb filter of the previous turn,

$$dV_{\mathrm{gen,out,n}} = \alpha_{\mathrm{comb}} dV_{\mathrm{gen,out,n\text{-}1}} + (1 - \alpha_{\mathrm{comb}}) \, dV_{\mathrm{gen,in,n}}, \tag{3.9}$$

SPS One Turn Feedback
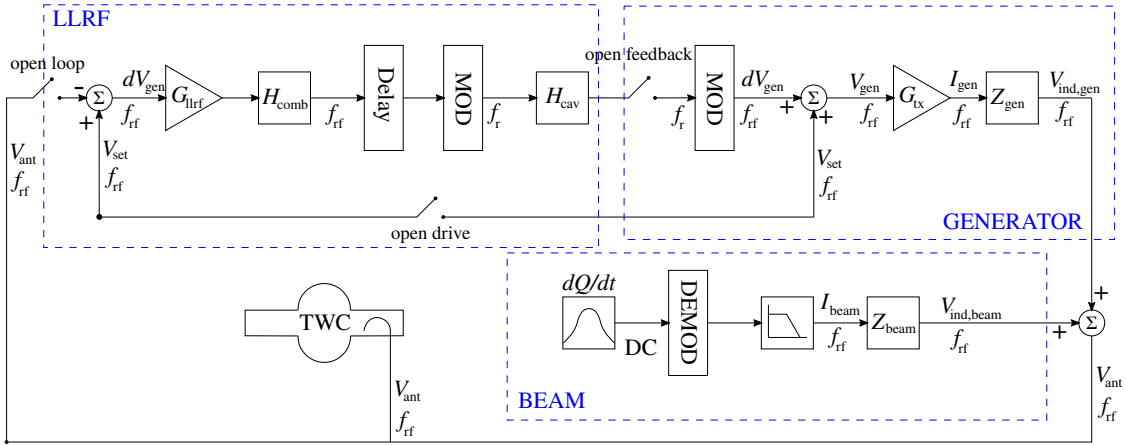
Figure 3.2: Schematic for the BLonD model that is used to describe the OTFB used in the SPS.

where n denotes the turn counter and α_{comb} is the comb filter coefficient. A complementary delay of $T_{\text{rev}} - \tau$ is then introduced to the signal that will add up later with the τ delay due to the cavity filling time, ensuring that the correction happens exactly one turn later. Lastly, the signal is modulated from the RF frequency to the cavity resonant frequency and filtered through the cavity response H_{cav}. The modulation of the signal can be formulated mathematically as

$$\begin{bmatrix} V_{\text{I,out}}(t) \\ V_{\text{Q,out}}(t) \end{bmatrix} = \begin{bmatrix} \cos\left((\omega_{\text{rf}} - \omega_{\text{r}})\,t + \phi\right) & -\sin\left((\omega_{\text{rf}} - \omega_{\text{r}})\,t + \phi\right) \\ \sin\left((\omega_{\text{rf}} - \omega_{\text{r}})\,t + \phi\right) & \cos\left((\omega_{\text{rf}} - \omega_{\text{r}})\,t + \phi\right) \end{bmatrix} \begin{bmatrix} V_{\text{I,in}}(t) \\ V_{\text{Q,in}}(t) \end{bmatrix}. \tag{3.10}$$

When modulating the signal, the RF phase ϕ_{rf} and the phase offset at the end of a one-turn modulated signal $\phi_{\text{mod,0}}$ is taken into account by setting $\phi = \phi_{\text{mod,0}} + \phi_{\text{rf}}$ in Eq. 3.10.

The cavity filter, H_{cav}, is modeled as a moving average over $K = \text{int}(\omega_{\text{rf}}\tau)$ samples,

$$dV_{\text{gen,out,k}} = \frac{1}{K} \sum_{i=k-K}^{k} dV_{\text{gen,in,i}} \tag{3.11}$$

and results therefore in a delay of τ on the signal.

Generator Unit

In the generator unit of Fig. 3.2, the error signal and the set point is used to compute the generator-induced voltage in the cavity. Firstly, the error signal is modulated back to the RF frequency using Eq. (3.10) and exchanging ω_{rf} and ω_{r} in the matrix. When modulating back to the RF frequency, the phase offset caused by the cavity filter delay τ is taken into account by setting $\phi = (\omega_{\text{rf}} - \omega_r)\,\tau - \phi_{\text{mod,0}} - \phi_{\text{rf}}$ in Eq. (3.10). The error signal is then summed up with the set point voltage to give the generator signal V_{gen}. Next, the generator current, I_{gen} is found

through

$$I_{\text{gen}} = G_{\text{tx}} \frac{V_{\text{gen}}}{R_{\text{gen}}}, \tag{3.12}$$

where G_{tx} is the transmitter gain and R_{gen} is a resistance given by

$$R_{\text{gen}} \equiv l \sqrt{\frac{\rho Z_0}{2}}. \tag{3.13}$$

Using the I/Q representation of the signals, the induced voltage through a response component can be written as a matrix convolution

$$\begin{bmatrix} V_I(t)) \\ V_Q(t)) \end{bmatrix} = \begin{bmatrix} h_s(t) & -h_c(t) \\ h_c(t) & h_s(t) \end{bmatrix} * \begin{bmatrix} I_I(t) \\ I_Q(t) \end{bmatrix}. \tag{3.14}$$

Again, the $*$-operator denotes a convolution and should be interpreted as taking the convolution between each product resulting from matrix multiplication. The matrix in Eq. (3.14) is known as an impulse response matrix. In the case of the generator-induced voltage, the current in Eq. (3.14) is the generator current and the elements of the impulse response matrix are given by

$$h_{s,\text{gen}}(t) = \frac{R_{\text{gen}}}{\tau} \text{rect}\left(\frac{t}{\tau}\right) \cos\left((\omega_{\text{rf}} - \omega_{\text{r}})\, t\right) \tag{3.15a}$$

$$h_{c,\text{gen}}(t) = -\frac{R_{\text{gen}}}{\tau} \text{rect}\left(\frac{t}{\tau}\right) \sin\left((\omega_{\text{rf}} - \omega_{\text{r}})\, t\right), \tag{3.15b}$$

where $\text{rect}\left(\frac{t}{\tau}\right)$ is the rectangular function defined in Eq. (B.4). Equation (3.15) can be derived from the expression for Z_{gen} in Eq. (3.6), which is done in [34].

Beam Unit

Lastly, we have the beam box in Fig. 3.2. This part of the model computes the beam-induced voltage from the longitudinal charge profile of the beam. First the RF beam current is found by

$$\begin{pmatrix} I_{\text{I,beam},i} \\ I_{\text{Q,beam},i} \end{pmatrix} = 2 \frac{Q_i}{T_s} \begin{pmatrix} \cos(\omega_{\text{rf}} t_i + \phi) \\ -\sin(\omega_{\text{rf}} t_i + \phi) \end{pmatrix}, \tag{3.16}$$

where i denotes the sample number, T_s is the sampling time, Q_i is the charge at bin i, t_i is the longitudinal position of the sample and ϕ is the phase between the first sample of the beam profile and the RF wave.

In the same way as in the generator-induced voltage calculation, the beam-induced voltage is found through Eq. (3.14). However, the difference is that the current is the RF beam current I_{beam} and the elements of the impulse response matrix, found through the expression for

Z_{beam} in Eq. (3.7), are given by

$$h_{s,\text{beam}}(t) = \frac{2R_{\text{beam}}}{\tau} \text{tri}_R\left(\frac{t}{\tau}\right) \cos\left((\omega_{\text{rf}} - \omega_r)t\right) \qquad (3.17\text{a})$$

$$h_{c,\text{beam}}(t) = -\frac{2R_{\text{beam}}}{\tau} \text{tri}_R\left(\frac{t}{\tau}\right) \sin\left((\omega_{\text{rf}} - \omega_r)t\right). \qquad (3.17\text{b})$$

In the equations $R_{\text{beam}} \equiv \frac{\rho l^2}{8}$ and $\text{tri}_R\left(\frac{t}{\tau}\right)$ is the right triangular function as defined in Eq. (B.2). Finally, the beam-induced voltage $V_{\text{ind,beam}}$, is combined with the generator-induced voltage, $V_{\text{ind,gen}}$, to give the total antenna voltage

$$V_{\text{ant}} = V_{\text{ind,beam}} + V_{\text{ind,gen}}, \qquad (3.18)$$

which is the total voltage in the TWCs that the beam particles experience.

3.2.2 Feed-Forward Model

In addition to the OTFB, the SPS cavity controller also has a FF circuit. This FF measures the RF beam current through a pick-up and filters it with the FF response $H_{\text{ff}}(\omega)$

$$I_{\text{gen}}^{\text{comp}}(\omega) = H_{\text{ff}}(\omega) I_{\text{beam}}(\omega). \qquad (3.19)$$

Then, the filtered signal is sent to the generator to compensates part of the induced voltage by the beam. In an ideal world, the FF would perfectly compensate the beam-induced voltage [34]

$$Z_{\text{gen}}(\omega) I_{\text{gen}}^{\text{comp}}(\omega) = -Z_{\text{beam}}(\omega) I_{\text{beam}}(\omega). \qquad (3.20)$$

The FF filter is implemented as a finite-impulse response (FIR) filter, with the optimal response determined by the requirement

$$Z_{\text{gen}}(\omega) H_{\text{ff}}(\omega) = -Z_{\text{beam}}(\omega). \qquad (3.21)$$

However, since Z_{gen} is purely real and Z_{beam} is complex, only the real part of Z_{beam} can be perfectly compensated by the real part of $H_{\text{ff}}(\omega)$. The imaginary part of Z_{beam}, on the other hand, cannot be fully compensated. As is the case in the designed FF system [34], the SPS beam is assumed to change little from turn to turn, hence the FF acts the one turn after the measurement.

3.2.3 Feeding OTFB Corrections into Particle Tracking

Without the OTFB present in the code, the RF voltage that the particles in the simulations will see is given by

$$V_{\text{eff}}(t) = |V_{\text{rf}}| \sin\left(\omega_{\text{rf}} \Delta t + \varphi_{\text{rf}}\right), \qquad (3.22)$$

where V_{RF} and φ_{RF} are scalar user inputs defining the set point voltage of the OTFB. However, when the OTFB is active the particles will in reality see the antenna voltage

$$V_{\mathrm{eff}}(t) = |V_{\mathrm{ant}}(t_n)| \sin\big(\omega_{\mathrm{rf}}\Delta t + \varphi_{\mathrm{ant}}(t_n)\big), \tag{3.23}$$

that is sampled at the positions t_n. By defining a correction voltage V_{corr} as

$$|V_{\mathrm{ant}}|\, e^{i(\varphi_{\mathrm{ant}} - \pi/2)} = |V_{\mathrm{corr}}|\, e^{i(\varphi_{\mathrm{corr}} - \pi/2)}\, |V_{\mathrm{set}}|\, e^{i(\varphi_{\mathrm{set}} - \pi/2)} \tag{3.24}$$

and using the fact that the set point in the OTFB is equal to the uncorrected RF voltage in the tracker, we can express

$$V_{\mathrm{eff}}(t) = |V_{\mathrm{ant}}| \sin\big(\omega_{\mathrm{rf}}\Delta t + \varphi_{\mathrm{ant}}\big) = |V_{\mathrm{rf}}||V_{\mathrm{corr}}| \sin\big(\omega_{\mathrm{rf}}\Delta t + \varphi_{\mathrm{rf}} + \varphi_{\mathrm{corr}}\big), \tag{3.25}$$

where $|V_{\mathrm{corr}}| = |V_{\mathrm{ant}}|\,/\,|V_{\mathrm{set}}|$ and $\varphi_{\mathrm{corr}} = \varphi_{\mathrm{ant}} - \varphi_{\mathrm{set}}$. The amplitude $|V_{\mathrm{corr}}|$ and phase φ_{corr} is computed in the OTFB and applied to the effective voltage that the particles sees in the tracker through the expression given above.

3.3   Benchmarking the Beam-Induced Voltage

The beam-part of the OTFB models the voltage induced by the beam as it passes through the TWCs. The induced voltage computed from this model has to be consistent with the sign conventions in BLonD. In addition, the I/Q-signals must satisfy rotational invariance in the I/Q-plane. The following section will go through the most central properties that the OTFB model has to satisfy when the beam-induced part of the model is included.

3.3.1   Integration in BLonD

The impedance of the SPS TWCs is taken into account when using the SPS OTFB model. Thus without any feedback corrections (zero gain), the total voltage with the OTFB should be the same as using the analytical impedance model of the cavities. To make sure that the beam induced voltage computed from the OTFB was consistent with this analytical impedance model of the TWCs in BLonD, the resulting beam-induced voltage from the two models were compared. Figure 3.3 shows the beam-induced voltage obtained with the two different methods along with the beam profile. As desired, the two models coincide.

Another aspect to verify was the relative orientation of the antenna, generator-induced and beam-induced voltages in the I/Q-plane. These should resemble the vectors found in [14]. A phasor diagram depicting the orientation of the set point, antenna and generator voltages relative to each other is shown in Fig. 3.4. In Fig. 3.4, V_{set} is chosen to be on the positive imaginary axis, and V_{ant} correctly matches it. As it should be, $_{\mathrm{beam}}$ is in advance and V_{gen} lags behind w.r.t. V_{ant}.

3.3.2   Rotational Invariance of the I/Q-signals

As mentioned in Sec. 3.2.3, the phase of the cavity loop voltage corrections that are used for particle tracking is always taken with the respect to the phase of the set point voltage.
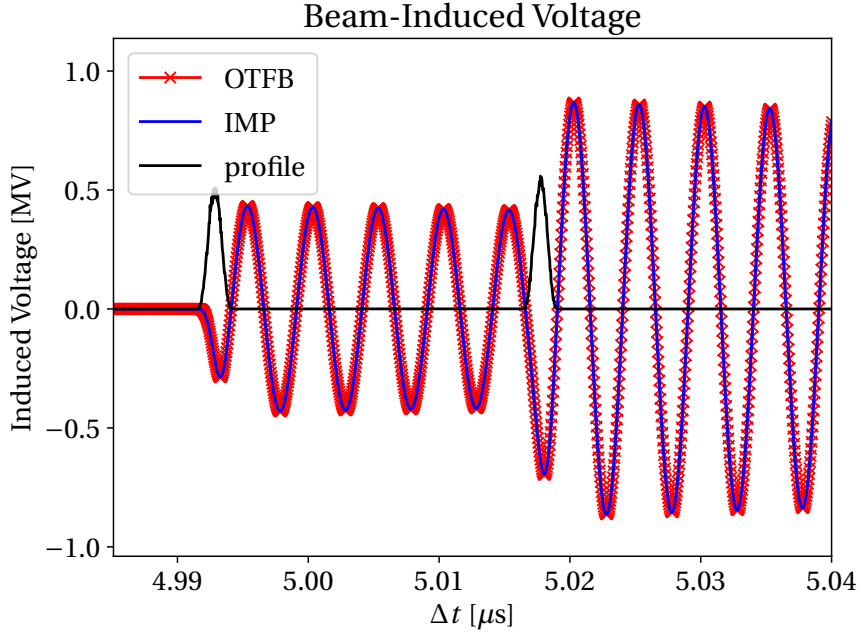
Figure 3.3: The beam-induced voltage from two bunches using the BLonD impedance model (IMP, blue) and the SPS OTFB model (OTFB, red).

A consequence of this is that the correction should be invariant if the set point voltage is rotated in the I/Q-plane as long as the beam-induced voltage is rotated with it. Hence, the generator-induced voltage and corrections should be invariant under the rotation of the set point and beam-induced voltages. This can be seen in Fig. 3.5. The I/Q vectors have the same relative orientation to each other, but are shifted by an overall phase of π.

3.4 SPS Full Machine

When benchmarking a numerical model, it is always good practice to come up with estimates from theory to compare with. The OTFB model is hard to solve analytically for the general time-dependent case. However, for the special case of a full machine, which is when the machine is filled with a bunch every fifth bucket, the OTFB-signals reach steady-state. This case can also be solved analytically with some additional assumptions.

3.4.1 Theoretical Estimates

The following derivation is based on the derivation found in [1]. Using Eq. (3.14), we can write the generator-induced voltage as

$$V_{I,\text{gen}} = h_{s,\text{gen}}(t) * I_{I,\text{gen}}(t) - h_{c,\text{gen}}(t) * I_{Q,\text{gen}}(t), \tag{3.26a}$$

$$V_{Q,\text{gen}} = h_{c,\text{gen}}(t) * I_{I,\text{gen}}(t) + h_{s,\text{gen}}(t) * I_{Q,\text{gen}}(t). \tag{3.26b}$$
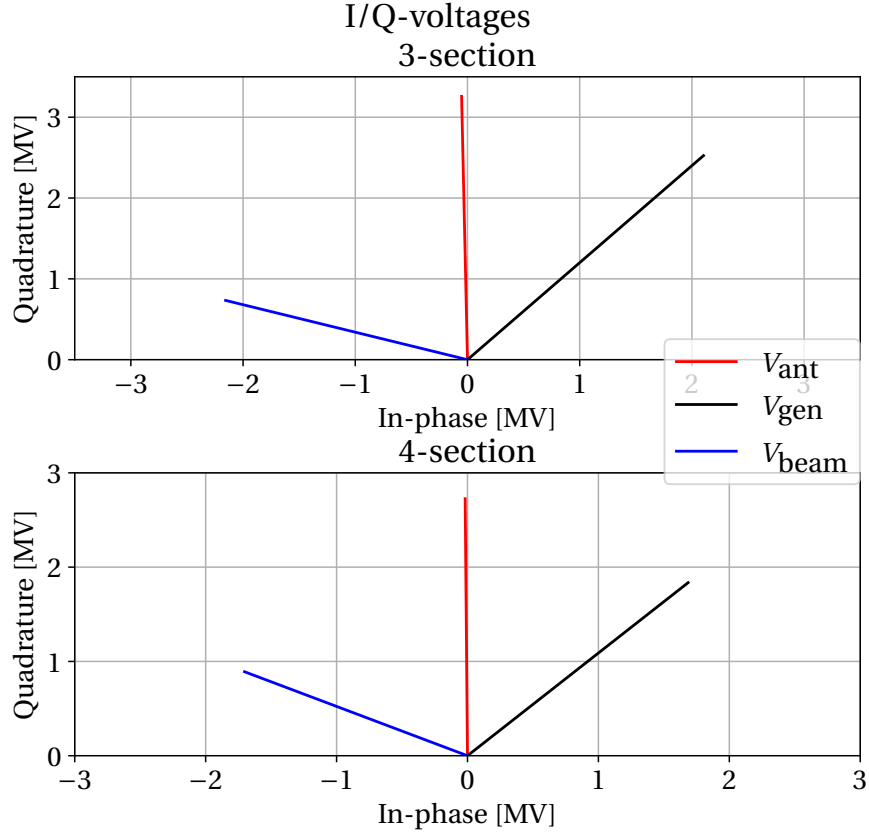
Figure 3.4: The antenna (red), generator-induced (black) and beam-induced voltages for the 3- and 4-section cavities in the SPS OTFB model after 100 turns of tracking.

When assuming steady state, all the currents become constant and the integrals in the convolutions simplify to integrals over the impulse response matrix elements. For the case of the generator the components become

$$h_{s,\text{gen}}(t) * I_{I,\text{gen}}(t) = \frac{I_{I,\text{gen}} R_{\text{gen}}}{\tau} \int_{-\tau/2}^{\tau/2} \cos(\Delta\omega t) dt = 2 \frac{I_{I,\text{gen}} R_{\text{gen}}}{\tau \Delta\omega} \sin\left(\Delta\omega \frac{\tau}{2}\right) \qquad (3.27)$$

and, by symmetry,

$$h_{c,\text{gen}}(t) * I_{Q,\text{gen}}(t) = \frac{I_{Q,\text{gen}} R_{\text{gen}}}{\tau} \int_{-\tau/2}^{\tau/2} \sin(\Delta\omega t) dt = 0, \qquad (3.28)$$

where we denoted $\Delta\omega \equiv \omega_{\text{rf}} - \omega_r$. Combining the above equations, we can express the generator-induced voltage in steady state as

$$V_{I,\text{gen}} = 2 \frac{R_{\text{gen}}}{\tau \Delta\omega} \sin\left(\Delta\omega \frac{\tau}{2}\right) I_{I,\text{gen}}, \qquad (3.29a)$$

$$V_{Q,\text{gen}} = 2 \frac{R_{\text{gen}}}{\tau \Delta\omega} \sin\left(\Delta\omega \frac{\tau}{2}\right) I_{Q,\text{gen}}. \qquad (3.29b)$$
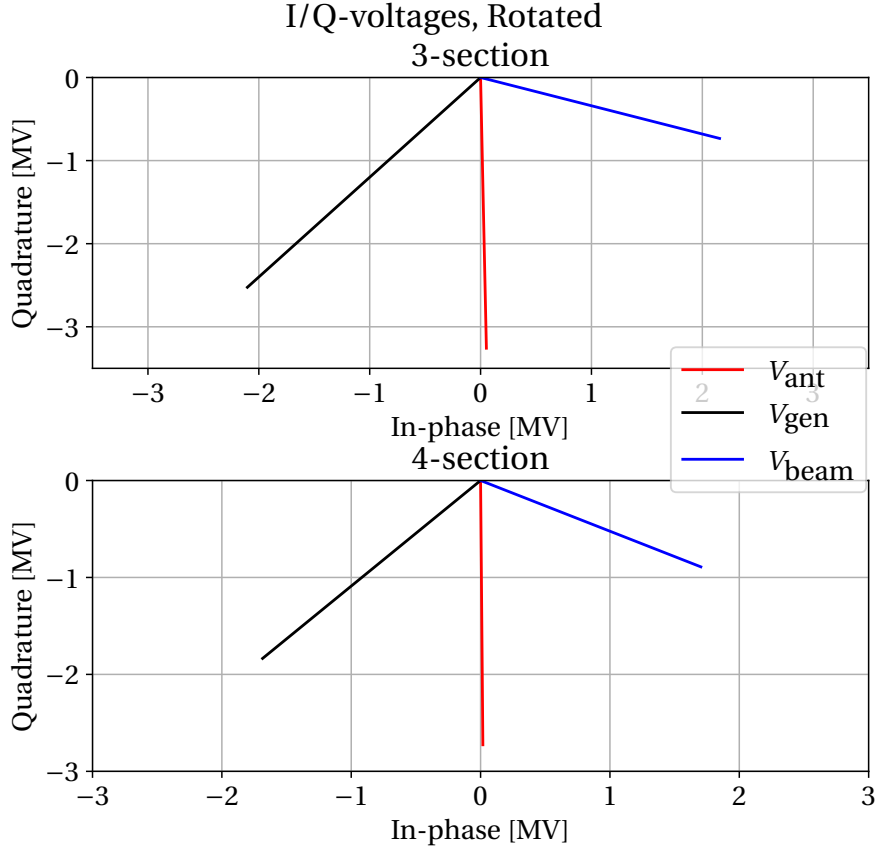
Figure 3.5: The antenna (red), generator-induced (black) and beam-induced voltages for the 3- and 4-section cavities in the SPS OTFB model after 100 turns of tracking. The phases of the set point and the beam-induced voltages are advanced by π in this plot.

To compute the beam-induced voltage we simplify the problem by assuming, without loss of generality, that the RF beam current is in-phase (purely real). This yields

$$V_{I,\text{beam}} = h_{s,\text{beam}}(t) * I_{I,\text{beam}}(t) \tag{3.30a}$$

$$V_{Q,\text{beam}} = h_{c,\text{beam}}(t) * I_{I,\text{beam}}(t) \tag{3.30b}$$

and through the use of the steady-state assumption, we obtain

$$h_{s,\text{beam}}(t) * I_{I,\text{beam}}(t) = I_{I,\text{beam}} \frac{2R_{\text{beam}}}{\tau} \int_0^\tau \left(1 - \frac{t}{\tau}\right)\cos\left(\Delta\omega t\right)dt \tag{3.31}$$

and

$$h_{c,\text{beam}}(t) * I_{I,\text{beam}}(t) = I_{I,\text{beam}} \frac{2R_{\text{beam}}}{\tau} \int_0^\tau \left(1 - \frac{t}{\tau}\right)\sin\left(\Delta\omega t\right)dt, \tag{3.32}$$

26

Hence, the beam-induced voltage in steady-state can be written as

$$V_{I,\text{beam}} = -\frac{2R_{\text{beam}}}{\tau^2 \Delta\omega^2} \left(1 - \cos\left(\Delta\omega\tau\right)\right) I_{I,\text{beam}} \tag{3.33a}$$

$$V_{Q,\text{beam}} = \frac{2R_{\text{beam}}}{\tau \Delta\omega} \left(1 - \frac{1}{\tau \Delta\omega} \sin\left(\Delta\omega\tau\right)\right) I_{I,\text{beam}}. \tag{3.33b}$$

To find the antenna voltage, we assume a perfect feedback with infinite gain. Hence, the antenna voltage is equal to the set point and get

$$V_{\text{set}} \approx V_{\text{ant}} = V_{\text{gen}} \qquad \text{without beam} \tag{3.34a}$$

$$V_{\text{set}} \approx V_{\text{ant}} = V_{\text{gen}} + V_{\text{beam}} \quad \text{with beam.} \tag{3.34b}$$

As mentioned earlier, the full SPS machine contains a bunch in every fifth bucket along the entire turn. This would give a peak RF beam current of

$$I_{I,\text{beam}} = \frac{2qN_p}{5T_{\text{rf}}} F, \tag{3.35}$$

where F is the form factor which depends on the bunch-by-bunch distribution, N_p is the number of particles per bunch and T_{rf} is the RF period. Note that in the short bunch approximation $F \approx 1$. Lastly, the power consumption of the generator is

$$P_{\text{gen}} = \frac{1}{2} Z_0 \left|I_{\text{gen}}\right|^2 \tag{3.36}$$

where $Z_0 = 50\ \Omega$ when the generator is matched.

3.4.2 Numerical Estimates

A static beam was used to obtain numerical estimates from the SPS OTFB model. The parameters that were used in the simulation can be found in Table 3.2. In addition, the settings used for the OTFB in these simulations are found in Table 3.3.

A full machine would result actually in an unstable beam. A static beam was used for this simulation because of this, which means that only the OTFB was tracked. Since the interest of this benchmark lies in the I/Q signals of the OTFB and the generator power, this was approach was reasonable. The bunch length of 1.2 ns gives a peak RF beam current of 2.75 A with a bigaussian beam profile. The peak value of the RF beam current was also used for the theoretical estimates in Eq. (3.33) to find the beam-induced voltage. The antenna, beam-induced and generator voltages from simulations and theory can be found in Fig. 3.6. The estimates for the generator power consumption can be found in Table 3.4.

Comparing the results from theory (Table 3.5) and simulation (Table 3.6), we see that there is good agreement between the theoretical prediction of the beam-induced and and simulations. The error in the beam-induced voltage is less than 1 % for both the 3- and 4-section, which means that the beam distribution is represented in a correct way. As for the generator-induced voltage, one can see that the Q-component has an error of less then 1 % for both cavities while I-component is roughly 4 % lower in simulations than in theory. This was

Table 3.2: Parameters for the full machine simulation that was compared against theoretical estimates.

Parameter	Symbol	Unit	Value
Set point voltage	V_{set}	MV	10.0
Antenna voltage	V_{ant}	MV	10.0
Synchronous momentum	p_s	GeV	450
Harmonic number	h	-	4620
Transition energy	γ_t	-	18.0
Synchronous phase	ϕ_s	-	0
Particles per bunch	N_b	p/b	2.3×10^{11}
Bunch length	τ_b	ns	1.2
Peak RF beam current	$I_{\text{RF, beam}}$	A	2.75

Table 3.3: OTFB settings for the full machine simulation that was compared against theoretical estimates.

Parameter	Symbol	Unit	3-section	4-section
Transmitter gain	G_{tx}	-	1	1
LLRF gain	G_{llrf}	-	20	20
Comb filter coefficient	α_{comb}	-	63/64	63/64
Central Frequency	f_r	MHz	200.222	200.222
Voltage partitioning	V_{part}	-	0.5172	0.4828
Number of cavities	n_{cavities}	-	4	2

found to be caused the small negative I-component to the simulated antenna voltage due the finite gain of the OTFB.

For the I/Q-components of the generator current, the discrepancy is larger than for the generator-induced voltage. The offset is caused by two effects. As mentioned above, we have the offset caused by the finite gain in the OTFB. Secondly, since the generator-induced voltage is proportional to generator current in Eq. (3.29), the phase of the generator current and the generator-induced voltage should be the same. Upon inspection of the values of in Table 3.6, we see that this is not the case in simulation. The generator current with beam has a phase of 55.1° (3-sec) and 59.1° (4-sec) while the generator-induced voltage with beam has a phase of 40.7° (3-sec) and 40.3° (4-sec). If we instead we look at the absolute value of these signals, the error is 2.8 % (3-sec) and 1.8 % (4-sec) for the current and 2.3 % (3-sec) and 2.1 % (4-sec) for the induced voltage. Hence, the length of the IQ vectors coincide better with theory and if it was not for the effect from the finite gain, one would expect these errors to be even smaller.

Using the simulated antenna voltages for the theoretical calculations, i.e. no longer assum-

Table 3.4: Transmitter forward power for a given cavity type at flattop. A bunch length of 1.2 ns was assumed, giving an RF peak beam current of $I_b = 2.75$ A. The total voltage was distributed in 51.72 % to the 3-section cavities and 48.28 % to the 4-section cavities. Theoretical estimate marked with * is computed using the generator currents in Table 3.7.

Configuration	3-section			4-section		
	Theory	Theory*	Sim	Theory	Theory*	Sim
Without beam	439.8 kW	442.8 kW	430.1 kW	863.5 kW	870.4 kW	853.7 kW
With beam	752.3 kW	717.9 kW	711.1 kW	1324.7 kW	1270.3 kW	1277.4 kW

Table 3.5: Theoretical estimates for the two cavity types at flattop. A bunch length of 1.2 ns was assumed, giving an RF peak beam current of $I_b = 2.75$ A. The total voltage was distributed in 51.72 % to the 3-section cavities and 48.28 % to the 4-section cavities.

Variable	3-section		4-section	
	I-component	Q-component	I-component	Q-component
V_{beam}	-5.23 MV	0.88 MV	-4.64 MV	1.06 MV
V_{gen} (with beam)	5.23 MV	4.29 MV	4.64 MV	3.77 MV
I_{gen} (without beam)	0	132.64 A	0	185.85 A
I_{gen} (with beam)	134.06 A	110.09 A	178.62 A	145.20 A

ing infinite gain in the OTFB, we get the values given in Table 3.7. As expected, the simulated generator-induced voltage has better agreement with this theoretical value. In fact, the error between simulation and this estimate is less than 1 % for both the I- and Q-components of the generator-induced voltage. On the other hand, there is still a component-wise difference in the generator current. Since the induced voltage agrees better with theory, this is likely caused by the convolution in simulation. However as expected, the error in the absolute value of the generator current with beam is now even lower, 0.5 % for the 3-section and 0.3 % for the 4-section cavities.

Finally, we compare simulated and theoretical power estimates, with and without beam, in Table 3.4. The simulations have an error w.r.t. the theoretical estimates (that assume an infinite gain) of 2.2 % (3-sec) and 1.1 % (4-sec) without beam and 5.5 % (3-sec) and 3.6 % (4-sec) with beam. The error with beam is likely caused by the small negative I-component mentioned above. If we compare simulations with the theoretical estimate with the finite gain effect, we get an error of 2.9 % (3-sec) and 1.9 % (4-sec) without beam and 0.9 % (3-sec) and 0.6 % (4-sec) with beam. It seems like simulations agree more with this estimate with beam, but less so without.

This can be explained in the following way. Let V_t be the generator-induced voltage from the theoretical estimate with infinite gain and V_s be the simulated one. The theoretical

Table 3.6: Numerical results for a given cavity type at flattop. A bunch length of 1.2 ns was assumed, giving an RF peak beam current of $I_b = 2.75$ A. The total voltage was distributed in 51.72 % to the 3-section cavities and 48.28 % to the 4-section cavities.

Variable	3-section		4-section	
	I-component	Q-component	I-component	Q-component
V_{beam}	-5.23 MV	0.88 MV	-4.64 MV	1.06 MV
V_{gen} (with beam)	5.01 MV	4.30 MV	4.47 MV	3.79 MV
I_{gen} (without beam)	-31.10 A	127.42 A	-58.00 A	175.46 A
I_{gen} (with beam)	97.60 A	138.25 A	114.72 A	194.77 A

Table 3.7: Theoretical estimates for the two cavity types at flattop with the antenna voltage taken from simulations. A bunch length of 1.2 ns was assumed, giving an RF peak beam current of $I_b = 2.75$ A. The total voltage was distributed in 51.72 % to the 3-section cavities and 48.28 % to the 4-section cavities.

Variable	3-section		4-section	
	I-component	Q-component	I-component	Q-component
V_{beam}	-5.23 MV	0.88 MV	-4.64 MV	1.06 MV
V_{gen} (with beam)	5.01 MV	4.31 MV	4.47 MV	3.79 MV
I_{gen} (without beam)	-5.52 A	132.97 A	-6.73 A	186.47 A
I_{gen} (with beam)	128.54 A	110.42 A	171.90 A	145.82 A

estimate is given as

$$V_t = I_t + iQ_t \tag{3.37}$$

and the simulated one as

$$V_s = I_s + iQ_s. \tag{3.38}$$

We can assume that $Q_s = Q_t$, which is reasonable if one considers the values in Table 3.5 and Table 3.6, and $I_s = I_t - \epsilon$, where ϵ is the small negative real part arising from the finite gain of the OTFB. Additionally, we set $I_t = |V_t|\cos\theta$ and $Q_t = |V_t|\sin\theta$ with θ being the angle to the in-phase axis. As shown in section A.2, the difference in length Δl of the two vectors is given by

$$\Delta l = \frac{\epsilon}{|V_t|}\cos\theta + O\left(\epsilon^2\right) \tag{3.39}$$

Since the angle is smaller with beam than without, the difference will be greater with beam.
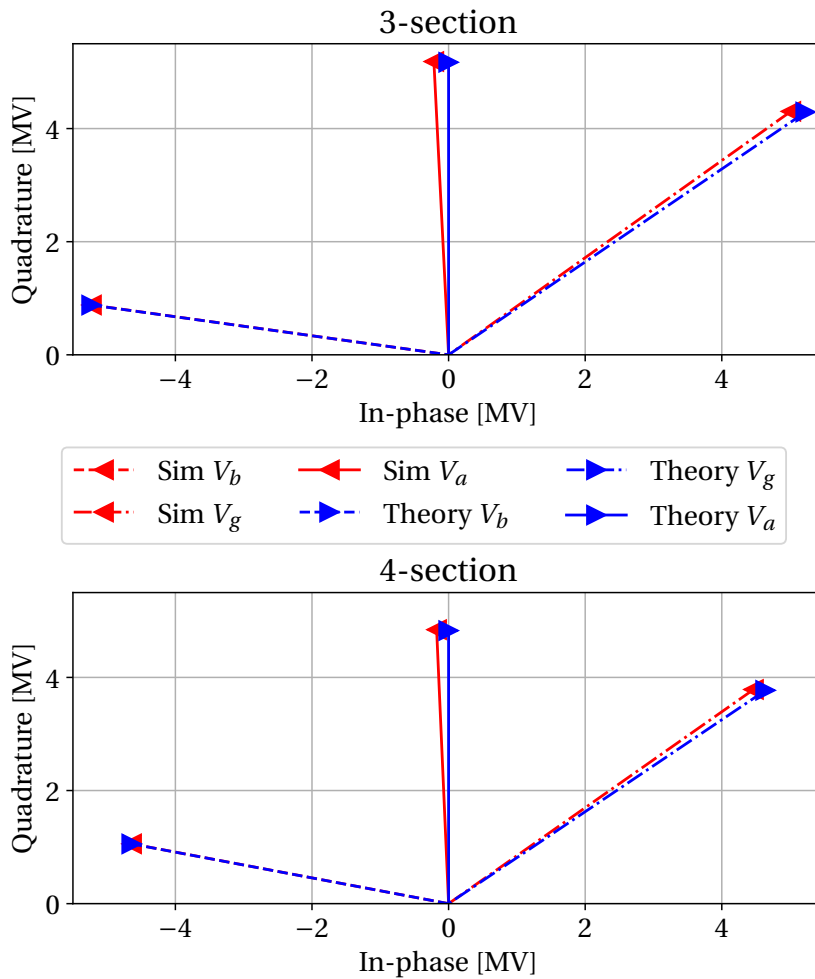
Figure 3.6: The IQ-vectors of the beam-induced, generator-induced and antenna voltages. The blue traces are from theory and the red are from simulations.

3.5 SPS OTFB Benchmark Against Measurements - Measurement Results

On November 6th 2021 measurements were performed on the HIRADMT2 cycle of the SPS with batched beam and the OTFB on and the FF off. Using the SPS OTFB simulation model, we aimed at reproducing the measurements as a final benchmark of the model. The following section walks through the acquisitions that were done, the conditions in the accelerator, how it the data was processed, compares simulation and measurement results, and details the error sources of the different measurements.

3.5.1 Measurement Conditions

The measurements used for benchmarking the OTFB were done on November 6th 2021 with a beam consisting of 4 batches with 72 bunches of 25 ns spacing (so-called 'standard' 25 ns

beam) at flat top. In addition to the profile measurements, various signals related to the OTFB were acquired for the six cavities (four 3-section cavities and two 4-section cavities). The exact measurement conditions are summarized in Table 3.8.

Table 3.8: Parameters of the HIRADMT2 cycle over which the measurements were performed.

Parameter	Symbol	Machine	200 MHz	800 MHz
Voltage	V	-	6.70 MV	1.27 MV
Relative RF phase	ϕ_{rf}	-	-	π
Harmonic number	h	-	4620	18480
Synchronous momentum	p_s	440 GeV	-	-
Transition energy	γ_t	18.0	-	-

The beam profile was measured over 100 consecutive turns over 25 cycles. Assuming a binomial distribution, The bunch lengths τ_{FWHM}, binomial exponents μ and bunch-by-bunch intensities were found through analyzing every bunch for every turn and for every shot. These parameters were then averaged over for each bunch across each turn and shot.

3.5.2 Measurement Results

The acquired antenna voltages during SPS flat top in the no beam segment are found in Table 3.9. The corresponding power estimates in the no beam segment are found in Table 3.10 and plotted in Fig. 3.7. For all of the cavities, the power variation was found to be less than 2.9 % on a turn-by-turn and 6.6 % on a shot-by-shot basis along the entire turn. The power signal from acquisitions when the beam passes through the cavity is shown in Fig. 3.8. For the acquisition of the antenna voltage, the variation was found to be less than 0.5 % turn-by-turn and 0.7 % shot-by-shot for each of the cavities.

As for the measurement of the beam profiles and the bunch-by-bunch offset, it was found that the turn-by-turn variation of the bunch-by-bunch offset was less than 65.6 ps and the shot-by-shot variation was found to be less than 77.6 ps. The variation is likely due to dipole oscillations of the bunches, i.e. the FWHM position of the bunches moving back and fourth in their RF buckets. This might also indicate that the beam was not entirely stable during these acquisitions, although the acquisitions did not cover enough turns to make conclusions on beam stability.

The OTFB will regulate the acquired antenna voltage $V_{ant,acq}$. This acquisition itself can have a calibration error, in which case the actual antenna voltage $V_{ant,real}$ seen by the beam would be different. If the cavity is properly calibrated, the two voltages should coincide. Three different values of the generator power were found using three different methods. P_{acq} is from the parasitic acquisitions that were done of the SPS OTFB signals. P_{set}, $P_{ant,acq}$ and $P_{ant,real}$ were found through the use of Eq. (3.29) and Eq. (3.36) and applying V_{set}, $V_{ant,acq}$ and $V_{ant,meas}$, respectively.
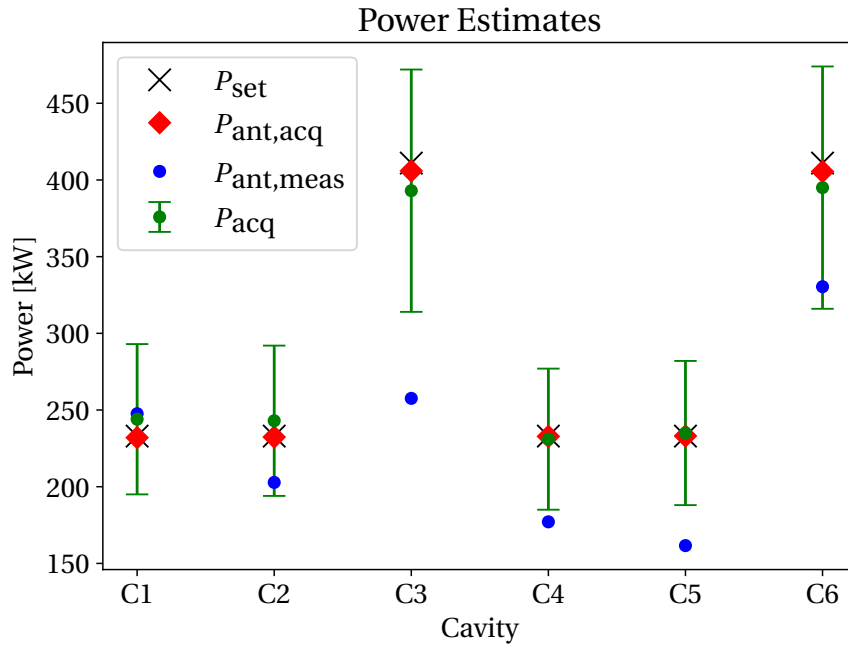
Figure 3.7: The data in Table 3.10 visualized. Note that the standard deviation of $P_{ant,acq}$ and $P_{ant,meas}$ were so small compared to that of P_{acq} that they are plotted as points.

Figure 3.8: The power signal from acquisitions of each cavity. The average is taken for each cavity over 23 turns and 3 acquisitions.

3.5.3 Measurement Error in Voltage and Power

The measurements were performed on the SPS in the first (commissioning) year after LS2. The RF power and voltage in the cavities were not yet perfectly calibrated. This is evident

Table 3.9: Voltage at flattop for each TWC extrapolated from measurement of voltage offsets done at flat bottom and from parasitic measurements done at flattop.

Cavity	V_{set}	$V_{ant,acq}$	Avg $V_{ant,real}$	Relative error
C1	0.91 MV	(907.1 ± 0.4) kV	0.937 MV	$(+3.0 \pm 1.0)$ %
C2	0.91 MV	(907.9 ± 0.5) kV	0.848 MV	(-6.8 ± 0.3) %
C3	1.53 MV	(1521.0 ± 0.5) kV	1.212 MV	(-20.8 ± 0.4) %
C4	0.91 MV	(908.8 ± 0.3) kV	0.793 MV	(-12.9 ± 0.2) %
C5	0.91 MV	(909.4 ± 0.3) kV	0.757 MV	(-16.8 ± 0.7) %
C6	1.53 MV	(1520.4 ± 0.5) kV	1.372 MV	(-10.3 ± 0.2) %

Table 3.10: Different estimates of the generator power consumption for each 200 MHz TWC. P_{set}, $P_{ant,real}$ and $P_{ant,acq}$ were found through the use of Eq. (3.29) and Eq. (3.36) and V_{set}, $V_{ant,meas}$ and $V_{ant,acq}$ from Table 3.9, respectively. P_{meas} are directly from parasitic measurements.

Cavity	P_{set}	$P_{ant,acq}$	$P_{ant,meas}$	P_{acq}
C1	233 kW	(232.0 ± 0.2) kW	(247.6 ± 4.8) kW	(244 ± 49) kW
C2	233 kW	(232.4 ± 0.2) kW	(202.8 ± 1.3) kW	(243 ± 49) kW
C3	411 kW	(405.9 ± 0.3) kW	(257.6 ± 2.6) kW	(393 ± 79) kW
C4	233 kW	(232.8 ± 0.1) kW	(177.1 ± 0.8) kW	(231 ± 46) kW
C5	233 kW	(233.1 ± 0.2) kW	(161.6 ± 2.7) kW	(235 ± 47) kW
C6	411 kW	(405.5 ± 0.3) kW	(330.4 ± 1.5) kW	(395 ± 79) kW

when analyzing the measured antenna voltage and power across cavities of the same type. Later in 2021, during a dedicated voltage calibration measurement with beam at flat bottom, the physical voltage seen by the beam during operation was measured to be 11 % lower on average than the acquired antenna voltage. Note that these measurements were only done on flat bottom and the calibration can differ at flat top.

The power measurement from acquisitions, P_{acq}, is obtained from directional couplers along the transmission line between the amplifiers on the surface and the cavities in the tunnel. Because the load is not perfectly matched between the two, the wave is partially reflected back from the cavities. The directional coupler measures the sum of the forward wave (sent down into the tunnel) and the reflected wave (even multiple reflections). The two waves can either interfere constructively or destructively at the point of measurement and a relative error of ± 20 % is assumed for the power measurements due to this. We assumed that all other sources where negligible for this measurement in comparison with this error. In addition, a relative error of 10 % was used for the voltages that were measured. Lastly, there was an uncertainty in

what the overall gain of the OTFB was, which is defined as

$$G_{\text{tot}} = G_{\text{llrf}} G_{\text{tx}}. \tag{3.40}$$

After LS2 upgrade, the gain reach of the LLRF system is 20 linear, or 26 dB, but during the measurements, it could have been in the range of 20-16 linear [35]. This gain is important since it determines by how much the OTFB reduces the 200 MHz effective impedance.

3.5.4   Measurement Data for Comparison with Simulations

A baseline case was chosen from the measurements that were performed. The two main measured signals that will be compared with simulations is the power and the bunch-by-bunch offset. The power measurement that will be compared with simulation is found in Fig. 3.9. This is the average across all cavities of the same type. Moreover, the shaded area represents the uncertainty in the measurement. As mentioned in Sec. 3.5.3, due to the reflected signals in the transmission line, the estimated uncertainty on the power signal is ±20 %, neglecting all other uncertainties. The bunch-by-bunch offset that will be compared with simulations is found in Fig. 3.10. This was found from the beam profiles, by averaging over all the bunch-by-bunch offsets over all batch, turns and shots. The shaded area in the plot was found by finding the standard deviation over the same set of measurements.
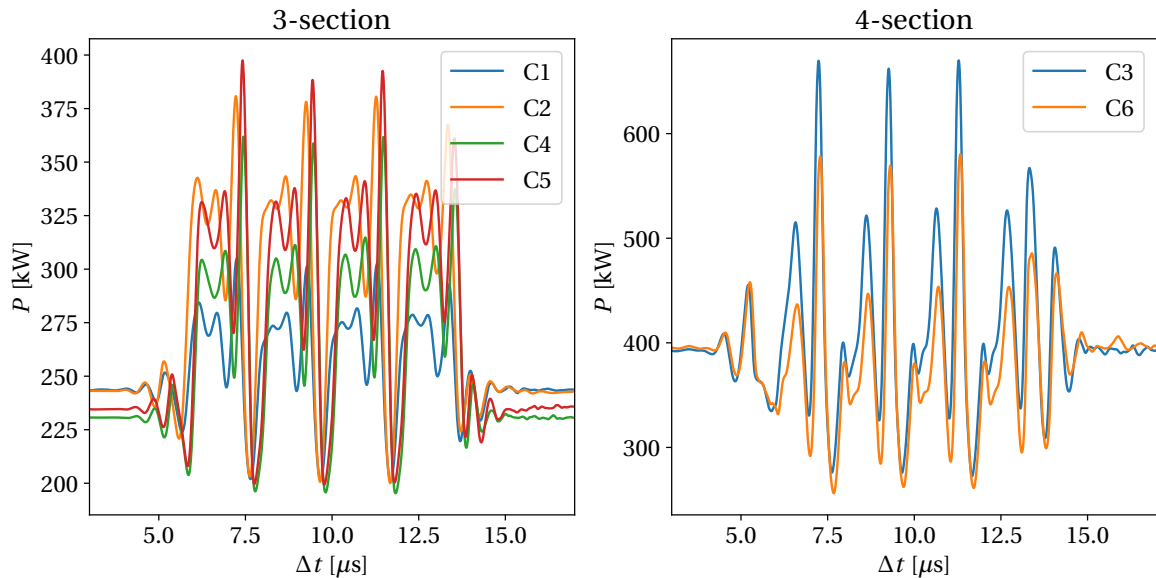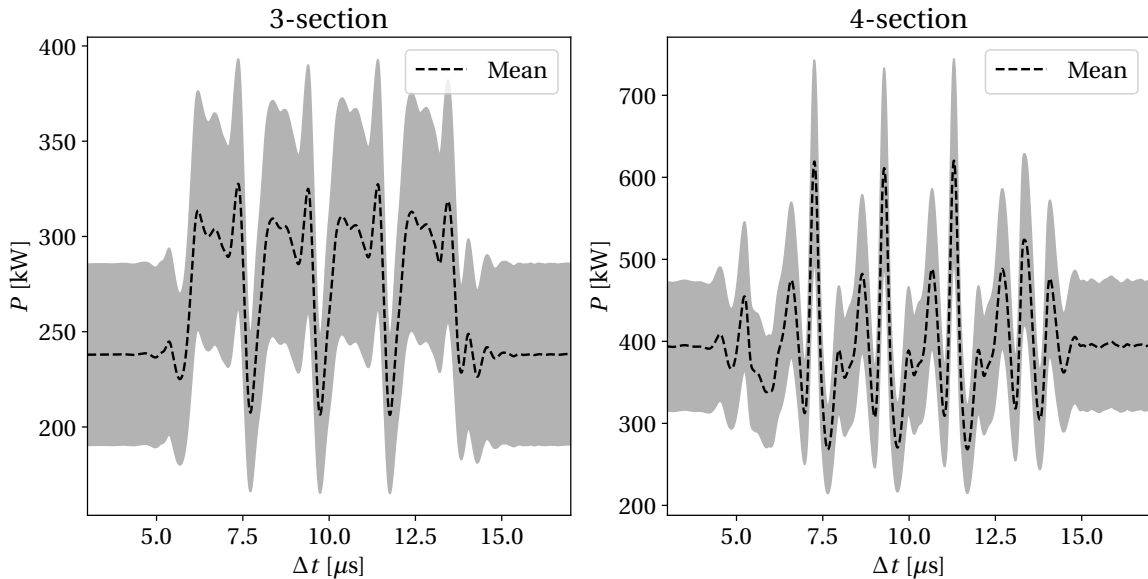

Figure 3.9: The power signal average from acquisitions of each cavity. The average is taken for each cavity over 23 turns and 3 acquisitions.

3.6   SPS Benchmark Against Measurements - Simulation Results

As a final benchmark of the OTFB model, we carried out simulations to reproduce the measurements done at SPS flat top. This section will go through the steps that were made to ensure a
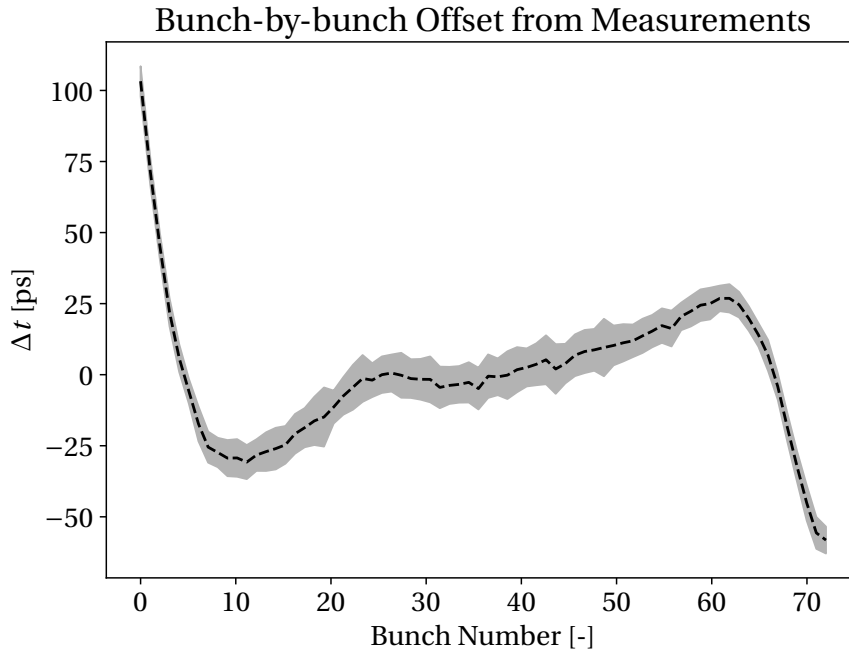
Figure 3.10: The turn-by-turn evolution of bunch 40 in batch 1 for a simulation with full impedance model without the 200 MHz TWCs and the OTFB model with a gain of 20.

simulation with reasonable conditions and compares the obtained results with measurements.

3.6.1 The Simulation of the SPS flattop

The parameters for the simulation can be found in Table 3.11 and the settings for the RF and OTFB system are found in Table 3.12. These setting will be the baseline case for the simulations. As discussed in Sec. 3.5.3, however, there are uncertainties in what the conditions were during the time of the measurements. Most importantly in the overall OTFB gain and the 200 MHz RF voltage. In the next subsection we will describe how the gains were found and how sensitive the simulations are to the gain value. Lastly, there has also been different measurements of the resonant frequencies of the 200 MHz TWCs. The designed resonant frequency of the cavities was originally 200.222 MHz [14]. When they were taken out of the tunnel and measured in 2018, it was found that the TWCs had a resonant frequency of 200.1 MHz [36]. The latest measurement of the TWCs [33] resulted in resonant frequencies of 200.038 MHz for the 3-section cavities and 199.995 MHz for the 4-section cavities. The most recent case, which also deviates the most for the original design, will be the baseline for the simulations. However, all three frequency configurations will be used in simulations, see Table 3.13, since the measurements have a high uncertainty [36] and because the 2018 value is assumed for the real LLRF system.

In addition to using the same parameters in simulations as in the real machine, a realistic impedance model has to be included, too. Since the impedance of the main harmonic of the 200 MHz TWCs is incorporated through the OTFB, all other impedances were modelled

Table 3.11: Parameters used to simulate the cycle over which the measurements were performed.

Parameter	Symbol	Unit	Value	200 MHz	800 MHz
Circumference	C	m	6911.560	-	-
Synchronous momentum	p_s	GeV / c^2	440	-	-
Transition gamma	γ_t	-	18.0	-	-
RF voltage	V	MV	-	6.70	1.27
Harmonic number	h	-	-	4620	18480
800 MHz RF phase (w.r.t. to the BLonD reference)	ϕ_{rf}	-	-	-	π

Table 3.12: Parameters for the SPS OTFB used to simulate the cycle over which the measurements were performed.

Parameter	Symbol	Unit	3-section	4-section
Transmitter gain	G_{tx}	-	0.91	0.91
LLRF gain	G_{llrf}	-	20	20
Voltage Partitioning	V_{part}	-	0.544	0.456
Number of Cavities	n_{cavities}	-	4	2
Comb filter coefficient	α_{comb}	-	31/32	31/32
Resonant frequency	f_r	MHz	200.038	199.995

through the frequency domain DFT in BLonD. A frequency domain plot of SPS impedance can be found in Fig. 3.11. The model is built of different elements, which described as resonators. The plot on the left depicts the different peaks of the narrow-band impedances and the plot on the right shows in more detail the broad-band impedance background. It is also worth mentioning that the higher-order modes of the 200 MHz TWC are reduced by a factor 3 because of the impedance reduction campaign performed during LS2. In addition, the impedance of the 800 MHz TWCs are reduced by a factor 20 to mimic the effect of their cavity controller system (which is not tracked in the BLonD simulations).

The last major piece of the simulation is modeling a realistic beam distribution. Using the average measured bunch length τ_b, bunch intensity and binomial exponent μ for each individual bunch taken from measurements, we generated a beam consisting of 4 batches each with 72 bunches. The beam was generated while also taking into account the impedance of the SPS. This was done by iteratively generating bunches and fitting them to the perturbed potential well created by the RF cavities and the beam-induced voltage due to the impedance [37].

The generated beam was then analyzed in the same way as the measured profiles. This was done to verify that the beam generated with impedance matching (GwI beam) was reasonable in comparison with the measured profiles. The measured and generated intensities along with

Table 3.13: The three resonant frequency scenarios that were used in simulations.

Scenario	Unit	3-section	4-section
F1 (2021 measurement)	MHz	200.038	199.995
F2 (2018 measurement)	MHz	200.1	200.1
F3 (1970's design)	MHz	200.222	200.222

the bunch lengths across the four batches can be found in Fig. 3.12; this beam was also used in [1].
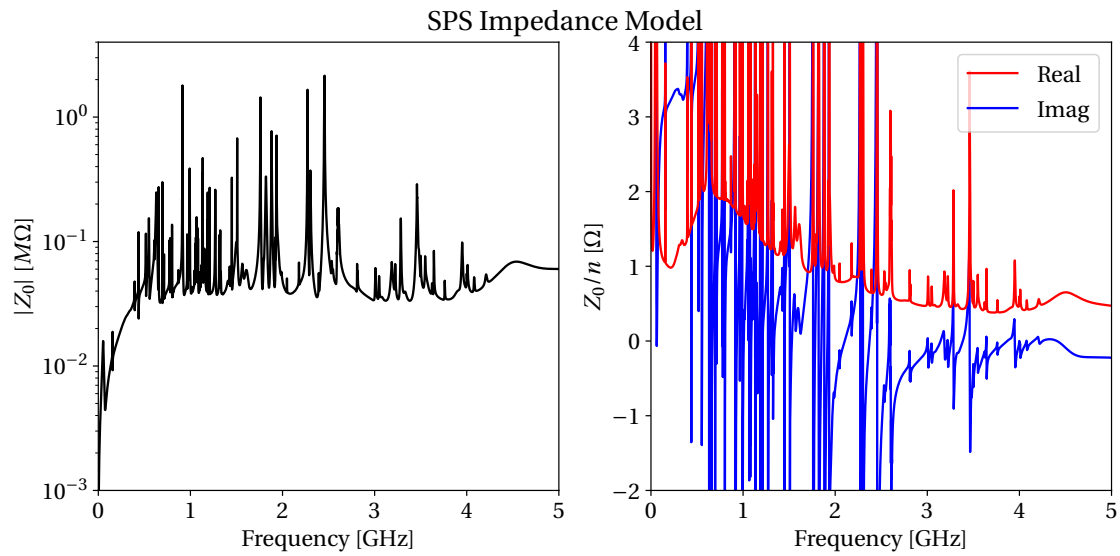
Figure 3.11: The model of the impedance in the SPS machine that was used in the simulations. This model does not contain the 200 MHz TWC impedance, since this impedance enter through the OTFB model. In addition, the 800 MHz TWC impedance is reduced by a factor 20 linear to model the effect their OTFBs. The right plot is zoomed in to show the broadband background of the SPS impedance.
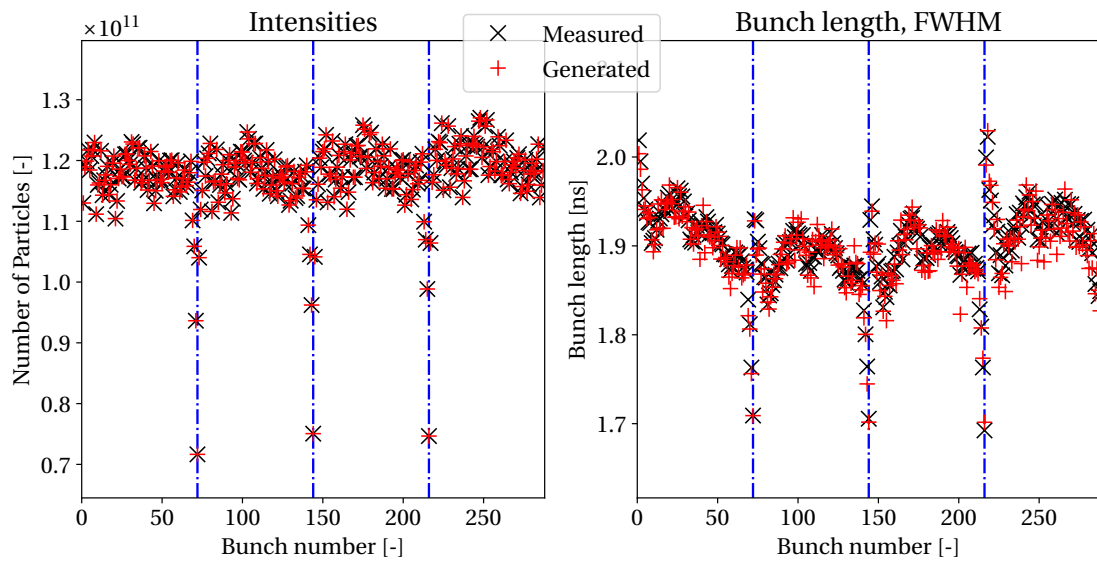
Figure 3.12: Bunch-by-bunch intensities and bunch lengths for the measured result and the generated beam with impedances.

3.6.2 OTFB Gain Sensitivity in Simulations

In operation the gain in the SPS LLRF system is optimized by leaving a 10 dB margin in the positive real zero-crossing of the open loop system response and a negative zero crossing equal to the total desired gain of the feedback. This can be read off directly from a Nyquist-plot like the one in Fig. 3.13. For this figure in particular we simulated the open loop response of the 3-section cavities with the OTFB settings as given in Table 3.12. To perform the measurement, the BBNA method was applied, injecting white noise into the OTFB system as shown in Fig. 3.14 and measuring after the cavity response towards the generator. The set point voltage was at 1 MV and the amplitude of the white noise was at 50 % of this. The obtained open-loop transfer function in a Bode plot can be found in Fig. 3.15 with a plot zoomed around the base-band frequency in Fig. 3.16 showing the comb-filter structure at f_{frev} sidebands. The lines in the NyQuist plot correspond to multiples of the revolution frequency and each of the notches in the zoomed Bode plot. As mentioned earlier, there was an uncertainty in what overall OTFB gain was used for the measured cycle and the exact values of the transmitter and LLRF gains were not obtained. Even though the OTFB model gains found in Table 3.12 were optimized in the same way as in operation, there was still an ambiguity in what the values were.
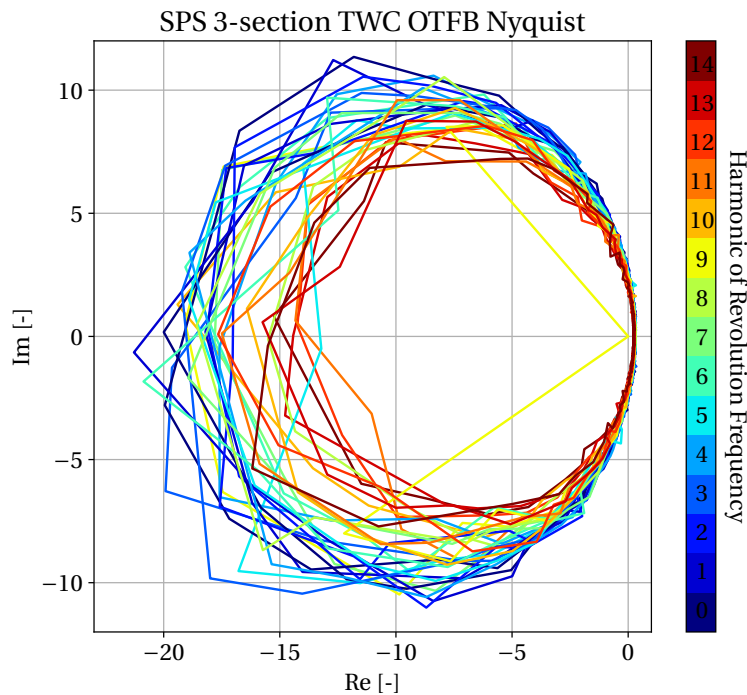
Figure 3.13: NyQuist plot of the 3-section TWC OTFB open loop response. The resonant frequency of the TWC was at 200.038 MHz.

A parameter scan around the optimized values were performed to check how sensitive the behavior of the beam and the OTFB were to the gain value. The scan was performed for three different configurations of the resonant frequency of the TWCs, see Table 3.13. The

SPS One Turn Feedback
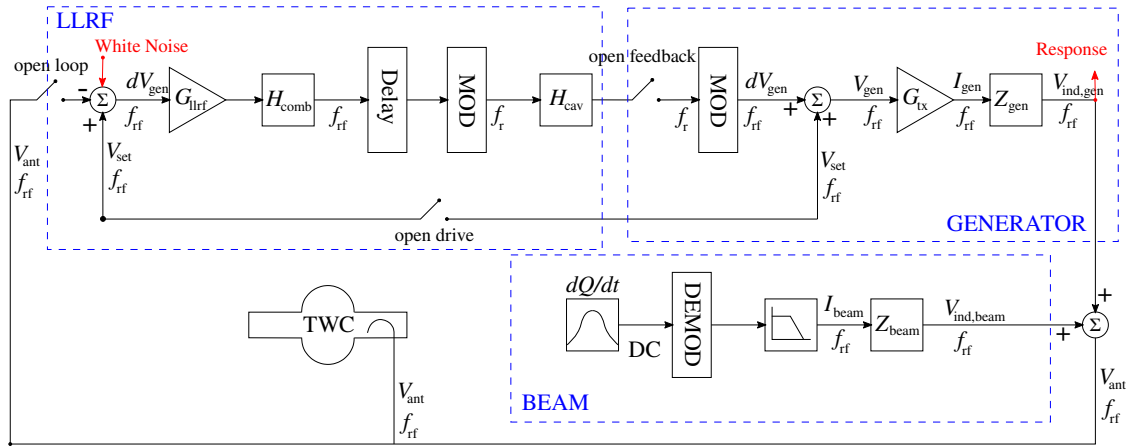
Figure 3.14: Schematic of how the broadband spectrum analysis was done on the SPS OTFB model. The analysis was performed with the loop open, with a set point of 1 MV and a white noise amplitude at 50 % of the set point.

transmitter gain was varied from −10 % to +10 % of the value given in Table 3.12 in 10 steps for each of the three resonant frequency configurations. Figure 3.17 depicts how the baseline configurations compare to the measured case. The two other resonant frequency scenarios are found in App. D.

As can be seen from Fig. 3.17, the bunch-by-bunch offset and the power of both the 3- and 4-section did not vary significantly within the parameter space that was scanned. This means that the result of the simulation should not depend much on how accurately the gain was calibrated in comparison what was in operation. It should however be emphasized that this statement is only valid around each of the gain values that could have been used in operation. Meaning that for each gain value, e.g. 10, 16 or 20 linear, we expect the signals depicted in Fig. 3.17 to vary more. This was only a check of how precisely the gain would have to be tuned around each value, which in this case was around a gain of 20 linear.

3.6.3 RF Voltage Parameter Scans

Parameter scans of the RF voltage of the 200 MHz RF system were performed due to the uncertainty in measurements, as discussed in Sec. 3.5.3.

The scan was performed for the three different scenarios in Table 3.13. Each scan was done from -20 % to +20 % of the nominal voltage at flattop of the measured cycle, 6.7 MV, with 20 increments. All the other settings and parameters were equal to the base case. The two representative cases in terms of 200 MHz RF voltage were taken to be 5.89 MV and 6.76 MV. In the top plot of Fig. 3.18 one can find the bunch-by-bunch offset from the two representative cases for the three resonant frequency scenarios. The two bottom plots of Fig. 3.18 shows the generator power consumption from the same set of simulations.
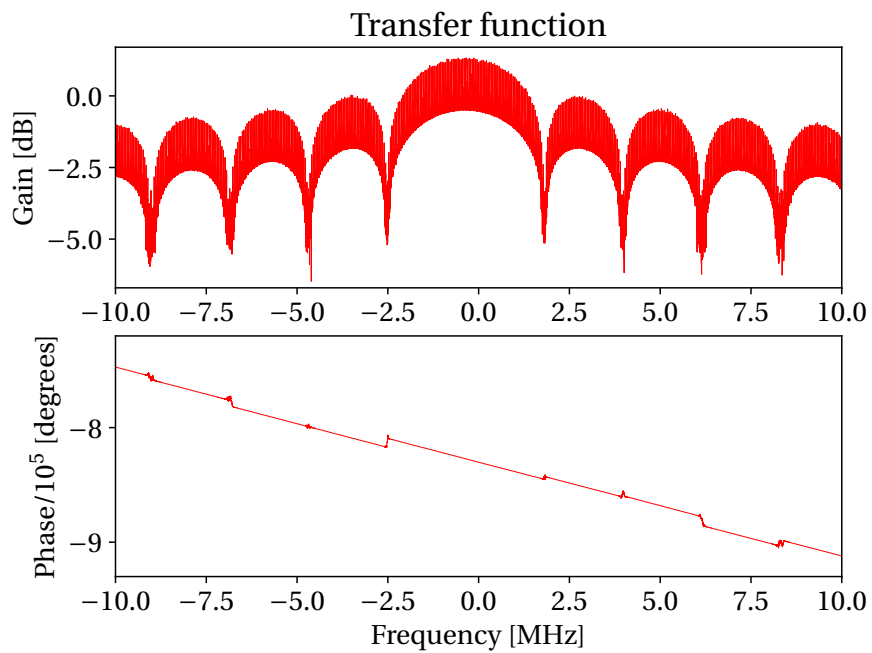
Figure 3.15: Simulated measurement of the open loop response of one SPS TWC 3-section with resonant frequency at 200.038 MHz.
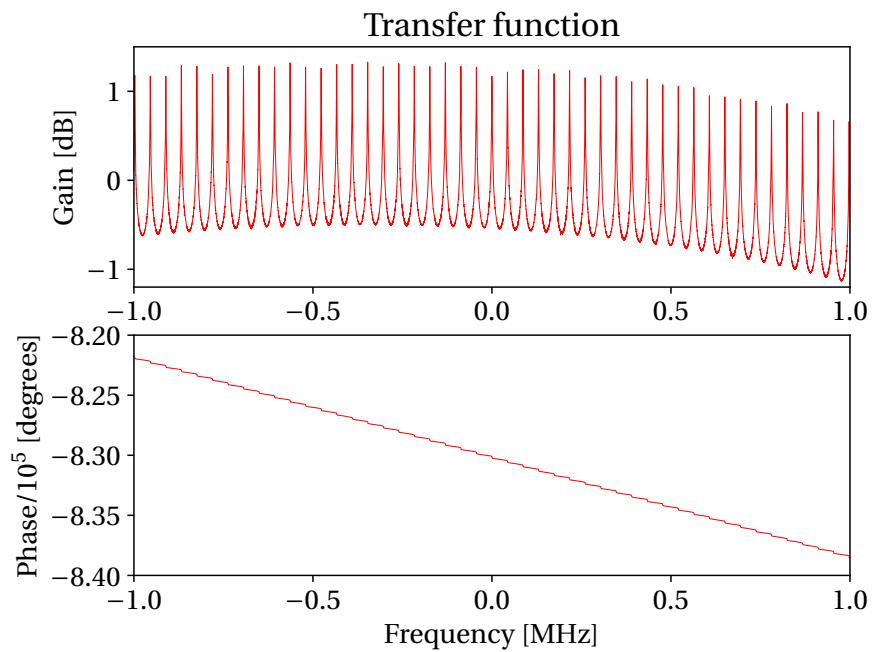
Figure 3.16: A zoom in on the simulated measurement of the open loop response of one SPS TWC 3-section with resonant frequency at 200.038 MHz.
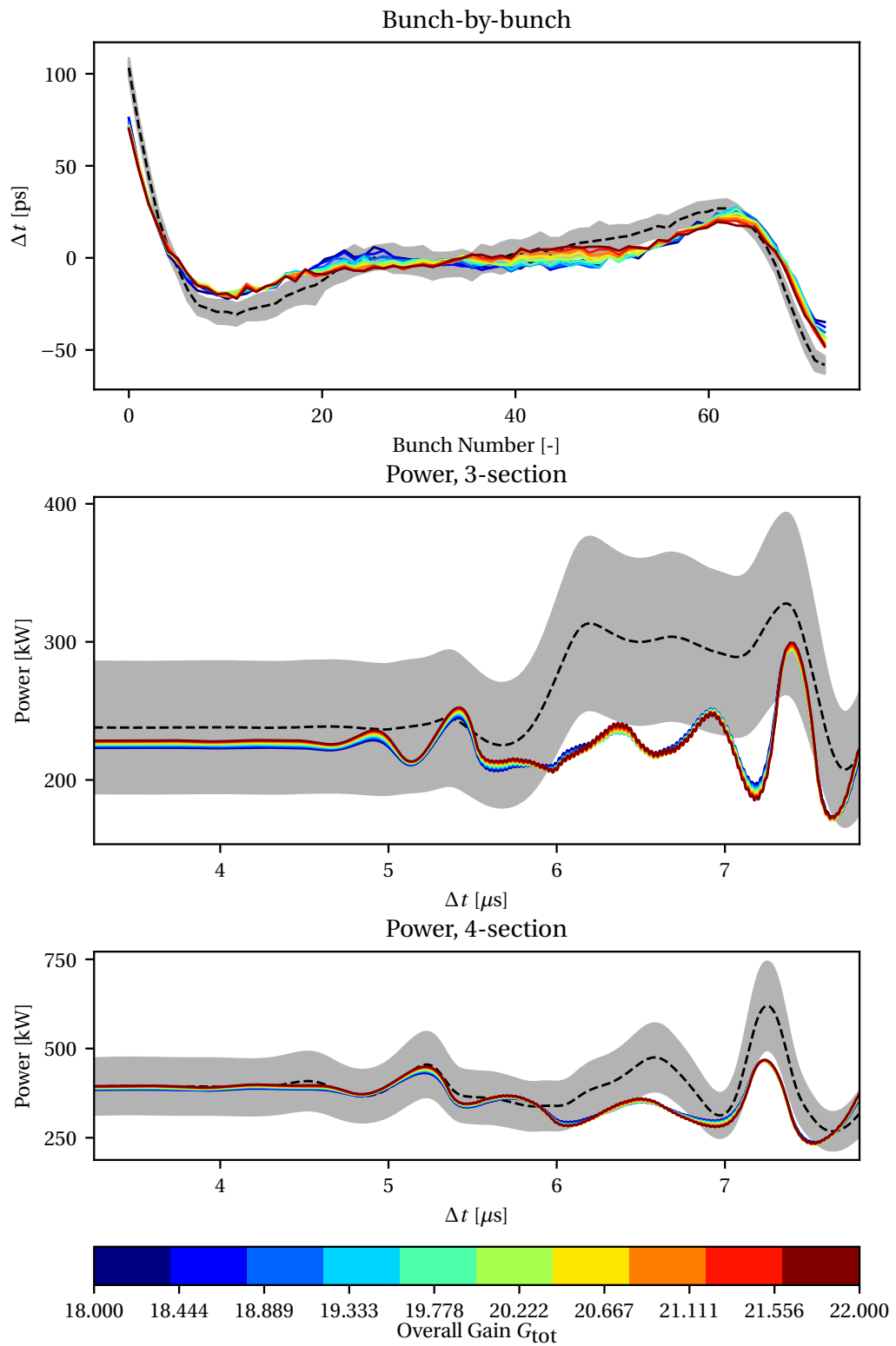
Figure 3.17: Scan of the OTFB gain with all other simulation parameters equal to the baseline case except the transmitter gain G_{tx}.
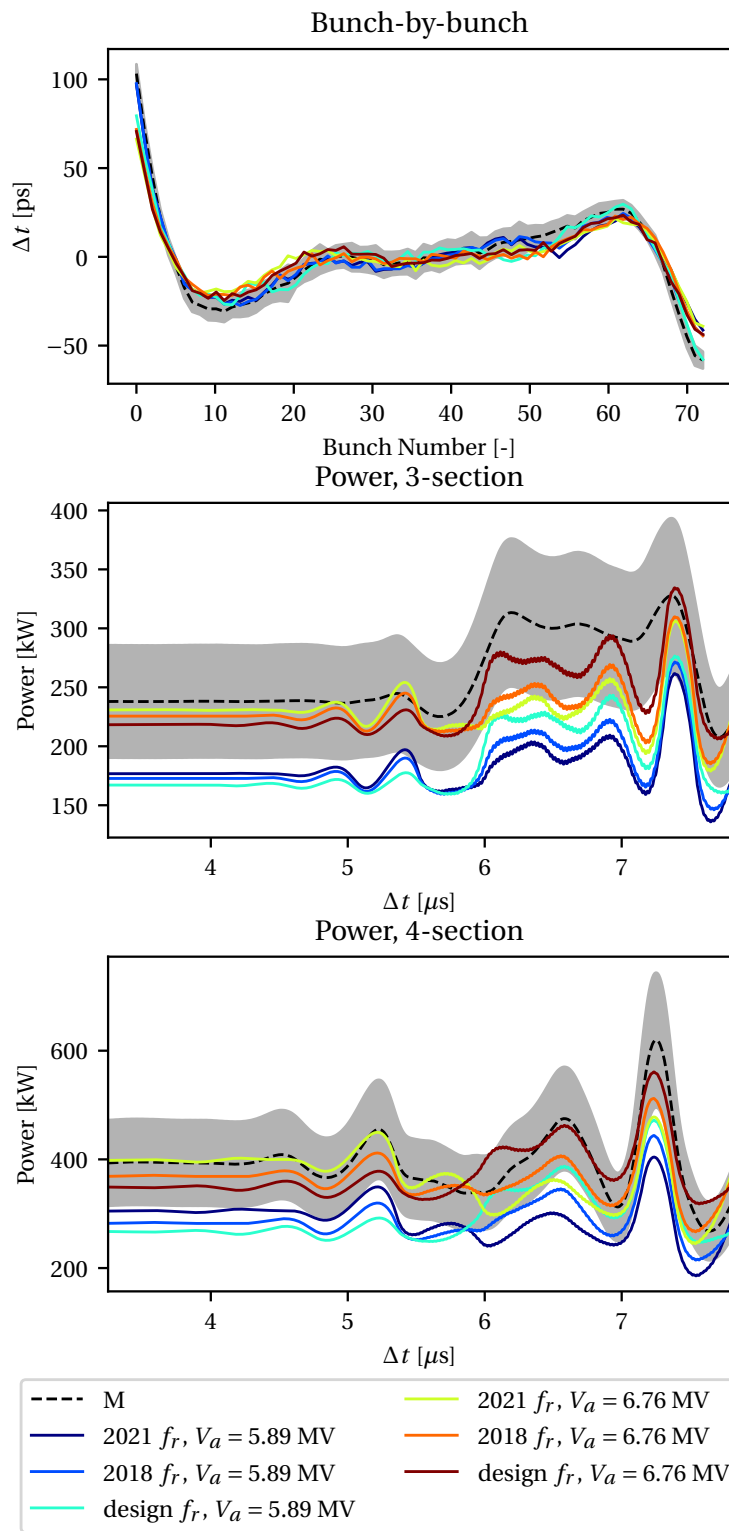
Figure 3.18: Comparison of power and bunch-by-bunch offset between measurements and simulations with various combinations of resonant frequency and 200 MHz RF voltage. The cable transfer function was applied to the beam profile from simulation before the bunch-by-bunch offset was calculated.

The cable and connectors that transmit the measurement of the beam profile have a certain response expressed through a transfer function. In order to make the comparison between measurements and simulations more realistic, the cable transfer function was applied to the simulated profiles (as measurement profiles are uncorrected). As is shown in Fig. 3.19, this had the effect of smoothing the offset across the batch and move the first and last few bunches away from the ones in the center. It should however be noted that the profile without the transfer function in principle is closer to the actual physical profile. Due to zeros in the cable transfer function however, it is not possible to easily de-convolve the measured profiles instead.

Figure 3.19: Bunch-by-bunch offset of the first batch in a simulation with $V_{ant} = 6.76$ MV and TWCs with their original design resonant frequencies. The full red trace is with the cable transfer function (CTF) and the dashed red trace is without.

From the bunch-by-bunch offsets depicted in the top plot in Fig. 3.18, one can see that there is little variation across the simulations. One can also see that the peak-to-peak offset in simulations is lower than in measurements. There can be a number of reasons for this. For instance, this could be due to a OTFB gain slightly lower than 20 linear in measurements. On the other hand, the offset at the center of the batch matches measurements within the standard deviation and a lower gain could change this. Another reason could be the filters in the OTFB model and in particular the cavity filter, which is not just a moving average in reality. A more accurate model of the filters could change the offset at the ends of the batch. The simplified filters could also be the cause of the difference between simulated and measured transient shapes in the generator power.

The two bottom plots in Fig. 3.18 shows that the higher the RF voltage supplied by the cavities, the higher the power consumption, which is what is expected. Additionally, it shows

that the further away the resonant frequency is from the RF frequency, the more power is consumed by the generator in the no beam segment. However, in the beam segment the opposite seems to be the case, i.e. the closer f_r of the TWCs are to RF frequency the higher the consumption. In addition, the shape of the transients seems to change slightly depending on the resonant frequency. In terms of power, it seems like the simulation with the TWC resonant frequencies at 200.222 MHz and a 200 MHz RF voltage closer to the nominal 6.7 MV describes the measurements overall the best. It should however be emphasized again that power measurements have a large uncertainty and we do not expect a perfect agreement with simulated power.

In terms of power it is also interesting to compare the difference between the no beam segment and the beam-loaded part of the power. The differences for the simulations discussed are found in Table 3.14. From the simulations given in this table, we see that the simulation with the resonant frequencies from the 2018 measurement and antenna voltage of 6.76 MV is the closest for the 3-section cavities. This simulation has only a 6.5 % difference w.r.t. measurements. For the 4-section cavities, however, it seems that the simulation with the original design resonant frequencies and antenna voltage at 6.76 MV is the closest with a difference of 4.9 %.

Table 3.14: The difference between the power no beam segment and the peak beam-loaded power from simulations and measurements.

Configuration	3-section		4-section	
	Absolute	Relative	Absolute	Relative
Measurement	89.80 kW	37.71 %	226.70 kW	57.51 %
Design f_r, V_{ant} = 5.89 MV	110.41 kW	66.06 %	208.44 kW	78.06 %
2018 f_r, V_{ant} = 5.89 MV	99.02 kW	57.35 %	163.44 kW	57.77 %
2021 f_r, V_{ant} = 5.89 MV	85.06 kW	48.13 %	99.49 kW	32.64 %
Design f_r, V_{ant} = 6.76 MV	116.94 kW	53.57 %	216.13 kW	61.97 %
2018 f_r, V_{ant} = 6.76 MV	84.31 kW	37.39 %	148.74 kW	40.25 %
2021 f_r, V_{ant} = 6.76 MV	79.55 kW	34.47 %	79.91 kW	20.07 %

In conclusion from these simulations, one can see that the model manages to reproduce the measured bunch-by-bunch offset within the measurement uncertainty. For the future studies of LHC injection, this is the most important result. Indeed, reproducing the bunch-by-bunch offset is what the SPS OTFB will mainly be used for in the context of the LHC injection studies. Furthermore, the power is not very far off from what was measured, as seen in Fig. 3.18 and Table 3.14. On the other hand, as discussed, there are many uncertainties in the measurement of the power, RF voltage, and cavity resonant frequency. For better agreement between measurements and simulations, both more precise measurements and probably more realistic filters in the simulation model would be required.

3.7   Beam Instabilities in the Simulations

Coupled-bunch instabilities were encountered in the simulations of SPS flat top. In fact, the results found in Fig. 3.17 and Fig. 3.18 are taken from a stable part of the simulations, i.e. right before the onset of instability. In general, the instabilities could either be due to numerical noise that drive some unphysical instability, or due to an actual physical effect. Figure 3.20 depicts bunch-by-bunch offset from the last 200 turns from the baseline simulation scenario and illustrates why this instability is problematic. As can be seen from this figure, as the bunches oscillate, the bunch-by-bunch offset changes over time. We will now go through the different behaviors of the instability that was studied and what parameters that had the most substantial influence on it.
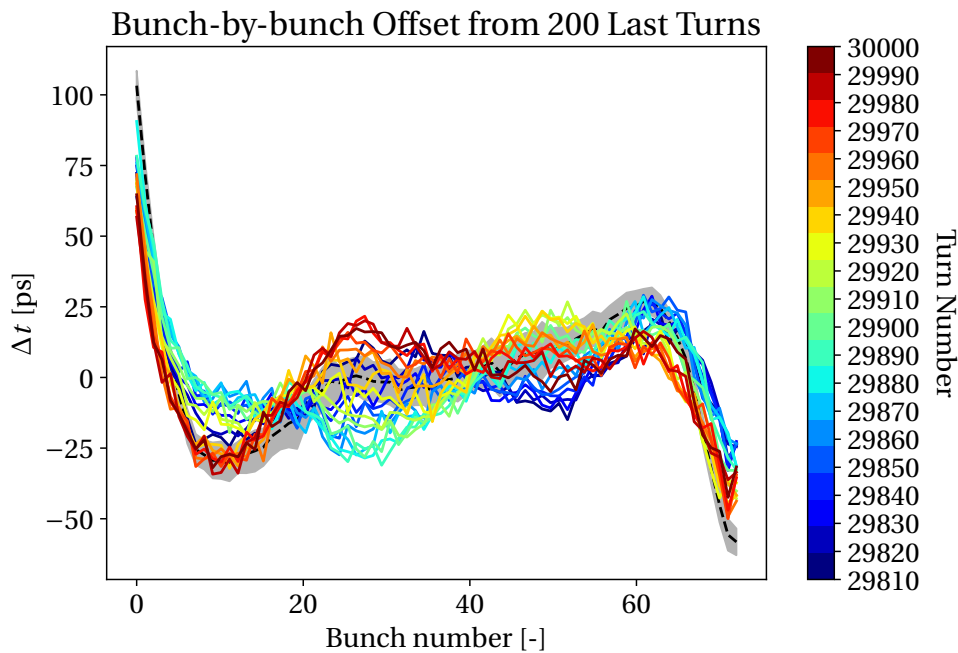
Figure 3.20: Bunch-by-bunch offset form the 200 last turns of the baseline simulation.

To quantify this instability, the behavior of the bunch positions, Δt_b, from a FWHM fit was analyzed over the span of the 30,000 turns that was simulated. The amplitude of the dipole oscillations was found by fitting a line to the bunch position of each bunch as a function of turns. Furthermore, the turn-by-turn displacement from this mean was found for each bunch, thus giving an estimate of the amplitude of the oscillatory behavior. Figure 3.21 depicts the bunch position as a function of turns for a given bunch in simulations. As can be seen from the figure, the estimate of the amplitude seems to match the local maxima and minima of the dipole oscillation, which is what we want to study. To study the growth of dipole oscillations in each of the batches, the maximum dipole oscillation (MDO) was computed. This was done by taking the amplitude of the dipole oscillation for each of the 72 bunches in the batch and finding the maximum value of it across the batch for each turn.

The procedure described above was then used to analyze the base case simulation, i.e. the
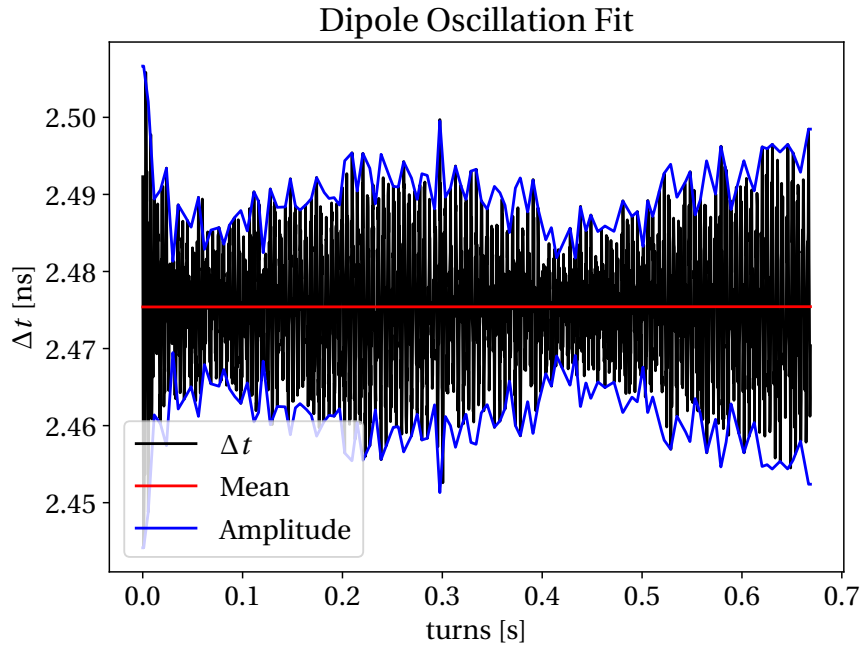
Figure 3.21: The turn-by-turn evolution of bunch 40 in batch 1 for a simulation with full impedance model without the 200 MHz TWCs and the OTFB model with a gain of 20.

simulation using the parameters in Table 3.11 and Table 3.12. The MDO estimated for each of the four batches in simulations can be found in Fig. 3.22. As seen from the plot, the growth of instability has a certain threshold from which it start. Additionally, the growth in dipole oscillations is largest in the first batch. A simulation with the exact same parameters as the baseline case was run with twice the amount of macro-particles. The MDO plot of each of the batches from this simulation is found in Fig. 3.23. If the number of macro-particles are too low then this could lead to numerical noise in the bunch profile and can cause an unphysical instability in the simulations. However, it was found that the simulation behaved in the same way with twice the number of macro-particles and that the behavior of the instability was almost exactly the same. Thus, it seems like behavior of the physics have already converged with respect to the number of macro-particles in the base case. This result would then suggest that the instability was not due to numerical noise and at least not due to a lack of macro-particles.

The beam that was used in simulation was generated without the OTFB. Since the simulations started at flat top, it is as if the OTFB starts acting at this stage of the cycle. To exclude the possibility that the instability came from the initial mismatch between the beam and the RF buckets, we also studied simulations with adiabatic intensity ramps. This was done by increasing the amount of particles each macro-particle was worth over the course of many turns. In this case the ramp was done over 10 000 turns. The increase of dipole oscillations was still observed however, excluding the possibility that the instability was due to initial abrupt effects. In the real machine the beam is injected at SPS flat bottom and accelerated to flat

Figure 3.22: Maximum dipole oscillation for each of the four batches in a simulation of the baseline case.

top. Although the simulations with intensity ramp excluded the possibility of abrupt effects driving instability in simulations, it could be that the simulated beam at flattop would behave differently if part of the ramp was included in the simulation.

As another check, we ran simulations with the same conditions as the baseline case, but without the dynamic model of the OTFB. This means that instead of using the implementation of the SPS OTFB model shown in Fig. 3.2, the effect of the OTFB was only included as a -26 dB (factor 20 linear) attenuation of the 200 MHz TWC impedance model. As Fig. **??** shows, the beam is actually stable for this case. On the other hand, without the so-called dynamic model of the OTFB, the bunch-by-bunch offset does not match what was found in beam profile measurements. The reason why the simulation with the dynamical OTFB is unstable and the one without is not, can come from a number things. First of all, the effective impedance of the TWCs that the beams sees with the OTFB acting is not a simple scaling of the impedance. The factor 20 reduction of the effective impedance is only at narrow band notches at multiples of ω_{rev} due to the comb filter. The bandwidth of the notches are given as

$$\Delta f_{BW} = (1 - \alpha_{comb}) \frac{f_{rev}}{2\pi} \qquad (3.41)$$

and for $\alpha_{comb} = 31/32$ the notches have a bandwidth of around 215 Hz. On the other hand, the bunches have a synchrotron frequency of around 300 Hz. This means that the beam might sample part of the effective impedance that is not damped by the OTFB, which can drive instability. Secondly, for the parameter space in simulations that was studied thus far
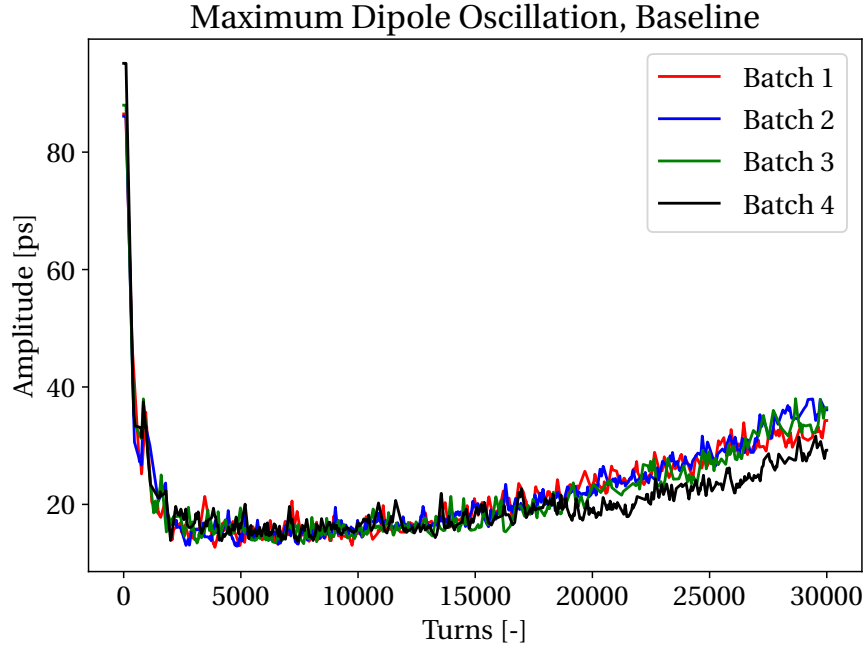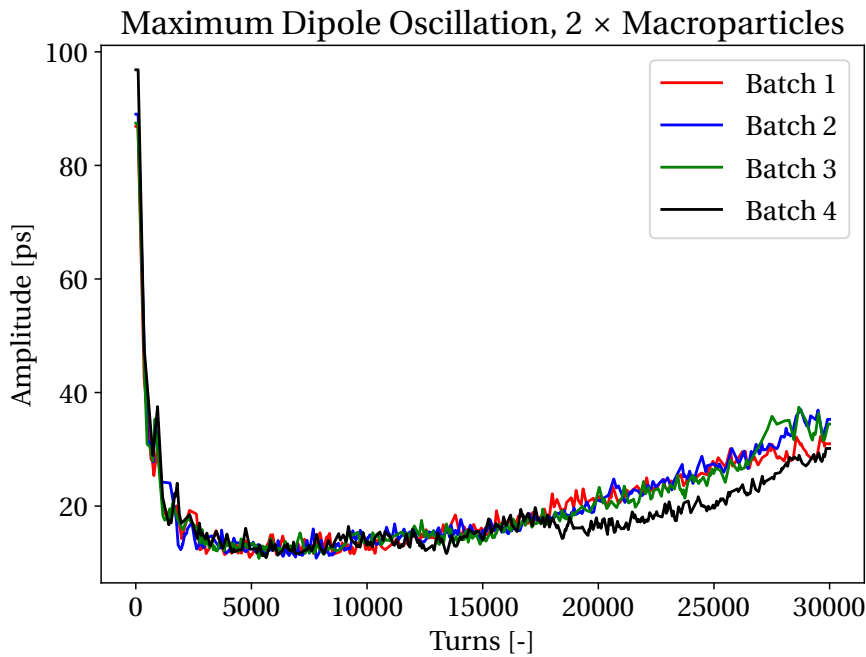
Figure 3.23: Maximum dipole oscillation for each of the four batches in a simulation of the baseline case, but simulated with twice as many macroparticles.

have seen the instability grow over the course of tens of thousands of turns. If the simulation without OTFB was longer than perhaps one would see the same instability. The reason why this is seen sooner in the simulations with the OTFB, might be because it introduces noise into the beam that drives the instability. Although these explanations should be considered, it cannot be excluded that the BLonD SPS OTFB model is the cause of the instability and that there is something wrong with the model.

A new beam was generated where the bunch length of every bunch in the beam was increased by 10 %. As shown in Fig 3.25, the longer bunch length helped stabilize the beam. It seems like there was still a growth in the dipole oscillations, but the onset of the increase in amplitude occurred later. Furthermore, the growth of the oscillations were slower than the baseline case. Comparing Fig. 3.25 with Fig. 3.24, we see that the increase in bunch length is not enough to achieve the same stability as the simulation without OTFB. In addition, the maximum dipole oscillation is higher than the simulation without OTFB also before the onset of instability. The fact that the instability diminishes with increasing bunch length is consistent with physical instabilities such as loss of Landau damping. Hence, this observation seems to point towards a physical effect rather than a numerical excitation.

As mentioned in Sec. 3.6.3, parameter scans of 200 MHz RF voltage were performed to study its effect on the instability. Fig. 3.26 shows scans in RF voltage done for the three different frequency settings in Table 3.13. The maximum dipole oscillation was calculated by finding the maximum value of the MDO between turn 5000 and the end of the simulation for each batch and each simulation. The maximum was found after turn 5000 to let the bunches stabilize
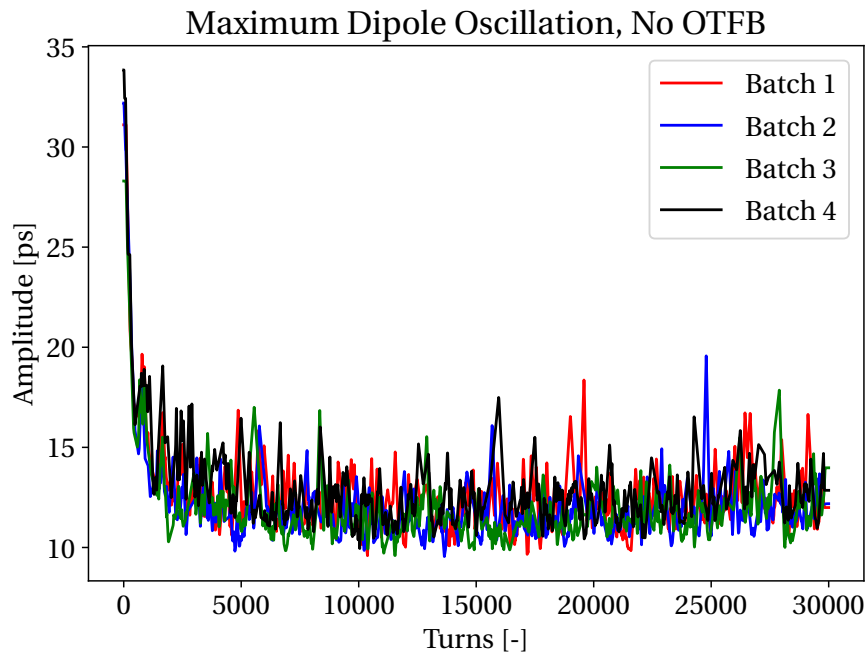
Figure 3.24: Maximum dipole oscillation for each of the four batches in a simulation with out the dynamic BLonD OTFB model. The TWC 3-section and 4-section impedances had the 2021 resonant frequencies and were attenuated by -26 dB to imitate the effect of the OTFB. 200 MHz RF voltage was 5.96 MV.

after the initial mismatching with the RF bucket which was perturbed by the OTFB. As can be seen from the figure, the dipole oscillations decrease in amplitude with increasing voltage and after approximately 7 MV the maximum amplitude stayed at around 14.1 ps for increasing voltages. The simulations with RF voltages over 7 MV was found to have the same sort of stability as the simulation without OTFB, meaning that there was no growth of instability over the 30 000 turns simulated. The dependency on voltage that was observed in Fig. 3.26, is also suggesting that the instability is some physical effect.
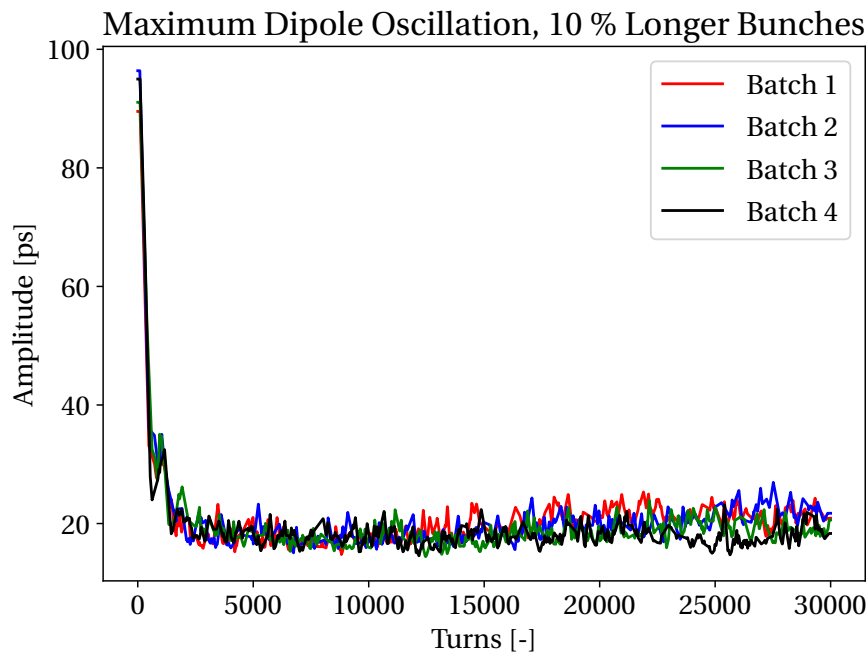
Figure 3.25: Maximum dipole oscillation for each of the four batches in a simulation using the baseline parameters, but with bunches that are 10 % longer.
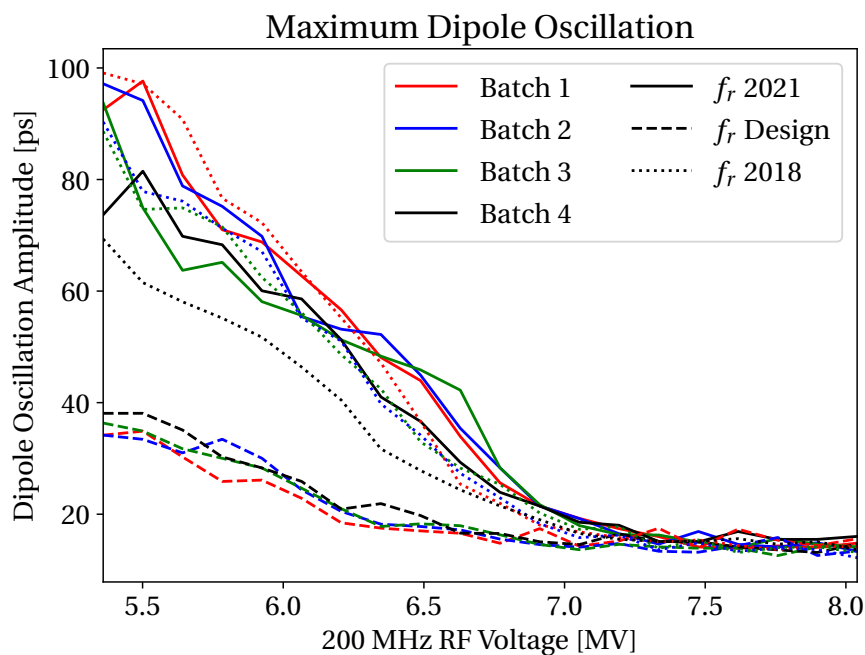
Figure 3.26: The maximum value of the MDO for each batch of each simulation. The full line traces are from simulations with the 2021 TWC resonant frequencies, the dashed traces are the original design frequency and the dotted traces are the 2018 measurements. All the simulation ran with the baseline case parameters otherwise.
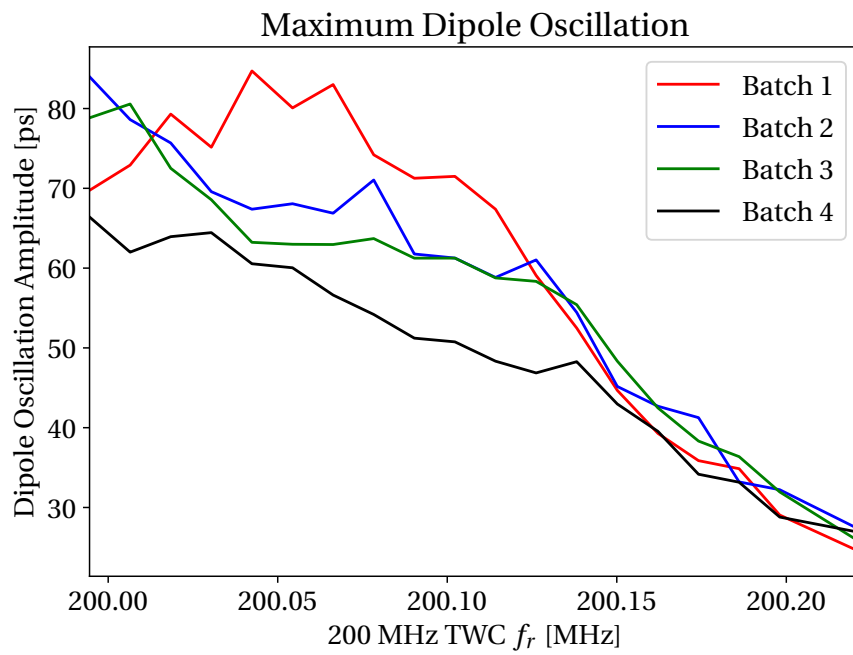
Figure 3.27: The maximum value of the MDO for each batch of each simulation. All the simulation ran with the OTFB model enabled with an overall gain of 20 linear, the 200 MHz RF voltage at 5.96 MV and both TWC types had the same resonant frequency.

The amplitude to which the dipole oscillations approached was found to be around 14.1 ps regardless of the resonant frequency. However, the amplitude of the dipole oscillation overall was seen to decrease with increasing resonant frequency. A parameter scan was performed for the TWC resonant frequency due to this observation. The maximum dipole oscillation as a function of resonant frequency can be found in Fig. 3.27 with the 200 MHz RF voltage at 5.96 MV instead of the baseline 6.7 MV value. This lower voltage was chosen because, as shown in Fig. 3.18, the lower voltages were more unstable. It should also be noted that the simulation with TWC resonant frequency at 200.210 MHz had to be discarded when making Fig. 3.27 because the MDO blew up for this simulation. As can be seen in Fig. 3.27, the instability seems to indeed diminish the closer the TWC resonant frequency is to the design frequency. This effect might also suggest that the instability was physical.

Instability was not directly observed in measurements. The maximum dipole oscillation amplitude after the 30 000 turns for the baseline simulation was approximately 40 ps. If this indeed was in the machine during the cycle, this would not have been deemed unstable during operation. Unfortunately, the stability of the beam was not checked and studied when the measurements where taken. In principle, we do therefore not know if the measurements were stable or not. It should also be emphasized that the measurements where done right after commissioning after Long Shutdown 2 and the SPS was therefore not yet properly calibrated. If the measurements were stable, then this might suggest a few things about the parameters in the simulations. Firstly, as shown in Fig. 3.26, a higher RF voltage leads to more stability within the parameter scan that has be considered. It might be the case that the RF voltage was higher than the value extrapolated from beam-based voltage calibration at flat bottom. Secondly, Fig. 3.27 suggests that the TWC resonant frequencies were higher than the baseline case. It is possible that there was a combination of the two, i.e. both a higher voltage than the 5.96 MV and a higher TWC resonant frequency than the 2021 measurement. We saw that the variation of these parameters had little effect on the bunch-by-bunch offset within the parameter space that was considered and given that the simulation was in a stable region. On the other hand, it seems like the generator power, especially in the beam segment, is more sensitive to the overall gain, the RF voltage and the TWC resonant frequencies.

We cannot exclude neither that the instability is physical nor unphysical. The instabilities dependency on RF voltage, TWC resonant frequency and bunch length is consistent with this being a physical instability. However, the absence of instability without the OTFB might indicate that this might be a numerical error in the OTFB model. A final check of this would be to do new measurements during a cycle with greater confidence in the parameters that were used, e.g. RF voltage, overall OTFB gain and so on. The simulation with OTFB was stable for certain settings and can therefore be used to generate a realistic bunch-by-bunch offset for LHC injection studies nonetheless.

4 LHC Cavity Control

This chapter describes the LHC cavity loop, how it was implemented in BLonD and some of the tests that have been performed to validate the model.

4.1 The LHC Superconducting Cavity

The LHC superconducting cavities can be modeled as an RLC-circuit [38]. Consider the circuit in Fig. 4.1 that shows the interaction of the cavity with the beam and the generator. In this representation, in addition to the RF cavity, the beam is presented as a current source and the generator as an incident wave current through a transmission line of impedance Z. In addition, there is also a reflected wave passing through the transmission line in the opposite direction.
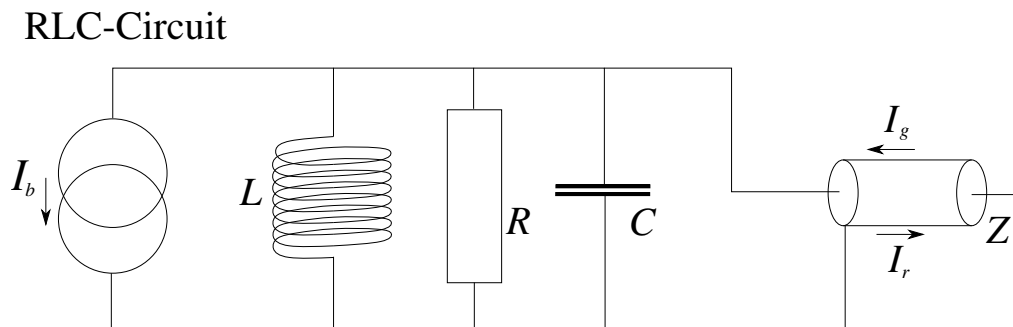
RLC-Circuit

Figure 4.1: Block diagram of the LHC SW cavity modelled as an RLC-circuit.

Consider the current flowing through the circuit given as

$$I_{RLC} = I_R + I_L + I_R. \tag{4.1}$$

By considering the relations between time-dependent currents and voltages through capaci-

tors, inductors and resistors, the equations can be rewritten to

$$\frac{1}{L}\int V(t)dt + C\frac{dV(t)}{dt} + V(t)\left(\frac{1}{R} + \frac{1}{Z}\right) = 2I_{\text{gen}}(t) - I_{\text{beam,RF}}(t) \tag{4.2}$$

as is detailed in [38]. Following the derivation in this paper, it can be shown that the parameters in the RLC circuit correspond to the physical properties of the cavity it serves to model. The resonant frequency ω_0 of the cavity is found to be

$$LC = \frac{1}{\omega_0^2}. \tag{4.3}$$

The capacitance in the RLC circuit is found to be

$$C = \frac{1}{\omega(R/Q)} \tag{4.4}$$

where ω is the RF frequency and (R/Q) is a property of the RF cavity defined as [39]

$$\frac{R}{Q} = \frac{|V_{\text{acc}}|^2}{2\omega_0 W}, \tag{4.5}$$

where V_{acc} is the accelerating voltage in the RF cavity and W is the energy stored in the cavity. Hence, (R/Q) is a measure of how much accelerating field the beams sees depending on how much energy is stored in the cavity. The resistance in the circuit is found to correspond to

$$R = Q_0(R/Q) \tag{4.6}$$

with Q_0 being the unloaded quality factor. Lastly, the transmission line in Fig. 4.1 with impedance Z modelling the coupler in the cavity is found to correspond to

$$Z = Q_{\text{ext}}(R/Q) \tag{4.7}$$

where Q_{ext} is known as the external quality factor. Using these relations and Eq. (4.2), it is shown in [38] that the generator current is given by

$$I_{\text{gen}}(t) = \frac{V_{\text{ant}}(t)}{2(R/Q)}\left(\frac{1}{Q_L} - 2i\frac{\Delta\omega}{\omega}\right) + \frac{dV_{\text{ant}}(t)}{dt}\frac{1}{\omega(R/Q)} + \frac{1}{2}I_{\text{beam,RF}}(t), \tag{4.8}$$

where $\Delta\omega = \omega_0 - \omega$ is the detuning of the RF cavity and Q_L is the loaded quality factor. The first term in Eq. (4.8) is generally $\frac{1}{Q_{\text{ext}}} + \frac{1}{Q_0}$, but for the superconducting cavities in the LHC it is assumed that $Q_{\text{ext}} << Q_0$ and $Q_L \approx Q_{\text{ext}}$, so the first term reduces to $1/Q_L$. The discretized version of Eq. (4.8) reads as

$$V_{\text{ant}}^{(n)} = (R/Q)\omega T_s I_{\text{gen}}^{(n-1)} + \left(1 - \frac{\omega T_s}{2Q_L} + i\Delta\omega T_s\right) - \frac{1}{2}(R/Q)\omega T_s I_{\text{beam,RF}}^{(n-1)} \tag{4.9}$$

with the upper indices denoting the time sample number. One of the signals that will be

studied in this chapter is the LHC RF cavity generator power, which is derived to be

$$P_{\text{gen}}(t) = \frac{1}{2}(R/Q)Q_L \left| I_{\text{gen}}(t) \right|^2 \tag{4.10}$$

in [38] and is always valid.

4.2 LHC RF-Feedback and One-turn Delay Feedback Model

To regulate the antenna voltage in the LHC cavities towards the set point, the LHC employs an RF feedback (RFFB) and a one-turn delay feedback (OTFB) [40]. Similar to the SPS cavity loop, the LHC cavity loop also serves to reduce the effective impedance of the LHC RF cavities seen by the beam.

The model of this system as it is implemented in BLonD is found in Fig. 4.2. In the same way as the SPS cavity controller implementation, all the currents and voltages are in IQ form, i.e. complex, and are discretely sampled on the coarse grid. In the LHC model however, the sampling time T_s is the length of 10 LHC RF buckets. This means that the sampling time is approximately 25 ns and 3564 samples per turn since this is the a tenth of the harmonic number of the LHC RF system. The typical values of all the parameters in the LHC RFFB and OTFB are found in Table 4.1.

Table 4.1: Typical values of the LHC cavity loop parameters.

Parameter	Symbol	Unit	Value
Overall loop delay	τ_{loop}	ns	650
Analog delay	τ_a	μs	170
Analog gain	G_a	A/V	6.79×10^{-6}
Digital delay	τ_d	μs	400
Digital gain	G_d	-	10
Analog-digital phase	$\Delta\varphi_{ad}$	-	0
OTFB gain	G_0	-	10
Comb filter coefficient	α	-	15/16
AC coupling time constant	τ_0	μs	110

4.2.1 Radio Frequency Feedback

The RFFB acts on the difference between the antenna voltage and the set point voltage. Due to the length of the wires between the LLRF system and the antenna measuring the cavity voltage, there is an overall loop delay τ_{loop} which must be taken into account. Hence, the feedback system acts on the following voltage

$$V_{\text{fb,in}}^{(n)} = V_{\text{set}}^{(n)} - V_{\text{ant}}^{(n-n_{\text{loop}})}, \tag{4.11}$$

Figure 4.2: Block diagram of the LHC cavity loop model as it is implemented in BLonD.

where all the voltages are taken to be complex, i.e. IQ-signals, and n denotes a given sample. Note also how the overall loop delay enters through n_{loop}, which is defined as $n_{\text{loop}} \equiv \text{int}\left(\tau_{\text{loop}}/T_s\right)$.

As shown in Fig. 4.2, the RFFB consists of two feedback subsystems. Namely, the analog feedback and the digital feedback. The analog feedback system is a high-pass filter with a gain G_a and the Laplace domain transfer function of the system is given as

$$H_a(s) = G_a \frac{\tau_a s}{1 + \tau_a s}, \tag{4.12}$$

where τ_a is the analog feedback delay. The optimum analog gain is given as

$$G_a = \frac{1}{2\frac{R}{Q}\omega\tau_{\text{loop}}} \tag{4.13}$$

for a flat closed-loop response. It is also worth noting that G_a has units $\frac{\text{A}}{\text{V}}$ and hence converts voltages into currents. In addition, it is possible to show that the output signal $y(t)$ of this system for a given input signal $x(t)$ in discrete time domain is given as

$$y^{(n)} = \left[1 - \frac{T_s}{\tau_a}\right] y^{(n-1)} + G_a \left(x^{(n)} - x^{(n-1)}\right), \tag{4.14}$$

where the superscript n denotes sample n.

The digital feedback is a low-pass filter, meaning it has a high gain at low frequencies. The

Laplace domain transfer function of this system is

$$H_d(s) = G_a G_d \frac{e^{i\Delta\varphi_{ad}}}{1 + \tau_d s}, \tag{4.15}$$

where G_d is the digital gain, τ_d is the digital delay and $\Delta\varphi_{ad}$ is the phase between the digital and analog feedbacks, which we would like to minimize. Similar to the analog feedback, the output $y(t)$ for a given input $x(t)$ signal for this system in discrete time domain is given as

$$y^{(n)} = \left[1 - \frac{T_s}{\tau_d}\right] y^{(n-1)} + G_a G_d e^{i\Delta\varphi_{ad}} \frac{T_s}{\tau_d} x^{(n-1)}. \tag{4.16}$$

4.2.2   LHC One-turn Delay Feedback

To boost the gain of the analog feedback in the LHC and to counteract coupled-bunch instabilities, one can also enable a one-turn delay feedback, which is essentially a comb filter. This system has a delay τ_{OTFB} which is complementary to the total loop delay such that the overall system acts exactly with a one turn delay.

The Laplace domain transfer function of the LHC OTFB is given as

$$H_{\mathrm{OTFB}}(s) = G_0 \frac{(1 - \alpha) e^{-T_{\mathrm{rev}} s}}{1 - \alpha e^{-T_{\mathrm{rev}} s}}, \tag{4.17}$$

where G_0 is the OTFB gain, α is the comb filter coefficient and T_{rev} is the revolution period of the turn at hand. The discrete time domain implementation of the OTFB can be shown to be

$$y^{(n)} = \alpha y^{(n-N)} + G_0(1 - \alpha) x^{(n-N)}, \tag{4.18}$$

where y is the output signal, x is the input signal and N is the total number of samples during an entire turn, hence $N \equiv \mathrm{int}\,(T_{\mathrm{rev}}/T_s)$.

To filter out undesired frequencies, the OTFB has an AC coupling both before the input and after the output. The AC coupling employed in conjunction with the LHC OTFB has the Laplace domain transfer function on the form

$$H_{\mathrm{AC,OTFB}}(s) = \frac{\tau_0 s}{1 + \tau_0 s}, \tag{4.19}$$

where τ_0 is time constant of the system. Additionally, in discrete time domain this corresponds to

$$y^{(n)} = \left[1 - \frac{T_s}{\tau_0}\right] y^{(n-1)} + x^{(n)} - x^{(n-1)}, \tag{4.20}$$

with the signals y and x being the output and input signals, respectively. Lastly, the LHC cavity loop also contains a 63-tap finite-impulse response (FIR) filter which is applied between the OTFB and the output AC coupling. The function of the FIR filter is to limit the bandwidth of the overall response of the OTFB.

4.3   Transfer Function Testing

By injecting white noise into the RFFB and OTFB circuits for various configurations, one can measure different aspect of the controller. This will now be used on the LHC RFFB model to compare with measurements on the real system.

4.3.1   Open Loop Transfer Function

The open loop response measurement is used in operation to get make a coarse adjustment of the system gain and phase before closing the loop. Additionally, this measurement is used to calibrate the loaded quality factor, Q_L. Figure 4.3 shows the simulated open loop response for a few different values of Q_L in the operational range. As is illustrated from the plot, Q_L influences the width and height of the open loop response transfer function. Both the width and the height increase with increasing Q_L.
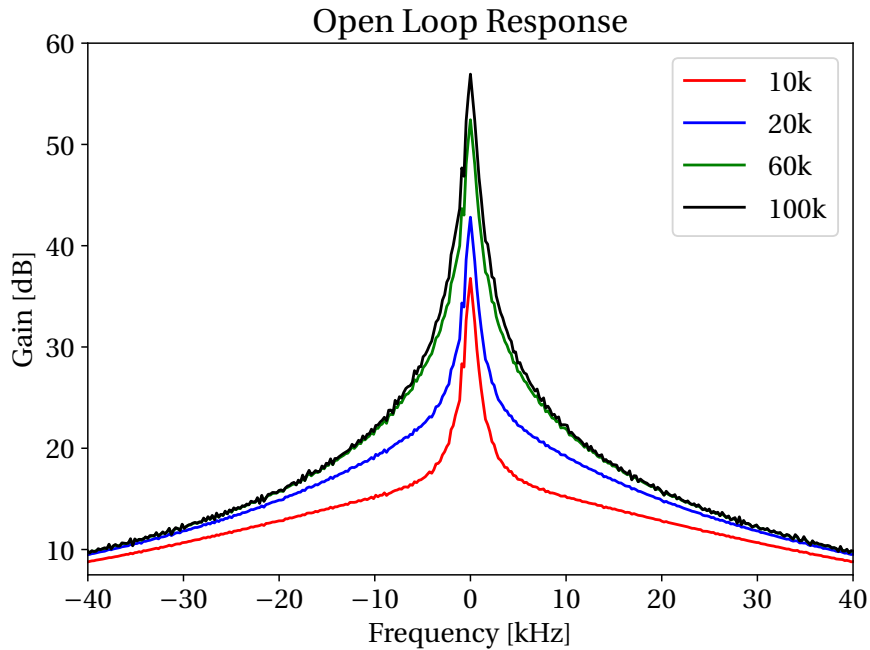
Figure 4.3: Simulated open loop response for four different values of Q_L. All the other parameters of the RFFB were the same as in Table 4.1.

An example of measurement of the open loop transfer function is found in Fig. 4.4. The figure shows the open loop response of cavity 1 for beam 1 and the simulated model in BLonD. The attenuated peak that can be seen in this plot is due to the digital feedback, which has gain at very low frequency. It should be said, however, that the zero-frequency value cannot be trusted in the BBNA measurements. We see that the simulated model is in good agreement with the measurement.
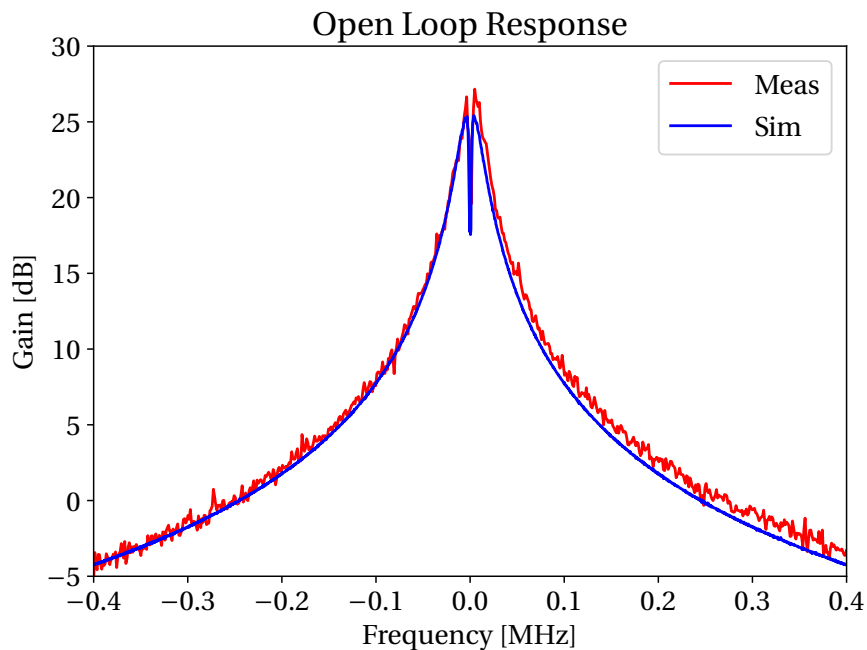
Figure 4.4: Open loop response from measurement of cavity 1 for beam 1 and the simulated BLonD model.

4.3.2 Closed Loop Transfer Function

The system's transfer function is also measured when the loop is closed. This is done to fine adjust the loop gain and phase. The gain is adjusted in order to obtain a flat response around the central ± 300 kHz bandwidth, which is desired to give better regulation. Figure 4.5 shows how the closed loop response varies with gain.

Figure 4.6 shows the closed loop measurement of cavity 1 for beam 1 in red and the simulated response from the BLonD model in blue. Both the simulated and the measured transfer function have a relatively flat response around the base-band, which indeed means that the cavity is well adjusted. In addition, we can see that there is a -20 dB attenuation of the higher frequencies, which is also something that is desired when adjusting the feedback. The gain, phase and overall behavior of the circuit seem to behave as expected. There is however, a small discrepancy in the width of the response.

Figure 4.5: Simulated closed loop responses where the gain and phase of the system has been varied slightly. All the other parameters in the loop are the same as Table 4.1.

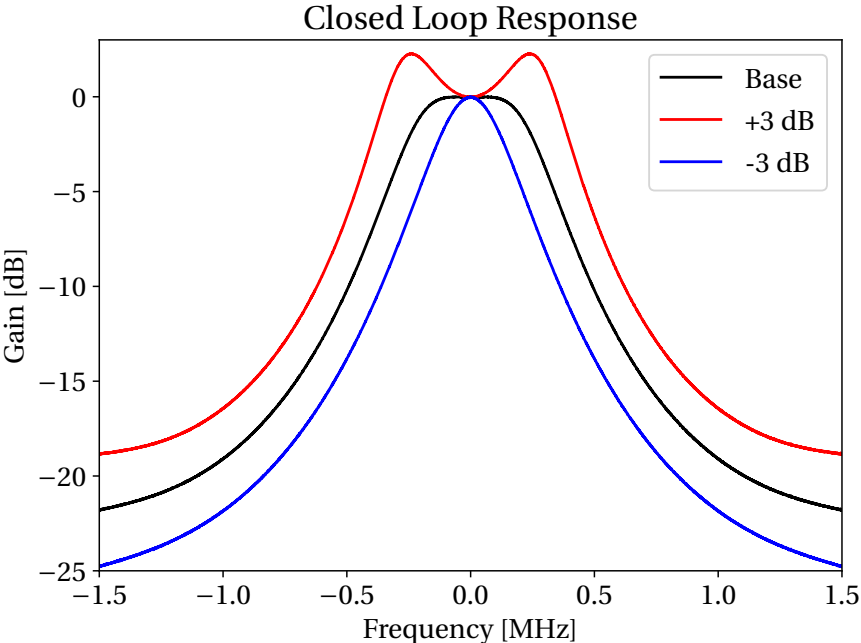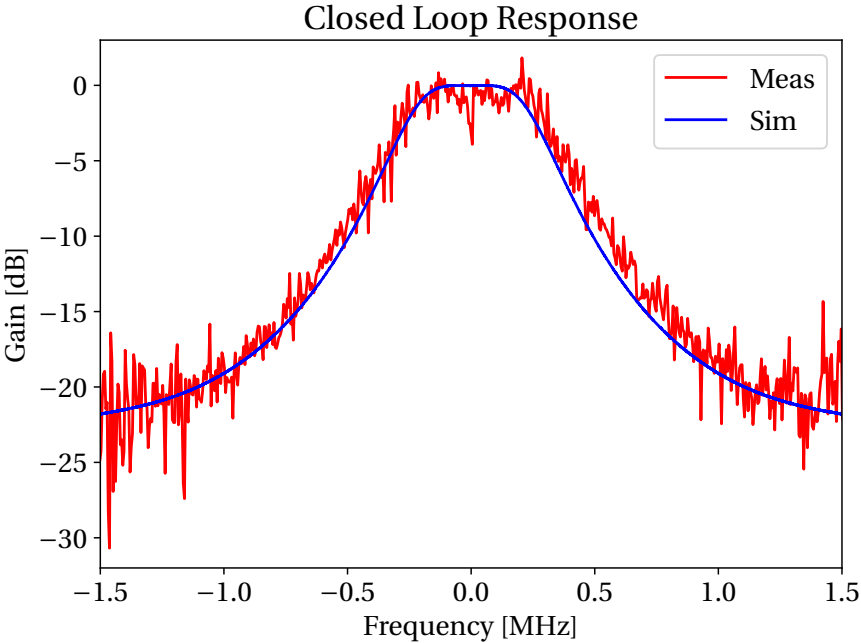**Figure 4.6:** Closed loop response from measurement of cavity 1 for beam 1 and the simulated response from the BLonD model.

4.4   LHC RF Power Consumption

Using Eq. (4.8), one can make analytic estimates of generator power consumption for a given antenna voltage. Assume that the cavity is not detuned, $\Delta\omega = 0$, that there is no beam, $I_{\text{beam, RF}}(t) = 0$, and that the antenna voltage is constant with time, $\frac{dV_{\text{ant}}(t)}{dt} = 0$. Eq. (4.8) is then simplified to

$$I_{\text{gen}} = \frac{V_{\text{ant}}}{2(R/Q)}\frac{1}{Q_L} \tag{4.21}$$

and thus the generator power is given as

$$P_{\text{gen}} = \frac{1}{8}\frac{1}{(R/Q)Q_L}|V_{\text{ant}}|^2 \; . \tag{4.22}$$

Unless otherwise specified, the parameters that are used for the calculations in this section are found in Table 4.1. Note also that the antenna voltage in Eq. (4.22) is the voltage in a single cavity. The simulated estimates were done by tracking the LHC cavity loop object without any beam. The loop was tracked for 100 turns to ensure that the signals had reached steady-state.

Table 4.2: Analytically estimated generator power compared with estimates from the BLonD LHC cavity loop model without OTFB. The generator power values and the antenna voltage given is the value for one RF cavity.

Total RF Voltage	Antenna Voltage	Analytic	Simulated	Measured
4 MV	0.50 MV	11.57 kW	11.51 kW	(11.4 ± 2.3) kW
5 MV	0.62 MV	18.08 kW	17.99 kW	(17.7 ± 3.5) kW
6 MV	0.75 MV	26.04 kW	25.90 kW	(25.3 ± 5.1) kW
7 MV	0.88 MV	35.45 kW	35.25 kW	(34.3 ± 6.9) kW
8 MV	1.00 MV	46.30 kW	46.04 kW	(45.6 ± 9.1) kW
9 MV	1.13 MV	58.59 kW	58.28 kW	(56.8 ± 11.4) kW
10 MV	1.25 MV	72.34 kW	71.95 kW	(70.5 ± 14.1) kW
11 MV	1.38 MV	87.53 kW	87.05 kW	(85.7 ± 17.1) kW
12 MV	1.50 MV	104.17 kW	103.60 kW	(101.8 ± 20.4) kW

Values of power are given Table 4.2. The value for the loaded quality factor was 60 000 for these estimates. The simulated power estimate was found to be consistently lower than the analytic by 0.54 % for all the antenna voltage values that were used. This was the case regardless of how long the LHC cavity loop was pre-tracked as long as the signals had reach steady-state. The error was found to arise from the fact that the RFFB does not regulate the antenna voltage perfectly to the set point in the simulated model, which is what is assumed in the analytic estimate. However, if the antenna voltage from the LHC cavity loop in simulations was used in Eq. (4.22) then the analytic estimate was found to match the simulated exactly.

Systematic measurements of the forward power of all the 16 klystrons was also done. The measured values can also be found in Table 4.2. Also in the LHC, the measurement of the

klystron forward power is estimated to have an uncertainty of 20 %. This uncertainty also shows in the line-by-line spread of measurement, see Fig. 4.7. The plot shows the klystron forward power as a function of time when measurements were performed. The total voltage in the cavities has been increased in parallel in a stepwise manner from 7 MV to 12 MV, in steps of 1 MV. Both the analytic and the simulated measurements seem to be well within the 20 % error bar of the measurements for all values of the RF voltage that were covered.
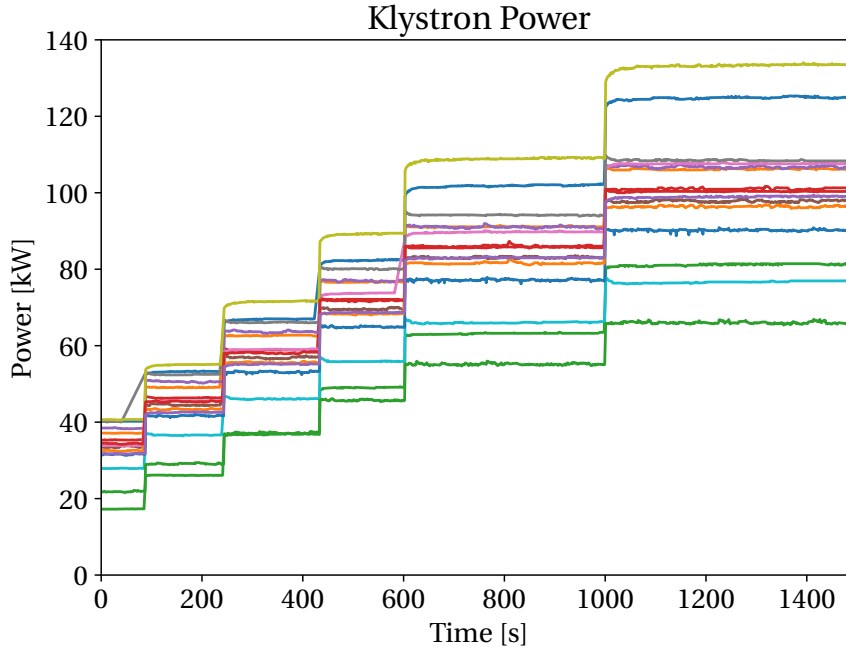
Figure 4.7: Measured forward klystron power from a ramp of the RF voltage from 7 MV to 12 MV in stemps of 1 MV.

4.5   LHC Power and Voltage with Beam

A beam of 120 bunches divided into 3 batches was simulated as a first test of the LHC RFFB with beam, i.e. without the OTFB. The three batches had a 12, 36 and 72 bunches and were spaced by 7.5 μs (3000 RF buckets). The bunches were spaced by 25 ns within each batch, had an intensity of 1.15×10^{11} p/b, a bigaussian profile and a bunch length of 1.2 ns. The rest of the simulation parameters can be found in Table 4.3. The parameters that were used for the RFFB are given in Table 4.1 Furthermore, the loaded quality factor was set to 20 000.

    The simulations were tracked until steady state was reached. The antenna voltage amplitude and phase and generator power can be found in Fig. 4.9. For the simulation corresponding to the yellow trace in Fig. 4.9, the LHC cavity loop model was tracked using the optimized half-detuning scheme, which was using the optimum detuning of -6.675 kHz for the given simulation parameters. The other simulations were tracked with a detuning that was a certain fraction of the half-detuning value. Figure 4.8 shows a measurement from [41] with the OTFB open. The no beam segment of the power in this measurement seems to be around 110 kW.

Table 4.3: Parameters used for the simulation with beam of the LHC cavity loop without the OTFB.

Parameter	Symbol	Unit	Value
Circumference	C	m	26658.883
Synchronous momentum	p_s	GeV / c^2	450
Transition gamma	γ_t	-	53.8
RF voltage	V	MV	6
Harmonic number	h	-	35640
RF phase	ϕ_{rf}	-	0

As mentioned in Sec. 4.4, the error bar on forward power measurements should be taken to be 20 %. With this taken into consideration, the no beam segment of the power signal from the three simulations with the largest detuning seems to match the measured within the uncertainty. On the other hand, it seems like simulation with optimal half-detuning cannot reproduce the power overshoot that is found in this measurement.

As seen in Fig. 4.9, the simulations that used lower detuning had a bigger overshoot in power. The simulations with detuning values of 1.67 kHz and 3.34 kHz managed to come close to the overshoot in measurement, at least qualitatively. In these cases, although the overshoot is closer to the measurement, we see that the no beam segment is lowered. This can be explained through setting $\frac{dV_{ant}}{dt} = 0$ and $I_{beam,RF} = 0$ in Eq. (4.8) and plugging it into Eq. (4.10), which yields

$$P_{gen} = \frac{1}{8} \frac{Q_L}{(R/Q)} \left(\frac{1}{Q_L^2} + \left(\frac{\Delta\omega}{\omega} \right)^2 \right) |V_{ant}|^2 . \tag{4.23}$$

As seen from Eq. (4.23), the power in the no beam segment increases with the square of the detuning of the cavity. Note that this is assuming that the antenna voltage is independent of time. From inspecting Fig. 4.9, there seems to be a slight gradient in the antenna voltage with time. Taking into account the substantial error bar in the forward power measurements however, the reduction is not enough to push the simulation with $\Delta f = 3.34$ kHz result outside the error margin.

The exact detuning value that was used in [41] is not known. It is likely that the detuning of the cavity in this paper was adjusted in a different way than using the optimal half-detuning value. For example in operation, the detuning of the RF cavities is done experimentally. The difference in the transient might therefore be caused by a difference in detuning. Additionally, the exact beam distribution that produced this measurement is not known either and can also influence the transient in power. The simulations seem to agree qualitatively with the measurement and it is possible to recreate a signal similar to the measured transient. Considering that these two parameters are not known and the uncertainty in the power measurement, there is a relatively good agreement between simulations and measurements.

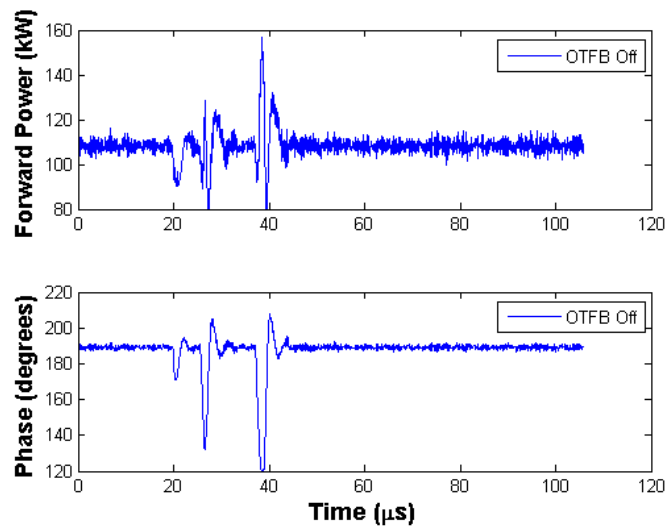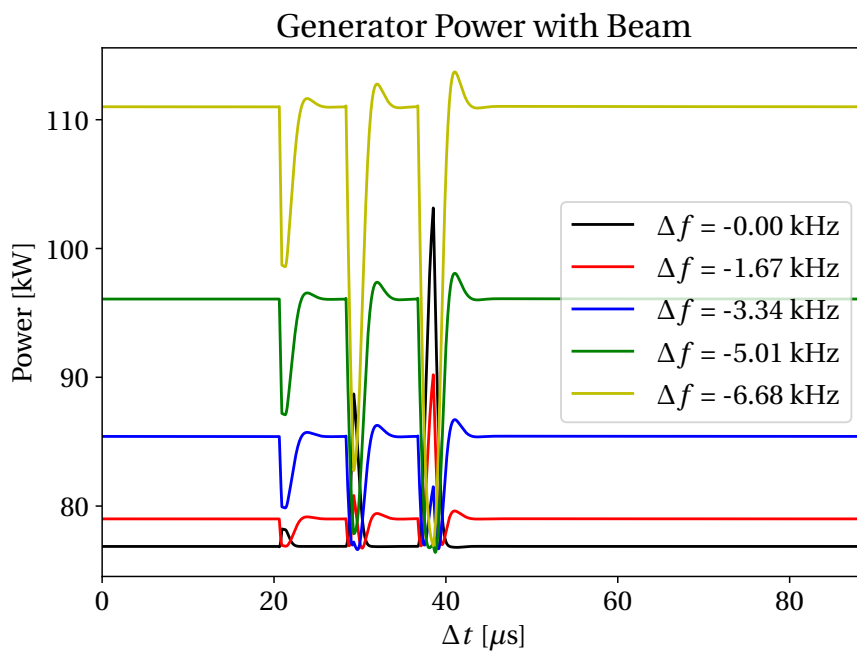**Figure 4.8:** Measured Klystron Forward Power with 12+36+72 bunches passing.

Figure 4.9: RF power for $12+36+72$ bunches in the LHC with the OTFB open. The trace with a detuning of -6.68 kHz corresponds to optimimum half-detuning value.

5 Future Work

For the purpose of LHC injection studies it seems that the SPS OTFB is benchmarked well. As mentioned in chapter 3, the purpose of model for the SPS-LHC injection studies is to generate a realistic bunch-by-bunch offset, which indeed it seems to do. However, the instabilities that were discussed in section 3.7 should be investigated further to ensure that this is something physical and not a numerical error in the BLonD SPS OTFB. To do this we suggest a new round of measurements of the SPS cycle where both OTFB signals and bunch profiles are measured. Additionally, the measurements should also be performed such that the stability of the measured cycle is verified. The measurements that this thesis compared simulations with was taken right after commissioning of after the LIU upgrade and measurements taken after some time with the new system in operation would be valuable.

To further improve the SPS OTFB model, it would help to implement more realistic filters. In particular the cavity filter, which in reality is not a moving average. Another improvement that can be made is the implantation of the additional comb filters that have notches at the synchrotron frequency. The first implementation of the SPS FF has already been made, but the real system is no yet commissioned. A benchmark of this part of the SPS cavity controller would be to compare with measurements of a SPS cycle when the SPS FF is used in operation.

For the LHC the next step would be to refine and benchmark the LHC OTFB. the LHC cavity loop should be benchmarked against measurement of operation in a similar to the SPS OTFB benchmark to ensure that the model gives good agreement with beam as well. The final step towards studying SPS-LHC transfer would be to couple the cavity controllers with the beam phase loop and the synchronization loop.

6 Conclusion

The benchmark of the SPS OTFB model that was documented in Chap. 3 was successful with respect to the future SPS-LHC injection studies. It was verified that the corrections from the OTFB are properly applied in particle tracking. This was done by showing that the beam-induced unit of the OTFB is compatible with the impedance models in BLonD. Additionally, it was verified that the behavior of the SPS OTFB is invariant under rotation in the I/Q-plane. The results in Sec. 3.6 show that the model is able to reproduce measurement of the real beam. In particular, it was found that as long as the simulation was stable, the bunch-by-bunch phase offset across the batch would lie within the uncertainty of the measurement for all the representative cases that was simulated, see Fig. 3.18. This is a very central result of the benchmark. Figure 3.18 illustrates that from the beam point-of-view, the model works to an acceptable degree. Indeed, this is the aspect of the model that is of most use for the injection studies. There are improvements to be made to the model however. One improvement to the SPS OTFB could be a more realistic cavity filter. Improvements such as this can help diminish the slight discrepancies in the bunch-by-bunch offset for the first few and last few bunches of the batch.

In simulations, coupled-bunch instabilities was encountered when recreating flattop SPS. A lot of investigation was done to see whether this was a physical instability or a numerical one. The various simulations that were done for Sec. 3.7 showed that the instability scales with voltage, resonant frequency and bunch length and is therefore compatible with a real instability. It should however be emphasized that it can not be excluded that the instability is numerically driven by the SPS OTFB. As mentioned in Chap. 5, the model should be compared with new measurements of SPS flat top to fully exclude the possibility of numerical excitation. The work that was done in Sec. 3.7 also proves how non-trivial it is both to recreate measurements with simulations and to do these simulations.

The SPS FF should also be refined and benchmarked against measurements to properly finalize the SPS cavity controller. The FF has an implementation which matches basic tests. However, to really refine it, one would have to track it with a beam to study its effect on the bunch-by-bunch offset.

The RFFB part of the LHC cavity loop is in excellent agreement with both measurement

of the open and closed loop transfer functions and measured power with and without beam. The open loop response that was compared with the measurement of cavity 1 for beam 1 seem to be in good agreement. The closed loop response is also in good agreement with the transfer function measurement it was compared to. In addition, the simulations of the LHC RFFB without beam was found to be in good agreement with analytic estimates. The discrepancy was found to be caused by the imperfect regulation of the antenna voltage towards the set point voltage. When compared to measurements of the klystron forward power, the simulated power matched the measurements within the error bar. Lastly, the LHC cavity loop without the OTFB was found to qualitatively reproduce measurements, not only in terms of no beam segment, but also the overshoot that was found in the measurement. The next step to finalize the LHC cavity loop is to refine the LHC OTFB and comparing its performance to measurements.

The final step before using these cavity loops for SPS-LHC injection studies is to couple the LHC cavity loop to the beam phase loop and the synchronization loop used in the LHC to regulate the RF frequency and the RF bucket center.

A I/Q-signals

Both the LHC and SPS cavity controllers use I/Q-signals. The following chapter will show how to go from a signal to its I/Q equivalent.

A.1   From signal to I/Q

Consider a sine-wave with a time-dependent amplitude, $A(t)$, and phase, $\phi(t)$;

$$f_c(t) = A(t)\sin\big(\omega_c t + \phi(t)\big) \tag{A.1}$$

where ω_c is the carrier frequency of the I/Q-signals. This expression can be rewritten as

$$f_c(t) = A(t)\sin\phi(t)\cos\omega_c t + A(t)\cos\phi(t)\sin\omega_c t. \tag{A.2}$$

To be consistent with the convetions in [34], we read of the corresponding I/Q-signal, $\tilde{f}_c(t)$, to $f_c(t)$ as

$$\tilde{f}_c(t) = A(t)\sin\phi(t) - i\,A(t)\cos\phi(t) = A(t)e^{i(\phi(t)-\pi/2)}. \tag{A.3}$$

Hence, it is possible to express the amplitude and phase of f_c in terms of the amplitude and phase of its corresponding I/Q-signal;

$$f_c(t) = \big|\tilde{f}_c(t)\big|\sin\big(\omega_c t + \angle\tilde{f}_c(t) + \pi/2\big). \tag{A.4}$$

Consider now a cosine-wave with a time-dependent amplitude, $A'(t)$, and phase, $\phi'(t)$;

$$g_c(t) = A'(t)\cos\big(\omega_c t + \phi'(t)\big) = A'(t)\sin\big(\omega_c t + \phi'(t) + \pi/2\big) \tag{A.5}$$

where ω_c again is the carrier frequency of the I/Q-signals. This can be rewritten as

$$g_c(t) = A'(t)\cos\phi'(t)\cos\omega_c - A'(t)\sin\phi'(t)\sin\omega_c t \tag{A.6}$$

and the I/Q-signal can be read of as

$$\tilde{g}_c(t) = A'(t)\cos\phi'(t) + A'(t)\sin\phi'(t) = A'(t)e^{i\phi'(t)}. \tag{A.7}$$

Notice how this could have been read of from Eq. (A.5) by expressing the cosine as a shifted

sine and the same I/Q-signal would have been obtained. In addition, the relation between the g_c and $\tilde{g}_c$ becomes

$$g_c(t) = \left|\tilde{g}_c(t)\right| \cos\left(\omega_c t + \angle\tilde{g}_c(t)\right). \tag{A.8}$$

A.1.1 Relation Between Sine- and Cosine-waves in I/Q

If $A(t) = A'(t)$ and $\phi(t) = \phi'(t)$ then we would expect $g_c(t)$ and $f_c(t)$ to be shifted by $\pi/2$ with respect to each other. This is reflected in their I/Q equivalents as well. The sine-wave is

$$\tilde{f}_c(t) = A(t)e^{i(\phi(t)-\pi/2)} \tag{A.9}$$

and the the cosine-wave becomes

$$\tilde{g}_c(t) = A(t)e^{i\phi(t)}. \tag{A.10}$$

It this then evident that

$$\tilde{g}_c(t) = e^{i\frac{\pi}{2}}\tilde{f}_c(t), \tag{A.11}$$

which is what one would expect from the know formula $\cos(x) = \sin(x + \pi/2)$.

Next, assume that $\tilde{f}_c(t) = \tilde{g}_c(t)$. Inserting into Eq. (A.8) yields

$$g_c(t) = \left|\tilde{f}_c(t)\right| \cos\left(\omega_c t + \angle\tilde{f}_c(t)\right) = \left|\tilde{f}_c(t)\right| \sin\left(\omega_c t + \angle\tilde{f}_c(t) + \pi/2\right) = f_c(t) \tag{A.12}$$

and so

$$f_c(t) = g_c(t) \Leftarrow \tilde{f}_c(t) = \tilde{g}_c(t). \tag{A.13}$$

If we assume $f_c(t) = g_c(t)$, then

$$f_c(t) = \left|\tilde{g}_c(t)\right| \cos\left(\omega_c t + \angle\tilde{g}_c(t)\right) = \left|\tilde{g}_c(t)\right| \sin\left(\omega_c t + \angle\tilde{g}_c(t) + \pi/2\right). \tag{A.14}$$

Using Eq. (A.4) and reading of yields $\left|\tilde{g}_c(t)\right| = \left|\tilde{f}_c(t)\right|$ and $\angle\tilde{g}_c(t) = \angle\tilde{f}_c(t)$, which means that $\tilde{g}_c(t) = \tilde{f}_c(t)$. This implies that

$$f_c(t) = g_c(t) \Leftrightarrow \tilde{f}_c(t) = \tilde{g}_c(t) \tag{A.15}$$

and that sine-to-I/Q and cosine-to-I/Q are consistent with each other.

A.1.2 Modulation of I/Q-signals

Consider the signal $f_c(t)$ and its I/Q equivalent

$$\tilde{f}_c(t) = A(t)e^{i(\phi(t)-\pi/2)}. \tag{A.16}$$

To modulate this signal from ω_c to some other angular frequency ω_r, first consider another signal $f_r(t)$

$$f_r(t) = A(t)\sin\left(\omega_r t + \phi'(t)\right) = A(t)\sin\left(\omega_c t + (\omega_r - \omega_c)t + \phi'(t)\right) \tag{A.17}$$

71

which gives an I/Q-signal

$$\tilde{f}_r(t) = A(t)e^{i\left((\omega_r - \omega_c)t + \phi'(t) - \pi/2\right)}. \tag{A.18}$$

If $\phi'(t) = \phi(t)$, then

$$\tilde{f}_r(t) = e^{-i(\omega_c - \omega_r)t}\tilde{f}_c(t), \tag{A.19}$$

which implies that $e^{i(\omega_r - \omega_c)t}$ is the transformation taking a signal from the initial angular frequency ω_c to the new angular frequency ω_r. If the I/Q signal is expressed as a 2D vector instead of a complex number with the in-phase part along the x-axis and quadrature part along the y-axis, then this transformation corresponds to the matrix

$$\begin{bmatrix} x_{I,r}(t) \\ x_{Q,r}(t) \end{bmatrix} = \begin{bmatrix} \cos{(\omega_c - \omega_r)}\,t & -\sin{(\omega_c - \omega_r)}\,t \\ \sin{(\omega_c - \omega_r)}\,t & \cos{(\omega_c - \omega_r)}\,t \end{bmatrix} \begin{bmatrix} x_{I,c}(t) \\ x_{Q,c}(t) \end{bmatrix}, \tag{A.20}$$

A.2 Generator-induced Voltage with Finite and Infinite Gain

Consider two IQ signals V_1 and V_2 that are both constant with time. V_1 have a real component $L\cos\theta$ and an imaginary component $L\sin\theta$. V_2 on the other hand, has an imaginary component equal to $L\sin\theta$ as well, but a real component which is slightly smaller than $L\cos\theta$ by ε. Hence the two signals are given as

$$V_1 = L\cos\theta + iL\sin\theta \tag{A.21a}$$

$$V_1 = L\cos\theta - \varepsilon + iL\sin\theta \tag{A.21b}$$

and are supposed to model the difference in generator-induced voltage in the SPS OTFB with infinite gain Eq. (A.21a) and finite gain Eq. (A.21b). The difference in absolute value of the two signals are given as

$$\Delta l = |V_1| - |V_2|. \tag{A.22}$$

Using the usual relation for the absolute value of complex numbers yields

$$\Delta l = L - \sqrt{(L\cos\theta)^2 - 2\varepsilon L\cos\theta + \varepsilon^2 + (L\sin\theta)^2} = L - \sqrt{L^2 - 2\varepsilon L\cos\theta + \varepsilon^2}. \tag{A.23}$$

Lastly, if we now consider $\varepsilon << L$ then

$$\Delta l \approx \frac{\varepsilon}{L}\cos\theta. \tag{A.24}$$

B Special Functions

This chapter contains special mathematical functions and transformations that are used elsewhere in the thesis.

B.1 Triangular- and Step-functions

The symmetrical triangular function is defined as

$$\text{tri}_S\left(\frac{t}{\tau}\right) = \left\{ \begin{array}{cl} 1 - |\frac{t}{\tau}| & : |t| < \tau \\ 0 & : \text{otherwise}, \end{array} \right. \tag{B.1}$$

where τ defines the length of the triangle. In the thesis we also use the right triangular function, which is defined as

$$\text{tri}_R\left(\frac{t}{\tau}\right) = \left\{ \begin{array}{cl} 1 - |\frac{t}{\tau}| & : 0 < t < \tau \\ 0 & : \text{otherwise}. \end{array} \right. \tag{B.2}$$

Note that the relation between the symmetric triangular function and the right triangular function is

$$\text{tri}_R\left(\frac{t}{\tau}\right) = \text{tri}_S\left(\frac{t}{\tau}\right) + \text{tri}_S\left(\frac{t}{\tau}\right)\text{sgn}\left(\frac{t}{\tau}\right) \tag{B.3}$$

and for the left triangular function the plus-sign on the right side of the equation is exchanged with a minus-sign. The function denoted as $\text{sgn}(x)$ is the sign-function and outputs the sign of the parameter.

The rectangular function is defined as

$$\text{rect}\left(\frac{t}{\tau}\right) = \left\{ \begin{array}{cl} 1 & : |t| < \frac{\tau}{2} \\ 0 & : \text{otherwise} \end{array} \right. \tag{B.4}$$

B.2 Fourier Transform

In this thesis we use the following normalization for the Fourier transformation

$$\hat{f}(\omega) = \mathscr{F}\{f(t)\} = \int_{-\infty}^{\infty} f(t)e^{i\omega t}dt \tag{B.5}$$

and therefore the inverse transform is normalized as

$$f(t) = \mathscr{F}^{-1}\{\hat{f}(\omega)\} = \frac{1}{2\pi}\int_{-\infty}^{\infty}\hat{f}(\omega)e^{-i\omega t}d\omega.$$

(B.6)

C SPS-LHC Injection Voltage Matching

To illustrate some of the problems what arise when injecting the beam from SPS into the LHC, the following appendix will go through the calculation of how to match the LHC RF bucket to the SPS RF bucket.

C.1 Longitudinal Emittance

Using Eq. (2.16) the longitudinal emittance for a single RF system, we get

$$\varepsilon = \frac{4E\omega_{s,0}\beta^2}{\omega_{rf}^2\eta_0} \int_0^{\varphi_b} d\varphi \sqrt{2\left(\cos\varphi - \cos\varphi_b\right)}. \tag{C.1}$$

The integral has to be estimated numerically in general and we define it as a variable $I \equiv \int_0^{\varphi_b} d\varphi \sqrt{2\left(\cos\varphi - \cos\varphi_b\right)}$.

C.2 Matching the RF Voltages

In order for the bunches not to blow-up in emittance upon transfer between the SPS and LHC, we impose the condition $\varepsilon_{\mathrm{SPS}} = \varepsilon_{\mathrm{LHC}}$. This conditions yields that

$$\left(\frac{\omega_{s,0}}{\omega_{rf}^2\eta_0}\right)_{\mathrm{SPS}} = \left(\frac{\omega_{s,0}}{\omega_{rf}^2\eta_0}\right)_{\mathrm{LHC}} \tag{C.2}$$

after canceling out all the parameters that are the same between the two accelerators upon injection. Next, using

$$\omega_{s,0} = 2\pi Q_s f_{\mathrm{rev}}, \tag{C.3a}$$

$$\omega_{rf} = 2\pi h f_{\mathrm{rev}}, \tag{C.3b}$$

$$Q_{s,0} = \sqrt{\frac{hV\eta_0}{2\pi\beta^2 E}} \tag{C.3c}$$

we get that

$$V_{\mathrm{LHC}} = V_{\mathrm{SPS}} \frac{\left(h^3 f_{\mathrm{rev}}^2 \eta_0\right)_{\mathrm{LHC}}}{\left(h^3 f_{\mathrm{rev}}^2 \eta_0\right)_{\mathrm{SPS}}} \frac{\left(I^2\right)_{\mathrm{SPS}}}{\left(I^2\right)_{\mathrm{LHC}}}. \tag{C.4}$$

Computing the integral I numerically, assuming the pre-LS2 maximum SPS voltage of 7 MV and a bunch length of 1.5 ns, we get that the LHC RF voltage should be approximately 1.9 MV.

D Additional SPS Simulation Results

This appendix contains additional plots of results from the SPS OTFB benchmark simulations. Fig. D.1 and Fig. D.2 are the results from the parameter scan of the OTFB gain around 20 linear. Fig. D.1 is with the TWC resonant frequency at the orignal design frequency and Fig. D.2 with the frequencies measured in 2018.
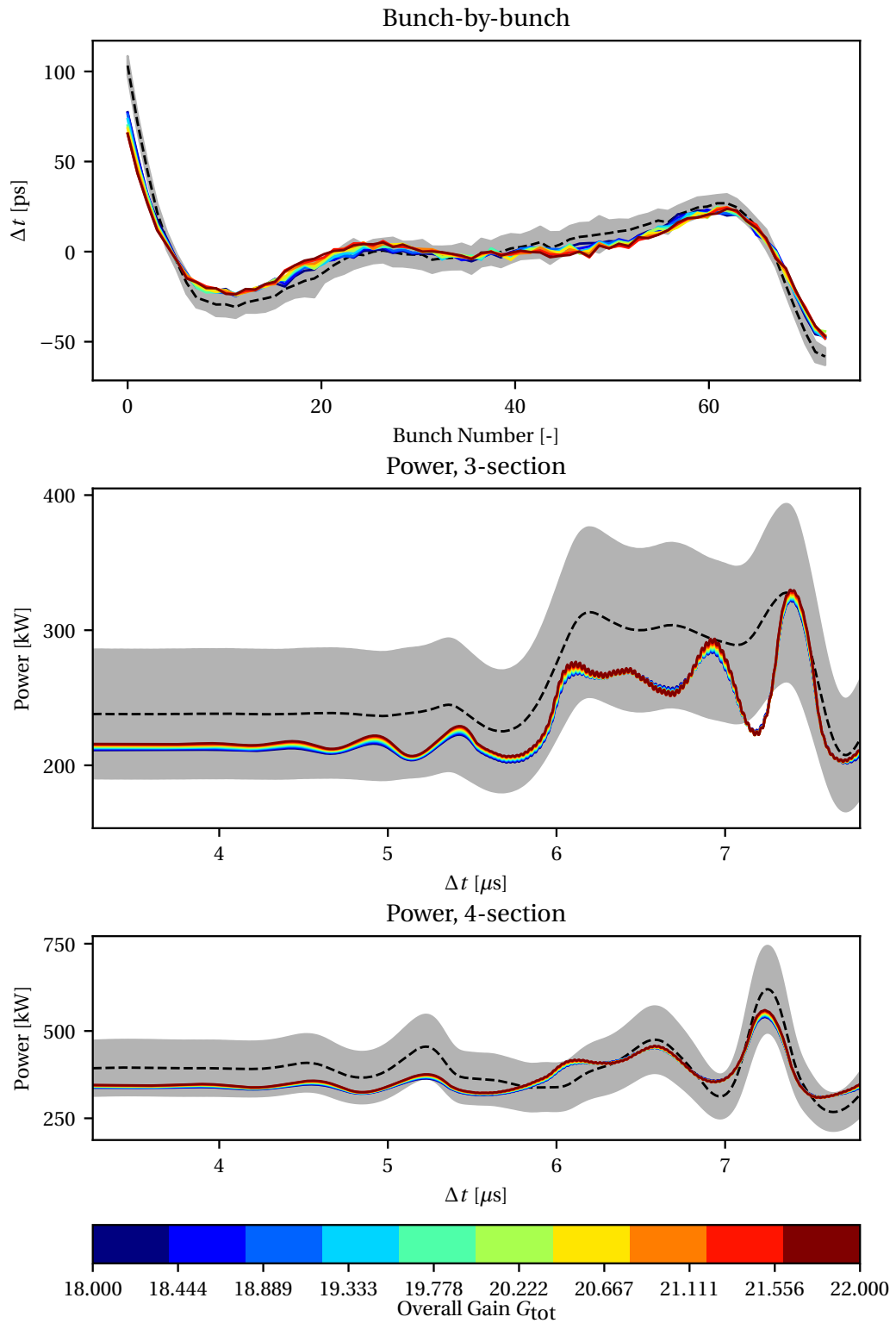
Figure D.1: Scan of the OTFB gain with all other simulation parameters equal to the baseline case except the transmitter gain G_{tx}. The resonant frequency of the TWCs were equal to the value that was initially designed (see Table 3.13).
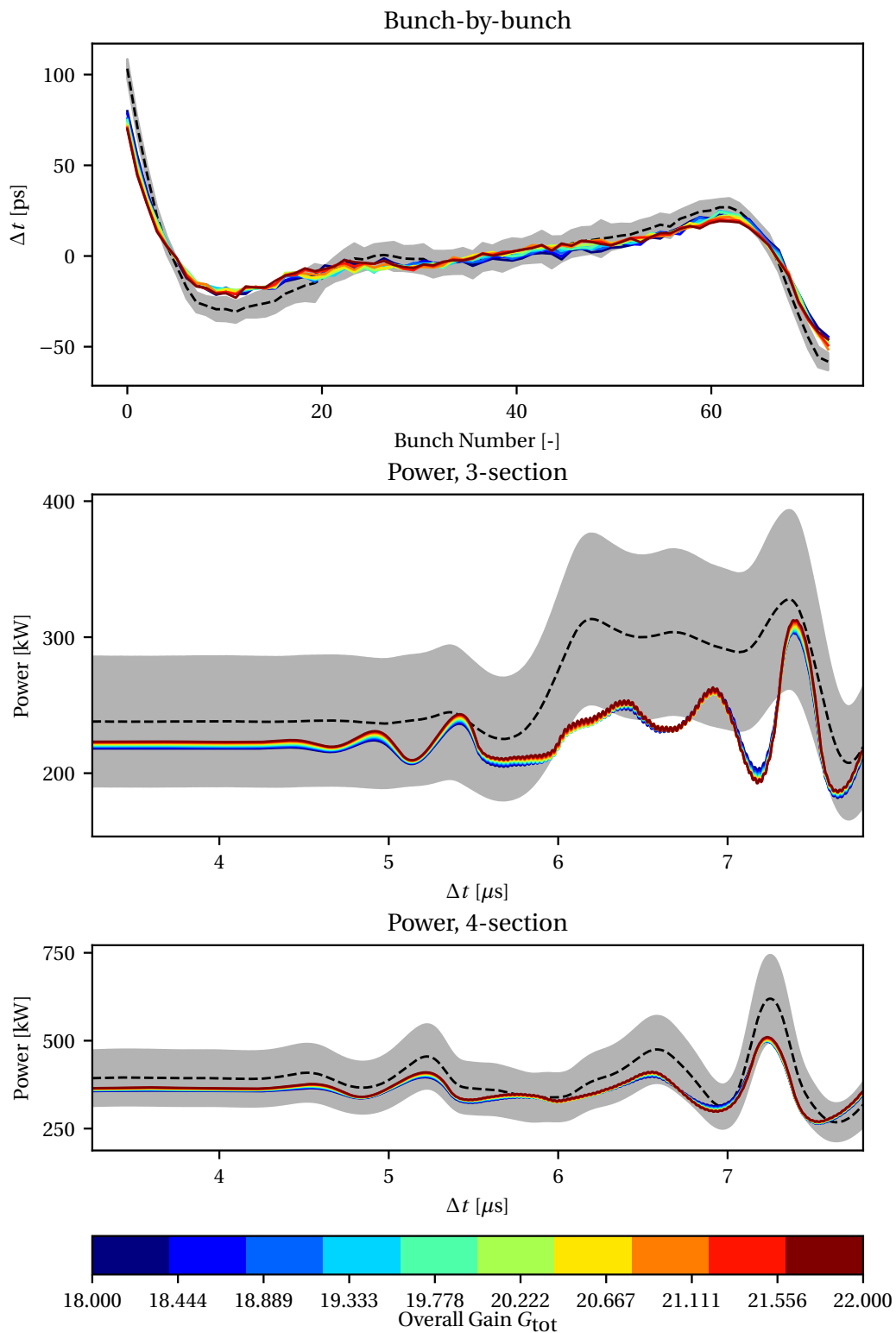
Figure D.2: Scan of the OTFB gain with all other simulation parameters equal to the baseline case except the transmitter gain G_{tx}. The resonant frequency of the TWCs were equal to the measured value in 2018 (see Table 3.13).

Bibliography

[1] Karlsen-Bæck BE. SPS One-Turn Delay Feedback Testing and Validation; 2022. Project Thesis (unpublished).

[2] Higgs PW. Broken Symmetries and the Masses of Gauge Bosons. Phys Rev Lett. 1964 Oct;13:508-9. Available from: https://link.aps.org/doi/10.1103/PhysRevLett.13.508.

[3] Englert F, Brout R. Broken Symmetry and the Mass of Gauge Vector Mesons. Phys Rev Lett. 1964 Aug;13:321-3. Available from: https://link.aps.org/doi/10.1103/PhysRevLett.13.321.

[4] Guralnik GS, Hagen CR, Kibble TWB. Global Conservation Laws and Massless Particles. Phys Rev Lett. 1964 Nov;13:585-7. Available from: https://link.aps.org/doi/10.1103/PhysRevLett.13.585.

[5] ATLAS Collaboration. Observation of a new particle in the search for the Standard Model Higgs boson with the ATLAS detector at the LHC. Physics Letters B. 2012;716(1):1-29. Available from: https://www.sciencedirect.com/science/article/pii/S037026931200857X.

[6] CMS Collaboration. Observation of a new boson at a mass of 125 GeV with the CMS experiment at the LHC. Physics Letters B. 2012;716(1):30-61. Available from: https://www.sciencedirect.com/science/article/pii/S0370269312008581.

[7] Mobs E. The CERN accelerator complex - 2019. Complexe des accélérateurs du CERN - 2019. 2019 Jul. General Photo. Available from: https://cds.cern.ch/record/2684277.

[8] Aberle O, Béjar Alonso I, Brüning O, Fessia P, Rossi L, Tavian L, et al. High-Luminosity Large Hadron Collider (HL-LHC): Technical design report. CERN Yellow Reports: Monographs. Geneva: CERN; 2020. Available from: https://cds.cern.ch/record/2749422.

[9] Damerau H, Funken A, Garoby R, Gilardoni S, Goddard B, Hanke K, et al. LHC Injectors Upgrade, Technical Design Report; 2014. Available from: http://cds.cern.ch/record/1976692.

[10] Timko, H. LHC RF: possible limitations and planned Run 3 studies; 2022. talk at the LHC Performance Workshop 2022 https://indi.to/P8t2d.

[11] Timko H, Albright S, Argyropoulos T, Iliakis K, Karpov I, Lasheen A, et al.. Beam Longitudinal Dynamics Simulation Suite BLonD;. (to be submitted).

[12] UA1 Collaboration. Experimental observation of isolated large transverse energy electrons with associated missing energy at s=540 GeV. Physics Letters B. 1983;122(1):103-16. Available from: https://www.sciencedirect.com/science/article/pii/0370269383911772.

[13] UA2 Collaboration. Observation of single isolated electrons of high transverse momentum in events with missing transverse energy at the CERN pp collider. Physics Letters B. 1983;122(5):476-85. Available from: https://www.sciencedirect.com/science/article/pii/0370269383916052.

[14] Dôme G. Travelling wave drift-tube structure for the CERN SPS; 1976. .

[15] Montesinos E. LIU-SPS 200 MHz RF Upgrade Presentation to SCK-CEN;. Available from: https://indico.cern.ch/event/822261/contributions/3437870/attachments/1847725/3032163/20190521_LIU-SPS_RF_power_upgrade_presentation_to_SCK-CEN.pptx.

[16] Shaposhnikova E. Longitudinal Instabilities in the SPS. 1999 Jan:6 p. Available from: https://cds.cern.ch/record/397579.

[17] Schwarz M, Iliakis K, Lasheen A, Papotti G, Repond J, Shaposhnikova E, et al. Flat-bottom instabilities in the CERN SPS. 2019:WEPTS049. 4 p. Available from: http://cds.cern.ch/record/2693533.

[18] Lasheen A, Argyropoulos T, Bohl T, Esteban Müller JF, Timko H, Shaposhnikova E. Beam measurement of the high frequency impedance sources with long bunches in the CERN Super Proton Synchrotron. Phys Rev Accel Beams. 2018 Mar;21:034401. Available from: https://link.aps.org/doi/10.1103/PhysRevAccelBeams.21.034401.

[19] Repond J. Possible Mitigations of Longitudinal Intensity Limitations for HL-LHC Beam in the CERN SPS; 2019. Presented 10 Oct 2019. Available from: http://cds.cern.ch/record/2695204.

[20] Boussard D, Chiaveri E, Häbel E, Kindermann HP, Losito R, Marque S, et al. The LHC superconducting cavities. 1999 Apr:3 p. Available from: http://cds.cern.ch/record/386691.

[21] Brunner OC, Frischholz H, Valuch D. RF Power Generation in LHC. 2003 Jun:4 p. Available from: https://cds.cern.ch/record/620365.

[22] Boussard D. rf power requirements for a high intensity proton collider ; parts 1 (chapters I, II, III) and 2 (chapters IV, V, VI). 1991 May:7 p. Available from: https://cds.cern.ch/record/221153.

[23] Brüning OS, Collier P, Lebrun P, Myers S, Ostojic R, Poole J, et al. LHC Design Report. CERN Yellow Reports: Monographs. Geneva: CERN; 2004. Available from: https://cds.cern.ch/record/782076.

[24] Lee SY. Accelerator Physics. 4th ed. World Scientific; 2019.

[25] Esteban Muller J. Longitudinal intensity effects in the CERN Large Hadron Collider; 2016. Presented 28 Jun 2016. Available from: https://cds.cern.ch/record/2196930.

[26] Kheifets SA, Zotter BW. Impedances and wakes in high-energy particle accelerators. Singapore: World Scientific; 1998.

[27] Palumbo L, Vaccaro VG. Wake fields, impedances and Green's function. (CERN Accelerator School). 1985 Sep.

[28] Cooley JW, Tukey JW. An Algorithm for the Machine Calculation of Complex Fourier Series. Mathematics of Computation. 1965;19(90):297-301. Available from: http://www.jstor.org/stable/2003354.

[29] Baudrenghien P, Mastoridis T. Proposal for an RF roadmap towards Ultimate Intensity in the LHC. Conf Proc. 2012 Apr;C1205201:MOPPC015. 7 p. Available from: https://cds.cern.ch/record/1460930.

[30] Mastoridis T, Baudrenghien P, Molendijk J. Cavity voltage phase modulation to reduce the high-luminosity Large Hadron Collider rf power requirements. Phys Rev Accel Beams. 2017 Oct;20:101003. Available from: https://link.aps.org/doi/10.1103/PhysRevAccelBeams.20.101003.

[31] Medina L, Timko H, Argyropoulos T, Shaposhnikova E, Salvachua B, Wenninger J, et al.. Optimal Injection Voltage in the LHC;. NIMA, accepted for publication.

[32] Weisstein EW. Laplace transform;. Available from: https://mathworld.wolfram.com/LaplaceTransform.html.

[33] Karpov I;. Private communication.

[34] Baudrenghien P, Mastoridis T. I/Q Model of the SPS 200 MHz Travelling Wave Cavity and Feedforward Design. 2020 May. Available from: http://cds.cern.ch/record/2719232.

[35] Hagmann G;. Private communication.

[36] Vollinger C;. Private communication.

[37] Quartullo D. Simulations of RF beam manipulations including intensity effects for CERN PSB and SPS upgrades;.

[38] Tückmantel J. Cavity-Beam-Transmitter Interaction Formula Collection with Derivation. 2010 Oct. Available from: http://cds.cern.ch/record/1323893.

[39] Bailey R, editor. CAS - CERN Accelerator School: RF for Accelerators: Ebeltoft, Denmark 8 - 17 Jun 2010. Proceedings of the CAS - CERN Accelerator School: Specialised Course on RF for Accelerators, Ebeltoft, Denmark, 8 - 17 Jun 2010. CAS - CERN Accelerator School: RF for Accelerators. CERN. Geneva: CERN; 2012. Comments: 20 lectures, 460 pages. Available from: http://cds.cern.ch/record/1231364.

[40] Baudrenghien P, Hagmann G, Molendijk JC, Olsen R, Rohlev A, Rossi V, et al. The LHC Low Level RF. 2006 Jul:4 p. Revised version submitted on 2006-08-28 14:51:11. Available from: http://cds.cern.ch/record/971742.

[41] Baudrenghien P, Mastoridis T, Molendijk J. The LHC One-Turn Feedback. 2012 Feb. Available from: https://cds.cern.ch/record/1424396.